

https://dspace.org/

Accuracy and associated measurement uncertainties in clinical dosimetry data for static small fields

Msimang, Zakithi Lungile Mpumelelo

2020

https://hdl.handle.net/10539/31402

Msimang, Zakithi Lungile Mpumelelo (2020) Accuracy and associated measurement uncertainties in clinical dosimetrydata for static small fields, University of the Witwatersrand, Johannesburg, <http://hdl.handle.net/10539/31402>

Downloaded from a DSpace repository. https://dspace.org/

UNIVERSITY OF THE WITWATERSRAND

JOHANNESBURG



FACULTY OF SCIENCE

ACCURACY AND ASSOCIATED MEASUREMENT UNCERTAINTIES IN CLINICAL DOSIMETRY DATA FOR STATIC SMALL FIELDS

Zakithi Lungile Mpumelelo Msimang

A thesis submitted to the Faculty of Science, University of the Witwatersrand, Johannesburg, in fulfilment of the requirements for the degree of Doctor of Philosophy

14 August 2020

DECLARATION

I declare that this thesis is my own, unaided work. It is being submitted for the Degree of Doctor of Philosophy at the University of the Witwatersrand, Johannesburg. It has not been submitted before for any degree or examination at any other University.

A waiver for ethics clearance was obtained from the Human Research Ethics Committee (Medical) at the University of Witwatersrand on 24/07/2017 Ref: W-CJ-170724-1. See appendix A for copy of the waiver.



_____

(Signature of candidate)

14 August 2020 at Johannesburg

ABSTRACT

Developments in radiotherapy techniques and technologies have contributed to an increase in the use of small fields. Small fields are used in stereotactic treatments and large uniform or non-uniform fields that are composed of small fields such as for intensity modulated radiation therapy (IMRT). Implementation has predated guidance documents for clinical dosimetry. The first international Code of Practice (CoP) for small field dosimetry was only published in 2017 by the International Atomic Energy Agency (IAEA), in collaboration with the American Association of Physicists in Medicine (AAPM).

There is a lack of data quantifying the accuracies linked with the use of small fields. Estimating and publishing uncertainties for measurement capabilities is standard practice for primary and secondary standard laboratories that operate within a rigorous total quality management system. This is not necessarily the case with clinical dosimetry measurements performed at hospitals, where there is a lack of published uncertainties for each of the steps used in the determination of the field output actors (FOF) for small fields.

In this study, the accuracy of detector positioning in small field clinical dosimetry measurements were evaluated in 6 MV and cobalt teletherapy beams with different collimation systems. In addition, the impact of two different methods of calculating the equivalent square, constancy and reproducibility of field output factors (FOFs) for different detectors, and machine stability over time, was evaluated. The influence of a reference detector was investigated. The uncertainties of all measurements were determined. For the linear accelerator data, the integrated multileaf collimator (MLC) and jaw were used as well as demountable stereotactic circular cones.

The data from the study highlighted the importance of verifying Central Axis (CAX) for independent measurement set ups and not relying on a visual set up using the field projection, the manufacturer's specifications of a detector or an automated water tank positioning system. A variation in CAX of 0.8 mm for in plane and 1.6 mm for cross plane was found to yield a 32 % variation in the FOF for S_{clin} of 0.6 cm. The solid-state

detectors used in the study performed better than the air ionisation detectors and are thus recommended as detectors of choice.

The study proved that the need for and frequency of the MLC calibration greatly affects the FOF, and lack of MLC maintenance will result in a gradual, unpredictable change in S_{clin}. A 3-monthly calibration period of the machine used in this study yielded results that were within the measurement uncertainties for the determination of S_{clin}, and it was concluded that this frequency was sufficient to achieve the required outcomes.

Data were compared to measurements provided by other hospitals in South Africa, standard data sets (BJR25) and other international hospitals that participated in the IAEA coordinated research project [E24021: “Testing of Code of Practice on Small Field Dosimetry”]. Comparison of measured data to that published in the British Journal of Radiology (BJR) Supplement No. 25 of 1996 showed that BJR 25 data for 6MV and cobalt teletherapy should not be adopted for $S_{clin} \leq$ than 6 cm. Local data should be determined experimentally.

For reference measurements, the standard uncertainty contributed by the traceability process of daisy-chaining, contributed the most significant uncertainty. For relative dosimetry measurements, the standard uncertainty associated with the determination of the FOF contributed the most significant uncertainty. These were identified as the two high risk areas in the dosimetry chain for small static field dosimetry. As such, dosimetry audits for small fields should focus on the FOF and reference dose determination in field sizes ≤ 2 cm.

DEDICATION

Dedicated to my family (both spiritual and biological), especially my late father Luke Mkhulu Msimang, my mother Eleanor Nunu Msimang, and my son Londa M.M. Msimang. Thank you all for your support and prayers.

ACKNOWLEDGEMENTS

I would like to acknowledge the following who had a major impact in my journey. A special thanks to Professor Debbie van der Merwe for the encouragement and guidance. Mr Nkosi Maphumulo and Mr Lazola Nobecu for spending their Saturdays assisting me with the operation of the equipment and for our valuable discussions on dosimetry. I also thank the Charlotte Maxeke Johannesburg Academic Hospital for the use of their equipment; PTW for the loan of several detectors; the University of the Witwatersrand and the National Metrology Institute of South Africa (NMISA) for supporting my studies. Most of all, I thank my Lord and saviour Jesus Christ for His love and undeniable guidance.

CONTENTS

List of figures x
List of tables xviii
1. Introduction 1
1.1 Overview 1
1.2 Hypothesis 3
1.3 Purpose of the study 3
1.4 Structure of the thesis 5
2. Dosimetry concepts in radiotherapy 6
2.1 Introduction 6
2.2 Dosimetry quantities and units 6
2.2.1 Photon fluence Φ and Energy Fluence Ψ 6
2.2.2 Attenuation coefficients 7
2.2.3 Kerma 9
2.2.4 Absorbed dose D 9
2.2.5 Stopping power 10
2.2.6 Charged particle equilibrium (CPE) 10
2.3 Relations between some of the dosimetric quantities 11
2.3.1 Energy fluence and kerma 11
2.3.2 Energy fluence and absorbed dose 12
2.4 Cavity theory 12
2.4.1 Cavity theory for large photon detectors 13
2.4.2 Bragg-Gray cavity theory 14
2.4.3 Spencer-Attix formalism 16
3. Traceability of measurements in dosimetry for absorbed dose 18
3.1 Introduction 18
3.2 Primary standards for absorbed dose to water 20
3.2.1 Water calorimeter 21
3.2.2 Graphite calorimeter 22
3.2.3 Primary cavity ionisation chambers 23
3.3 Secondary standards for absorbed dose to water 24
3.4 Dosimetry formalism 25
3.4.1 Calibration at a Secondary Standard Laboratory in a Co-60 beam 25
3.4.2 Reference beams 26
3.4.3 Cross calibration at the user's beam 27

3.4.4 Output factor measurements 28
3.4.5 Beam quality index 28
4. Physics of small field dosimetry 30
4.1 Introduction 30
4.2 Characteristics of small field 32
4.2.1 Lack of lateral charged particle equilibrium 32
4.2.2 Partial occlusion of the primary photon source 34
4.2.3 Detector effects 35
4.2.4 Energy spectrum of small fields 36
4.3 Traceability for small photon fields 37
4.3.1 Water calorimeter 37
4.3.2 Graphite calorimeter 38
4.3.3 Detectors used for small field dosimetry 38
4.4 Dosimetry formalism in small fields 39
4.4.1 Reference dosimetry 39
4.4.2 Field output factor 41
4.4.3 Field size 42
4.4.4 Beam quality Indices 42
5. Introduction to measurement uncertainty 44
5.1 Terminology 45
5.1.1 Measurement accuracy and measurement precision 45
5.1.2 Measurement repeatability 46
5.1.3 Measurement reproducibility 47
5.1.4 Measurement error 47
5.1.5 Measurement uncertainty 47
6. Experimental: Materials and Methods 51
6.1 Materials 51
6.1.1 Irradiators and data collecting system 51
6.1.2 Detectors and electrometers 54
6.2 Methodology 59
6.2.1 Alignment of the water phantom with the gantry and positioning of a detector 59
6.2.2 Determination of the equivalent square field size 63
6.2.3 Determination, constancy and reproducibility of field output factors 64
6.2.4 Measurements with and without a reference chamber 69
6.2.5 Beam quality Indices 70
6.2.6 Traceability of measurements with different small field detectors 70
6.3 Estimation of uncertainties 71

6.3.1 Reference measurements 71
6.3.2 Relative measurements 76
7. Results and discussions 79
7.1 Alignment of the water phantom with the gantry 79
7.2 Determination of the equivalent square field size 79
7.2.1 Equivalent square field determined using various detectors in MLC fields, measured over a period of 333 days 81
7.2.2 Equivalent square field determined using various detectors in MLC fields, measured in the same session 82
7.2.3 Equivalent square field determined using various detectors in cone fields 84
7.3 Determination, constancy and reproducibility of field output factors 87
7.3.1 The impact of no CAX correction on the accuracy of the treatment data 87
7.3.2 Determination of field output correction factors. 88
7.3.3 Determination of the field output correction factors for the PTW 31021 detector 89
7.3.4 Variation of the field output factors with detectors for a linac beam 91
7.3.5 Variation of the field output factors with detectors in a Co-60 beam 101
7.3.6 Variation of equivalent square field size, S_{clin}, with MLC movement and calibration and its effect on field output factor 103
7.3.7 Variation of equivalent square field size, S_{clin}, and the field output factor measurements with induced gantry and collimator errors 110
7.3.8 Variation of the determination of field size and field output factor with the orientation of a detector 113
7.4 Measurements with and without a reference detector 119
7.5 Beam quality Indices 122
7.6 Traceability of measurements 124
7.7 Estimation of uncertainties 125
8. Conclusions 129
9. Future work 133
References 134
Appendix A: Ethics waiver 146

List of figures

List of figures	Page No.
Figure 2.1 Depiction of the charged particle equilibrium. A charged particle y of a given type and energy, E, leaves the volume, v, and is replaced by a charged particle x of the same type and energy.	11
Figure 2.2 Depiction of a detector that is introduced into a medium on the left thus giving D_{det} for a given exposure to radiation of beam quality, Q, and then being converted into the dose D_{med} at point + in the absence of the detector (Mayles, 2007).	13
Figure 2.3 Depiction of a small detector in a medium irradiated with a photon beam. The detector is small compared to the secondary electron ranges (Nahum, 2009).	15
Figure 2.4 A graphical representation of the energy deposited in a cavity following the Spencer-Attix energy deposition model. The incident fluence of electrons, that contains all generations of electrons, Φ^{total}, is identical to that present in the uniform medium (Nahum, 2009).	17
Figure 4.1 The ratios of the dose-to-water, D_w, to water-collision kerma, $K_{col,w}$, versus the radius of the beam for beam energies Co-60, 4 MV, 6 MV, 10 MV, 15 MV and 24 MV. The ratios were evaluated on the central axis of the beam, at a depth of 5 cm, SSD of 80 cm for Co-60 and SSD of 100 cm for all the other beams (Reproduced from IAEA TRS 483 (IAEA, 2017) with permission from Papaconstadopoulos, McGill University, Canada).	34
Figure 4.2 Illustration of the partial source occlusion. On the “full view of extended direct beam source”, the source is viewable from the plane of measurement and penumbra is separate. To the right is the “partial view of extended direct beam source”, the source is not viewable from the measurement plane of view and the penumbra is overlapping (IPEM, 2010).	35

List of figures	Page No.
Figure 5.1 Representation of (a) low accuracy and low precision, (b) high accuracy and low precision, (c) low accuracy and high precision, and (d) high precision and high accuracy (Streiner, 2006).	46
Figure 5.2 A Gaussian distribution (continuous black curve) and a t-distribution with four degrees of freedom (broken red curve) ('unit' denotes any unit) (BIPM JCGM, 2009).	49
Figure 5.3 A triangular distribution with limits a and b (BIPM JCGM, 2009).	50
Figure 6.1 Treatment units from CMJAH that were used for the study (a) Siemens Primus linear accelerator and (b) Equinox 80 Co-60 unit.	52
Figure 6.2 The Siemens Primus linac head at CMJAH with a demountable tertiary collimator attached.	53
Figure 6.3 The motorised PTW MP3 water tank that was used for the measurements at CMJAH.	54
Figure 6.4 Picture showing small field detectors used in the study. From top to bottom they are PTW 60012, PTW 31016, PTW 31018, PTW 31021 and PTW 60019.	55
Figure 6.5 Positioning of a detector using the machine cross hair when the detector is oriented perpendicular to the beam. The tip of the detector was positioned such that it just touches the projection of the cross hair. Then the detector travel along the axes was checked using the projected machine cross hair as the detector travelled along each axis.	60

List of figures	Page No.
Figure 6.6 Pictures showing the sequential positioning of the reference point of a detector on the central axis of the beam when the detector is oriented parallel to the field. Picture on left showing the tip of the detector positioned few mm from the water surface, centre picture showing the detector on the water surface and the picture on the right showing the reference point of the detector on the central axis of the beam. The dimensions specified by the manufacturer were used for the setting up.	61
Figure 6.7 Pictures showing the sequential positioning of the reference point of a detector on the central axis of the beam when detector is oriented perpendicular to the field. Picture on left showing the central axis of the detector positioned few mm from the water surface, centre picture showing the central axis of the detector on the water surface and the picture on the right showing the reference point of the detector on the central axis of the beam. The dimensions specified by the manufacturer were used for the set up.	62
Figure 6.8 The setup of a PTW 34091 ionization chamber placed 30 cm from the surface of the water.	70
Figure 7.1 Standard deviation of the mean for measurements of S_{clin} that were performed using the detectors PTW 31018, PTW 60019, PTW 60012, PTW 31021 and PTW 31016 on the same day but measured on four different days, in a 6 MV beam for field sizes defined by an MLC and jaw.	84
Figure 7.2 Variance of field output factors versus S_{clin}, when various PTW detectors were used to measure field size with no FOCF.	89

List of figures	Page No.
Figure 7.3 FOCFs derived for the PTW 31021 detector and determined from the FOCFs for the PTW 60019 and PTW 60012 detectors as published in the IAEA TRS 483. The graph also shows factors for the PTW 31021 determined using the analytical function suggested by Sauer (Sauer, 2007) and given as Sauer-P and Sauer-T. Data are labelled #-P-60012 and #-T-60012 where # is the sequence in which the measurements were taken; P refers to detector orientation parallel to the beam and T refers to detector orientation perpendicular to the beam. The other numbers are the model numbers of the detectors.	90
Figure 7.4 The FOFs versus the equivalent square field, $S_{clin,}$ determined using detectors PTW 60019, PTW 31018, PTW 31010, PTW 31021 and PTW 60012. The measurements were performed over a period of 333 days on 14 different days at various MLC calibration intervals, and the average of all the measurements is displayed here.	92
Figure 7.5 The measured FOF versus the equivalent square field, S_{clin}, from this study (A), and at centres D (D) and E (E and E-M). Data from treatment planning systems of centres D and E are labelled D and E-M respectively. BJR-25 data are also plotted (BJR-25, 1996).	94
Figure 7.6 FOF versus equivalent square field measurements obtained from data using various detectors and demountable stereotactic cones at CMJAH in a 6 MV beam. The depth of the measurements was 5 cm in water with SAD of 100 cm.	95
Figure 7.7 A plot of the average data for FOF versus S_{clin} measurements obtained from data using various detectors when the field is defined with Brainlab demountable cones at centres A, B and C. The depth of measurements was 10 cm and 6 MV was used by all centres. All data were normalised to 10 x 10 cm^2 field size.	97

List of figures	Page No.
Figure 7.8 Data for FOF versus S_{clin} measurements obtained from data using only synthetic diamond detectors, PTW60019, when the field is defined with Brainlab demountable cones at centres A, B and C. The depth of measurements was 10 cm and 6 MV was used by all centres. All data were normalised to 10 x 10 cm^2 field size.	98
Figure 7.9 Data for FOF versus equivalent square field measurements obtained from data using diode detectors (PTW 60012, PTW 60017, PTW 60016 and IBA SFD) when the field is defined with Brainlab demountable cones at centres A, B and C. Depth of measurements was 10 cm and 6 MV energy was used by all centres. All data were normalised at 10 x 10 cm^2 field size.	99
Figure 7.10 Data for FOF versus S_{clin} obtained from data using ionisation chambers when the field is defined with Brainlab demountable cones at centres A and B. The depth of measurements was 10 cm and 6 MV was used by all centres. All data were normalised at 10 x 10 cm^2 field size.	100
Figure 7.11 FOF versus S_{clin} obtained from data using various PTW detectors when the field is defined with Brainlab demountable cones at centres A and C. The depth of measurements was 5 cm.	101
Figure 7.12 FOF versus S_{clin} measured using various PTW detectors in a Co-60 beam. No FOCFs were applied. BJR-25 data were also plotted (BJR-25, 1996).	102
Figure 7.13 FOFs versus equivalent square field measured using a PTW 60012 detector over a period of 333 days on 11 different days. MLC calibrations were performed at least every three months. The data were for a 6 MV beam.	103

List of figures	Page No.
Figure 7.14 FOF versus equivalent square field measured using various PTW detectors over a period of 117 days on 6 different days during which MLC calibrations were performed at least every three months. The equivalent square field data were obtained from the measurement with the PTW 60012 detector. Data were for a 6 MV beam.	104
Figure 7.15 The variation of the FOFs versus equivalent square field measured using a PTW 60012 detector over a period of 57 days over four different days. There was no MLC calibration during this period.	106
Figure 7.16 The standard deviation of the mean versus S_{clin} for the FOF and equivalent square field data that were measured over a period of 294 days during which there was one MLC calibration. The data were measured using a PTW 60019 detector.	107
Figure 7.17 The plot of the standard deviation of the mean versus S_{clin} for the FOF and equivalent square field data that were measured over a period of 333 days on 11 different days during which MLC calibrations were performed at least every three months. The data were measured using a PTW 60012 detector.	108
Figure 7.18 The plot of the standard deviation of the mean versus S_{clin} for the FOF and equivalent square field data that were measured over a period of 329 days on 3 different days during which MLC calibrations were performed at least every three months. The data were measured using a PTW 31021 detector.	109
Figure 7.19 The plot of the standard deviation of the mean versus S_{clin} for the FOF and equivalent square field data that were measured over a period of 399 days on 4 different days during which MLC calibrations were performed at least every three months. The data were measured using a PTW 31018 detector.	110

List of figures	Page No.
Figure 7.20 Averaged FOF data obtained when ionisation chambers were oriented parallel and perpendicular to the beam. Data for the PTW 31016 detector were collected over a period of 28 days on three different days, data for the PTW 31018 detector were collected over a period of 7 days on two different days and data for the PTW 31021 detector were collected over a period of 196 days on three different days. T represents data when the ionisation chamber was oriented perpendicular to the beam and II represents data when the ionisation chamber was oriented parallel to the beam.	114
Figure 7.21 FOF versus S_{clin} obtained using a PTW 31016 detector oriented parallel and perpendicular to the beam in a 6 MV beam. T represents data when the ionisation chamber was oriented perpendicular to the beam and II represents data when the ionisation chamber was oriented parallel to the beam. The data set were measured in a period of 28 days and there was an MLC calibration between data 2 and 3.	115
Figure 7.22 FOF versus S_{clin} obtained using a PTW 31018 detector oriented parallel and perpendicular to the beam in a 6 MV beam. T represents data when the ionisation chamber was oriented perpendicular to the beam and II represents data when the ionisation chamber was oriented parallel to the beam. The data set 1 and 2 were measured seven days apart.	116
Figure 7.23 FOF versus S_{clin} obtained using a PTW 31021 detector oriented perpendicular and parallel to the beam. The data shown were collected over a period of 196 days. T represents data when the ionisation chamber was oriented perpendicular to the beam and II represents data when the ionisation chamber was oriented parallel to the beam.	117

List of figures	Page No.
Figure 7.24 Standard deviation of the mean versus set field size for measurements using a PTW 31021 ionisation chamber when the orientation of the detector is the same when measuring field size and when measuring FOFs. The measurements were performed over a period of 196 days but those compared for perpendicular and parallel were performed on the same say. Measurements were performed in a 6 MV photon beam.	118
Figure 7.25 *PDD* curve for a set field size of 0.6 x 0.6 cm^2 measured with and without a reference detector, PTW 34091. Yellow represents the data that were obtained with a PTW 34091 detector in the beam and pink represents the data for measurements without a PTW 34091. Each curve normalised at depth of maximum dose.	120
Figure 7.26 *PDD* curve for a set field size of 1 x 1 cm^2 measured with and without a reference detector, PTW 34091. Red represents the data that were obtained with a PTW 34091 detector in the beam and green represents the data for measurements without a PTW 34091 detector. Each curve normalised at depth of maximum dose.	121
Figure 7.27 Percentage difference in the FOF values measured with and without a PTW 34091 detector when using a PTW 31021 and a PTW 31010 detector to measure FOFs.	122
Figure 7.28 $TPR_{20,10}(10)$ measured in a 6 MV beam using various PTW detectors over a period of two years with MLC calibration periodically. 31016 II refers to the detector positioned parallel to the beam and 31016 T, to the detector positioned parallel to the beam.	124

List of tables

List of tables	Page No.
Table 6.1 Specifications of the solid-state detectors used during the study provided by the manufacturer.	56
Table 6.2 Specifications of the ionisation chambers used during the study provided by the manufacturer.	57
Table 7.1 S_{clin} and ESQ determined using equations 6.1 and 6.2 in the 6 MV beam and the FOFs obtained with a PTW 60012. The uncertainties associated with the measurements of the field size was 0.06 cm.	80
Table 7.2 S_{clin} and ESQ determined using equations 6.1 and 6.2 in the 6 MV beam and the FOFs obtained with a PTW 31018. The uncertainties associated with the measurements of the field size was 0.06 cm.	81
Table 7.3 The variation of the equivalent square field size as measured with different detectors for field sizes defined by an MLC and jaw. The result is the average of more than three sets of measurements obtained over a period of 333 days in the same 6 MV beam.	82
Table 7.4 The equivalent square field size, S_{clin}, measured at depth 10 cm in a water phantom at a SAD of 100 cm using PTW 60019, PTW 60012, and PTW 31021 detectors for a set of stereotactic cones of different diameters. The data were measured on the same day.	84
Table 7.5 The variation in the equivalent square field size, S_{clin} measured at depth 10 cm in a water phantom at a SAD of 100 cm using a PTW 60019, PTW 60012, and PTW 31021 detectors for a set of stereotactic cones of different diameters. The data were measured on four different days over a period of 28 months.	86

List of tables	Page No.
Table 7.6 The variation of the equivalent square field size, S_{clin}, for demountable cones measured at a depth of 5 cm in water at a SAD of 100 cm using PTW 60012, PTW 60019 and PTW 31016 detectors.	87
Table 7.7 The variations in CAX and how they impact on the S_{clin} and the FOF data measured using a PTW 31018 detector.	88
Table 7.8 FOCF derived for the PTW 31021 from data presented in figure 7.3 together with the associated relative measurement uncertainty for a coverage factor of k = 2, equal to confidence level of 95 %.	91
Table 7.9 Difference in the cross plane CAX determined when performing lateral beam profile measurements with the gantry at 0^o and collimator at 0^o compared with those when mixed gantry and collimator errors were introduced using a PTW 60019 detector.	112
Table 7.10 Difference in the cross plane CAX determined when performing lateral beam profile measurements with the gantry at 0^o and collimator at 0^o compared with those when mixed gantry and collimator errors were introduced using a PTW 31018 detector.	112
Table 7.11 Calibration coefficients obtained by cross calibrating the detectors at a reference field 10 x 10 cm^2 and virtual msr fields of 6 x 6 cm^2 and 4 x 4 cm^2 in a LINAC using a 6 MV beam.	125
Table 7.12 Calibration coefficients obtained by cross calibrating the detectors at a reference field 10 x 10 cm^2 and virtual msr fields of 6 x 6 cm^2 and 4 x 4 cm^2 in a Co-60 beam.	125
Table 7.13 Uncertainty budget for the determination of the FOCF when using a PTW 31021 in a 1 x 1 cm^2 field size.	126
Table 7.14 Uncertainty budget for the determination of the FOF when using a PTW 60012 in a 0.6 x 0.6 cm^2 field size.	127

List of tables	Page No.
Table 7.15 Combined relative uncertainty for the FOFs determined using various PTW detectors and the FOCFs published in the IAEA TRS 483 for k = 2, equal to a confidence level of 95 %.	128

1. Introduction

1.1 Overview

Treatment of cancer using radiation therapy started after Wilhelm Conrad Röntgen discovered X-rays in 1895 (Röntgen, 1896). Before their physical properties and their biological effects were fully understood, X-rays were used to treat patients. Emil Herman Grubbe started treating patients with breast cancer using X-rays in 1896 (Serena, 2017). The most frequently treated cancers were that of the skin. Higher energy X-rays were produced in the 1910s by Coolidge (Serena, 2017). At the time, there was no scientific or clinical understanding of radiotherapy and the concept of radiation doses was introduced only in the 1920s (Serena, 2017). In 1932, an air ionisation chamber was developed, and it allowed for the approximation of the radiation dose delivered with the unit of measurement as Röntgen, which was the first radiation dose measurement unit (Thoraeus, 1932). X-ray tubes, able to deliver peak energies of up to 200 kV were developed in the period 1930 to 1950 (Serena, 2017). Therapy using neutrons started in 1938 (Svensson, 1994). Linear accelerators (linacs), Cs-137 and Co-60 teletherapy machines were simultaneously developed in the early 1950s (Thoraeus, 1961 and Podgorsak, 2005). Devices for delivering proton beams were introduced in 1970s and 1980s (Podgorsak, 2005). The end of 1980s saw the introduction of stereotactic radiosurgery (Serena, 2017). Technology developments and usage continue to outpace international traceability, the availability of dosimetry standards, and international consensus guidance and dosimetry protocols.

Radiation therapy may be the most cost-effective treatment for many cancers (Barton, 2003 and Levin, 2002) and is used to treat a wide range of tumours. Due to its success in the treatment of cancer and improved localization of small early-stage tumours, more attention is being given to small field radiotherapy techniques that can potentially spare more normal tissue near the target to reduce side effects and long-term morbidity (Aspradkis, 2011). The possibility of using small fields in radiotherapy is

made possible in part by advances in the collimation systems used. Developments in online imaging and treatment technologies used in radiotherapy have also contributed to an increase in the use of small fields (Wuerfel, 2013 and Alfonso, 2008).

There has been an increasing availability of standard-, mini- and micro-multileaf collimators on clinical linear accelerators as well as the introduction of treatment units specifically designed for stereotaxy, intensity modulated, non-standard or hypofractionation treatments, e.g. flattening filter free linear accelerators, GammaKnife™, CyberKnife™, Tomotherapy™, etc. (Alfonso, 2008). No universally accepted code of practice on dosimetry measurements for small static fields or flattening filter free beams existed until 2017 (IAEA, 2017) and no guidance for reference dosimetry in dynamic fields exists at the time of writing. This has led to incidents that could have been attributed to the absence of guidance documents for the dosimetry of small fields and users adapting codes of practice that were written for broad reference beams e.g. 10 x 10 cm^2 without fully evaluating the limitations particular to small fields. From the article published on the lessons from French accidents (Derreumaux, 2008 and 2011), some of the root causes of the incidents are linked to the incorrect determination of the absorbed dose to water in small fields, use of wrong detectors and use of wrongly measured output factors (OF). There is therefore a need to accurately determine the dosimetry in small fields.

When this project was initiated, the Institute of Physics and Engineering in Medicine (IPEM) had published a report on small field dosimetry (IPEM, 2010) but no national code of practice was published. However, there were publications that could guide small static field measurements based on investigators' experiences. The International Atomic Energy Agency (IAEA) in collaboration with the American Association of Physicists in Medicine (AAPM) published a dosimetry Code of Practice for small static field in 2017 (IAEA, 2017), referred to as IAEA TRS 483 in this work. With this publication more consistency in the implementation of the dosimetry for small static fields is expected. There is a continuous need to train users on the implementation. This code of practice uses the formalism from the broad beam codes of practice, e.g. IAEA TRS 398 and AAPM TG 51, as a basis and develops a link to a new formalism

for small static fields (IAEA, 2000 and Almond, 2010). The broad beam codes of practise are used for reference dosimetry in terms of absorbed dose to water and are based on air ionisation chambers in reference field sizes of typically 10 x 10 cm^2. The IAEA TRS 483 gives the uncertainty estimates for the field output correction factors and the beam quality correction factors for a series of detectors. In this study the uncertainty in the field output factors and the field output correction factors for the new detectors were determined. Also, the uncertainties arising from the actual measurements of field size, the reproducibility of the collimator and the positioning of a detector at a specified reference point, were determined.

1.2 Hypothesis

Small field technology has been commissioned in various clinics prior to the publication of harmonized and standardized medical physics dosimetry procedures and guidelines, which until recently, were only available for more conventional, established techniques and technologies (van der Merwe, 2017). This research will assist those using small fields in radiotherapy to better identify, quantify and assess the accuracy and uncertainties in clinical dosimetry measurements. No national quality assurance programs in small field dosimetry have been adopted by the medical physics fraternity in South Africa. Dosimetric procedures resulting in the biggest uncertainties will inform the development of an effective independent audit methodology, which can focus on the risks associated with treatment delivery and the measurement techniques that contribute higher uncertainties.

1.3 Purpose of the study

The aim of this project was to assess and quantify the accuracy of clinical dosimetry data used to commission small fields in radiotherapy and demonstrate the associated measurement uncertainties. Different parameters that are used for the characterisation and calibration of units capable of delivering small fields were

investigated in order to quantify their contribution to the uncertainty of clinical measurements. High risk areas were identified. Some of the theories applied to reference field dosimetry were revisited to ascertain they could safely be applied in small static field dosimetry. Measurement procedures that should be prioritised in national audits of treatment modalities using small fields were identified based on the data.

Small fields are used in Intensity Modulated Radiation Therapy (IMRT), stereotactic radiosurgery, Volumetric modulated arc therapy (VMAT), etc. (IPEM, 2010). During this study uncertainties in the following were determined, through measurements, in small static fields:

a) Choice of a detector and how it affects the accuracy of measurements performed.
b) Definition of the field size (equivalent/effective square) and how it affects the accuracy of measurements.
c) Determination of the central axis for small field measurements and its impact on the accuracy of the treatment data.
d) Determination, constancy and reproducibility of reference dose measurements and field output factors and considering the multileaf collimator (MLC) stability.
e) Measurement and interpretation of beam quality.
f) Measurements of small fields from different collimating systems.
g) Measurements with and without a reference detector to determine the LINAC stability.
h) Daisy chaining of small field detectors using a reference detector that was calibrated at an SSDL.

All the above led to an estimation of the overall accuracy and uncertainty in clinical dosimetry measurements of small fields. In addition, a survey of dosimetry data from users of small fields was conducted and the information used to inform requirements for the establishment of a national audit mechanism.

1.4 Structure of the thesis

This thesis has nine chapters. Chapter one gives a brief overview of the introduction of radiotherapy treatment, modalities used and the lack of international codes of practice at the time of adopting newer machines for treatment as well as the purpose and justification of the work performed.

Chapter two is a review of dosimetry concepts in radiotherapy. The review continues in chapter three and focusses on the traceability chain in dosimetry and the relevant formalism. Chapter four introduces the subject of small field dosimetry and its associated dosimetry formalism. Chapter five is a review of the uncertainty of measurements.

Chapter six gives information on the materials used and methods followed during the study. Chapter seven gives the results and discussions on the results obtained. Chapter eight is the conclusions derived from the work and other related studies. Chapter nine is the recommended areas of future research.

2. Dosimetry concepts in radiotherapy

2.1 Introduction

The International Commission on Radiation Units and Measurements (ICRU), was established in 1925. Its main objective is to develop and promote internationally accepted recommendations on radiation related quantities and units, terminology, measurement procedures, and reference data for the safe and efficient application of ionizing radiation to medical diagnosis and therapy, radiation science and technology, and radiation protection of persons. As such, they have defined quantities and units for describing radiation beams. Their recommendations are reviewed continually in order to keep abreast with the fast-growing applications of ionising radiation. In this section some of the dosimetry quantities and units used in dosimetry applicable for absorbed dose to water measurements and how they relate are described in accordance with the ICRU Report No. 85a (ICRU, 2011). Cavity theory, which is the basis for the absorbed dose measurements, is also explained.

2.2 Dosimetry quantities and units

Radiation dosimetry gives methods that may be used to quantitatively determine the energy deposited in a given medium by indirectly or directly ionising radiations. The most used dosimetric quantities in photon beams and their units are defined below.

2.2.1 Photon fluence Φ and Energy Fluence Ψ

The photon fluence, Φ, is defined as dN divided by da, where dN is the number of particles incident on a sphere of cross-sectional area da (Attix, 1968; ICRU, 2011). The unit for fluence is m^{-2}.

$$\Phi = \frac{\mathrm{d}N}{\mathrm{d}a} \qquad 2.1$$

The energy fluence, Ψ, is dR divided by da, where dR is the radiant energy incident on a sphere of cross-sectional area da (Attix, 1968; ICRU, 2011). Its unit is J m^{-2}. Radiant energy is the kinetic energy of the particles that are emitted, transferred or received in a cross-section area da.

$$\Psi = \frac{\mathrm{d}R}{\mathrm{d}a} \qquad 2.2$$

It may also be calculated, using the fluence:

$$\Psi = \frac{\mathrm{d}N}{\mathrm{d}a}E = \Phi E \qquad 2.3$$

where dN is the number of particles incident on a sphere of cross-sectional area da with energy E.

These definitions are only applicable for monoenergetic photon beams. However, photon beams used in radiotherapy are not always monoenergetic. The particle fluence spectrum and energy fluence spectrum are then used. The particle fluence spectrum in energy E, $\varphi(E)$, can be described as a function of energy (Podgorsak, 2005; ICRU, 2011)

$$\varphi(E) = \frac{\mathrm{d}\Phi}{\mathrm{d}E}(E) \qquad 2.4$$

Therefore, the total particle fluence is

$$\Phi = \int_0^{E_{\max}} \varphi(E)\mathrm{d}E \qquad 2.5$$

Using equation 2.3, the total energy fluence may be determined as

$$\Psi = \int_0^{E_{\max}} \varphi(E)E\mathrm{d}E \qquad 2.6$$

2.2.2 Attenuation coefficients

If a number of photons, N_0, is considered from a narrow beam incident on a material of thickness, x, the number of photons that passes through the material without interacting is given by (Attix, 1968; ICRU, 2011)

$$N = N_0 e^{-\mu x} \qquad 2.7$$

where μ is the linear attenuation coefficient with units cm^{-1}. μ represents a fragment of those photons removed per unit thickness (Attix, 1968). By dividing μ by the density of the material, ρ, results in μ/ρ which is independent of the density and is known as the mass attenuation coefficient. This factors out the density of the material and depends on the atomic composition of the material (Attix, 1968).

The mass attenuation coefficient, μ/ρ, of a material, for uncharged particles of a given type and energy, is the quotient of dN/N by ρdl, where dN/N is the mean fraction of the particles that experience interactions in traversing a distance dl in the material of density ρ (ICRU, 2011), thus

$$\frac{\mu}{\rho} = \frac{1}{\rho \mathrm{d}l}\frac{\mathrm{d}N}{N} \qquad 2.8$$

Its unit is $m^2\ kg^{-1}$.

When photons interact with electrons in a material, they may transfer all or part of their energy. This energy is converted into kinetic energy of the charged particles. The part of the photon energy converted into kinetic energy of charged particles per unit thickness of the absorber is given by the energy transfer coefficient, μ_{tr} (Khan, 1992). Then, the mass energy-transfer coefficient, μ_{tr}/ρ, of a material, for uncharged particles of a given type and energy, is the quotient of dR_{tr}/R by ρdl, where dR_{tr} is the mean energy that is transferred to kinetic energy of charged particles by interactions of the uncharged particles of incident radiant energy R in traversing a distance dl in the material of density ρ, (ICRU, 2011; Andreo, 2017) thus

$$\frac{\mu_{\mathrm{tr}}}{\rho} = \frac{1}{\rho \mathrm{d}l}\frac{\mathrm{d}R_{\mathrm{tr}}}{R} \qquad 2.9$$

Its unit is $m^2\ kg^{-1}$.

The mass energy-transfer coefficient, μ_{tr}/ρ, is related to the mass energy absorption coefficient, μ_{en}/ρ by

$$\frac{\mu_{\mathrm{en}}}{\rho} = \frac{\mu_{\mathrm{tr}}}{\rho}(1-\bar{g}) \qquad 2.10$$

where $\bar{g}$ is an averaged fraction of kinetic energy transferred to charged particles that is lost in radiative processes as the charged particles slow down to rest in the material

and μ_{en}/ρ represents the fraction of photon energy transferred that results in local dose deposition (ICRU, 2011; Andreo, 2017).

2.2.3 Kerma

Kerma, *K*, is a descriptor for kinetic energy released per unit mass. ICRU, 2011 defines it as the sum of the initial kinetic energies, d*E*, of all the charged particles released in a mass d*m* of a material by the uncharged particles incident on d*m*. It is

$$K = \frac{\mathrm{d}E_{tr}}{\mathrm{d}m} \qquad 2.11$$

and its unit is J kg^{-1} named gray (Gy). Kerma is only used for indirectly ionising radiation and includes the energy released by charged particles that will re-radiate as bremsstrahlung photons (Mayles, 2007).

2.2.4 Absorbed dose *D*

Absorbed dose is defined as the mean energy, $d\bar{\varepsilon}$, imparted by ionizing radiation to matter of mass d*m*, in a finite volume, by

$$D = \frac{d\bar{\varepsilon}}{dm} \qquad 2.12$$

and its unit is J kg^{-1} named, gray (Gy). It is due to the energy deposited in the material by the radiation tracks. ICRU (1980, 1998, 2011) defines the energy imparted, $\bar{\varepsilon}$, by ionising radiation to matter of a given volume as

$$\bar{\varepsilon} = R_{\mathrm{in}} - R_{\mathrm{out}} + \sum Q \qquad 2.13$$

where

R_{in} is the average radiant energy of all charged and uncharged ionizing particles that enter the volume, excluding rest mass energies;

R_{out} is the average radiant energy, excluding rest mass energies, of all charged and uncharged ionizing particles that leave the volume; and

$\sum Q$ is the average sum of all changes of the rest energy of nuclei and elementary particles that occur in the volume ($Q < 0$ for an increase in total rest energy and $Q > 0$ for a decrease in total rest energy) (ICRU, 2011).

2.2.5 Stopping power

The mean kinetic energy lost, dE, by a charged particle travelling a distance, dx, in the material is known as the linear stopping power, S, and its unit is MeV/cm.

$$S = \frac{\mathrm{d}E}{\mathrm{d}x} \qquad 2.14$$

Dividing the linear stopping power with the density of the material gives the mass stopping power, S/ρ, with unit MeV cm^2/g (Khan, 2009; Podgorsak, 2005; ICRU, 2011).

$$\frac{S}{\rho} = \frac{1}{\rho}\frac{\mathrm{d}E}{\mathrm{d}x} \qquad 2.15$$

According to the ICRU 85a, the stopping power can be expressed as:

$$\frac{S}{\rho} = \frac{1}{\rho}\left(\frac{\mathrm{d}E}{\mathrm{d}l}\right)_{\mathrm{col}} + \frac{1}{\rho}\left(\frac{\mathrm{d}E}{\mathrm{d}l}\right)_{\mathrm{rad}} + \frac{1}{\rho}\left(\frac{\mathrm{d}E}{\mathrm{d}l}\right)_{\mathrm{nuc}} \qquad 2.16$$

where

$\frac{1}{\rho}\left(\frac{\mathrm{d}E}{\mathrm{d}l}\right)_{\mathrm{col}}$ is the collision stopping power, and is due to the interactions with atomic electrons resulting in ionization or excitation;

$\frac{1}{\rho}\left(\frac{\mathrm{d}E}{\mathrm{d}l}\right)_{\mathrm{rad}}$ is the mass radiative stopping power, which is caused by the emission of bremsstrahlung in the electric fields of atomic nuclei or atomic electrons; and

$\frac{1}{\rho}\left(\frac{\mathrm{d}E}{\mathrm{d}l}\right)_{\mathrm{nuc}}$ is the mass nuclear stopping power due to the elastic Coulomb interactions in which recoil energy is imparted to atoms.

2.2.6 Charged particle equilibrium (CPE)

If a charged particle of a given type and energy, E, leaves the volume, v, and is replaced by a particle of same type and energy, in terms of expectation values, then

the charged particle equilibrium is achieved (Andreo, 2017), depicted in figure 2.1. For photons of energy ≥10 MeV, the CPE is not well approximated because the penetrating power of the generated secondary electrons increases faster than the maximum range of the primary radiation field, as the photon energy is increased. This phenomenon is termed partial charged particle equilibrium (PCPE) (Andreo, 2017).

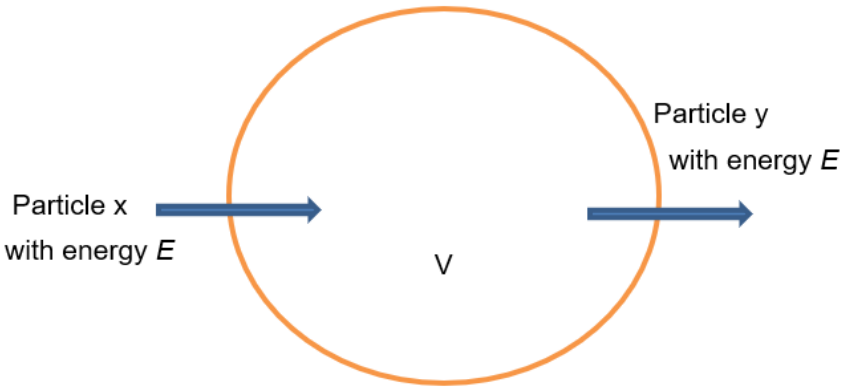


Figure 2.1 Depiction of the charged particle equilibrium. A charged particle y of a given type and energy, *E*, leaves the volume, *v*, and is replaced by a charged particle x of the same type and energy.

2.3 Relations between some of the dosimetric quantities

2.3.1 Energy fluence and kerma

For a photon beam travelling across a medium, at any point in a medium, kerma is directly proportional to the photon energy fluence resulting in

$$K = \Psi \frac{\bar{\mu}_{\mathrm{tr}}}{\rho} \qquad 2.17$$

where $\bar{\mu}_{\mathrm{tr}}/\rho$ is the mass energy transfer coefficient for the medium averaged over the energy fluence spectrum of photons (Khan, 1992). Combining equations 2.10 and 2.18 leads to

$$K = \Psi \frac{\bar{\mu}_{\mathrm{en}}}{\rho} \Big/ (1 - \bar{g}) = \Psi \frac{\bar{\mu}_{\mathrm{en}}}{\rho} + \Psi \left(\frac{\bar{\mu}_{\mathrm{en}}}{\rho}\right) \frac{\bar{g}}{1-\bar{g}} = K_{\mathrm{col}} + K_{\mathrm{rad}} \qquad 2.18$$

K_{col} is as a result of Coulomb force interactions with atomic electrons, which leads to the production of electrons that lose energy as ionization in or near the electron tracks in the medium. K_{rad} is the production of radiative photons as the secondary charged particles slow down and interact in the medium (Podgorsak, 2005).

2.3.2 Energy fluence and absorbed dose

At a point in a medium, the absorbed dose to a medium, D_{med}, will be equal to the collision kerma, K_{col}. This is only true when there is charged particle equilibrium at that point and because most of the radiative photons escape the volume of interest. This implies, for a monoenergetic beam (Andreo, 2017, Podgorsak, 2005),

$$D_{\mathrm{med}} = (K_{\mathrm{col}})_{\mathrm{med}} = \left(\Psi \frac{\bar{\mu}_{\mathrm{en}}}{\rho}\right)_{\mathrm{med}} = \left(\Phi E \frac{\bar{\mu}_{\mathrm{en}(E)}}{\rho}\right)_{\mathrm{med}} \qquad 2.19$$

For a photon fluence spectrum, Φ_E, under CPE, D_{med} becomes

$$D_{\mathrm{med}} = \int_0^{E_{\max}} [\Phi_E]_{\mathrm{med}} E \left[\frac{\bar{\mu}_{\mathrm{en}(E)}}{\rho}\right]_{\mathrm{med}} \mathrm{d}E \qquad 2.20$$

Also, the absorbed dose to medium, D_{med}, and the electron fluence in the medium, Φ_{med}, is correlated as follows:

$$D_{\mathrm{med}} = \Phi_{\mathrm{med}} \left(\frac{S_{\mathrm{col}}}{\rho}\right)_{\mathrm{med}} \qquad 2.21$$

where $(S_{col}/\rho)_{med}$ is the unrestricted mass collision stopping power of the medium for the energy of the electron. This is only valid when radiative photons escape the volume of interest and there is a charged particle equilibrium (CPE) of secondary electrons (Podgorsak, 2005).

2.4 Cavity theory

The aim of dosimetry is to know the dose absorbed at a specific point in a medium. A detector is used to perform these measurements. One of the challenges is that most of the detectors are made of material that is different from that of the medium in which the measurements are performed. Also, detectors do not measure dose to medium directly, an interpretation of the detector response is needed. Cavity theory aims to

establish the relation between the dose measured in the medium in the absence of the detector, D_{med}, and the dose measured by the detector, D_{det}, in a beam quality, Q, see Figure 2.2. The name “cavity” is historical as ionisation chambers that were mainly used at the time, were gas filled (Mayles, 2007).

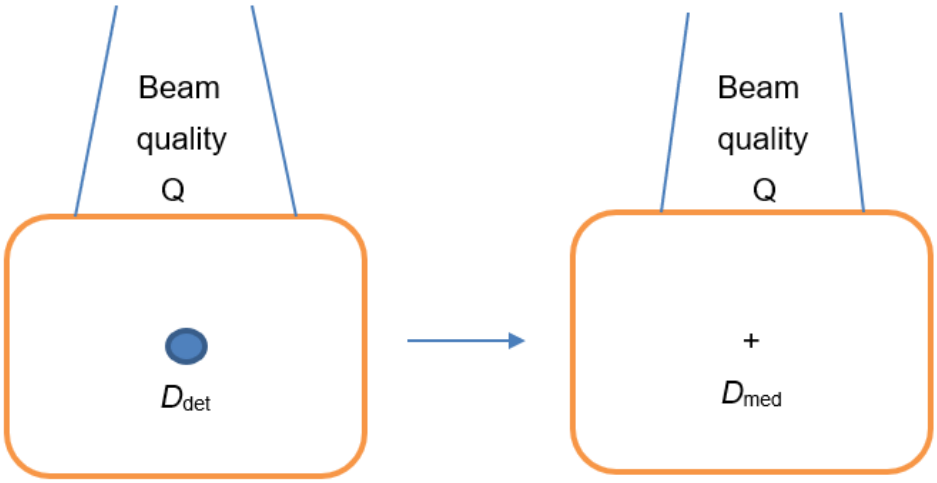


Figure 2.2 Depiction of a detector that is introduced into a medium on the left thus giving D_{det} for a given exposure to radiation of beam quality, Q, and then being converted into the dose D_{med} at point + in the absence of the detector (Mayles, 2007).

2.4.1 Cavity theory for large photon detectors

For a monoenergetic photon beam with energy fluence, Ψ, incident on a medium, med, at depth z, the dose to the medium (provided there is charged particle equilibrium) at depth z is given by:

$$D_{\mathrm{med,z}} = \Psi_{\mathrm{med,z}} \left(\frac{\mu_{\mathrm{en}}}{\rho}\right)_{\mathrm{med}} \qquad 2.22$$

When the sensitive volume of a detector is placed at depth z in that phantom, the absorbed dose averaged over the detector volume will be given by:

$$\bar{D}_{\mathrm{det,z}} = \Psi_{\mathrm{det,z}} \left(\frac{\mu_{\mathrm{en}}}{\rho}\right)_{\mathrm{det}} \qquad 2.23$$

on condition that the volume of the detector is large enough for charged particle equilibrium. $\Psi_{\mathrm{det,z}}$ is the energy fluence in the detector. From equations 2.22 and 2.23:

$$f_Q = \frac{D_{\mathrm{med,z}}}{\bar{D}_{\mathrm{det,z}}} = \frac{\Psi_{\mathrm{med,z}}\left(\frac{\mu_{\mathrm{en}}}{\rho}\right)_{\mathrm{med}}}{\Psi_{\mathrm{det,z}}\left(\frac{\mu_{\mathrm{en}}}{\rho}\right)_{\mathrm{det}}} \qquad 2.24$$

If the detector does not perturb the photon fluence in the medium then $\Psi_{\mathrm{med,z}} = \Psi_{\mathrm{det,z}}$, and equation 2.24 becomes:

$$f_Q = \frac{D_{\mathrm{med,z}}}{\bar{D}_{\mathrm{det,z}}} = \frac{\left(\frac{\mu_{\mathrm{en}}}{\rho}\right)_{\mathrm{med}}}{\left(\frac{\mu_{\mathrm{en}}}{\rho}\right)_{\mathrm{det}}} \qquad 2.25$$

Photon energies used in practise are however never monoenergetic. For a spectrum of photon energies equation 2.25 can be written:

$$f_Q = \frac{D_{\mathrm{med,z}}}{\bar{D}_{\mathrm{det,z}}} = \frac{\int_0^{E_{max}} E \frac{\mathrm{d}\Phi_{\mathrm{med,z}}}{dE}\left(\frac{\mu_{\mathrm{en}(E)}}{\rho}\right)_{\mathrm{med}} \mathrm{d}E}{\int_0^{E_{max}} E \frac{\mathrm{d}\Phi_{\mathrm{med,z}}}{dE}\left(\frac{\mu_{\mathrm{en}(E)}}{\rho}\right)_{\mathrm{det}} \mathrm{d}E} \qquad 2.26$$

This ratio is also known as the ratio of the mass-energy absorption coefficient of the medium to detector (Nahum, 2009 and Andreo, 2017).

2.4.2 Bragg-Gray cavity theory

When a detector is small compared to the secondary electron ranges, as shown in figure 2.3, and its size is small enough not to perturb the electron tracks, the electron fluence is ideal to use to derive the absorbed dose in that small detector. This is because the detector size is too small to establish the charged particle equilibrium and thus cannot use energy fluence.

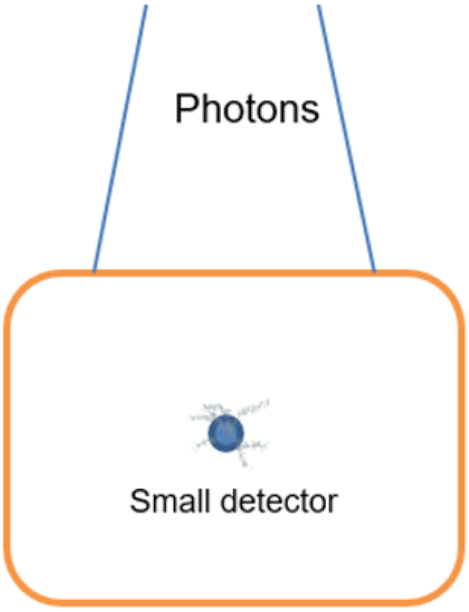


Figure 2.3 Depiction of a small detector in a medium irradiated with a photon beam. The detector is small compared to the secondary electron ranges (Nahum, 2009).

Using equation 2.21,

$$f_Q = \frac{D_{\mathrm{med,z}}}{\bar{D}_{\mathrm{det,z}}} = \frac{\Phi_{\mathrm{med,z}}\left(\frac{S_{\mathrm{col}}}{\rho}\right)_{\mathrm{med}}}{\Phi_{\mathrm{det}}\left(\frac{S_{\mathrm{col}}}{\rho}\right)_{\mathrm{det}}} \qquad 2.27$$

Assuming that by putting the detector in the medium does not disturb the electron fluence existing in the undisturbed medium, then $\Phi_{\mathrm{med,z}} = \Phi_{\mathrm{det}}$ yielding

$$\frac{D_{\mathrm{med}}}{\bar{D}_{\mathrm{det}}} = \frac{\left(\frac{S_{\mathrm{col}}}{\rho}\right)_{\mathrm{med}}}{\left(\frac{S_{\mathrm{col}}}{\rho}\right)_{\mathrm{det}}} \qquad 2.28$$

This ratio is known as the mass stopping power ratio. For a spectrum of electron energies

$$\frac{D_{\mathrm{med,z}}}{\bar{D}_{\mathrm{det,z}}} = s^{\mathrm{BG}}_{\mathrm{med,det}} = \frac{\int_0^{Emax}(\Phi_{\mathrm{E}})_{\mathrm{med,z}}\left(S_{col}(E)/\rho\right)_{med}\mathrm{d}E}{\int_0^{Emax}(\Phi_{\mathrm{E}})_{\mathrm{med,z}}\left(S_{col}(E)/\rho\right)_{det}\mathrm{d}E} \qquad 2.29$$

Detectors that respond to the electron fluence that exists in the absence of any detector and do not perturb that electron fluence, are known as Bragg-Gray cavities

(Mayles, 2007). The following conditions must be met for a detector to be a Bragg-Gray cavity (Andreo, 2017):

a) The cavity is small when compared with the range of charged particles incident on it and its presence does not perturb the charged particle fluence existing in the absence of the cavity.
b) The absorbed dose in the cavity is deposited only by the charged particles crossing it.

The attainment of these conditions is dependent on electron energy spectrum, as well as the size and material of a detector.

2.4.3 Spencer-Attix formalism

Bragg-Gray cavity theory assumes that for an electron crossing the cavity all the energy dissipated along its track is locally deposited. Spencer and Attix extended the Bragg-Gray cavity theory to take into consideration the ranges of the secondary electrons, δ. A two-group representation and a cut off energy Δ, were introduced. All electrons with energy higher than Δ are considered part of the fluence spectrum incident on the cavity, whether they are primary electrons or δ rays. All energy losses below Δ are considered to deposit their energy in the cavity and all losses above Δ, to escape the cavity (Nahum, 1978 and 2009). The incident fluence of electrons, that contains all generations of electrons, Φ^{total}, is identical to that present in the uniform medium. This is shown in figure 2.4 and leads to a restricted stopping power ratio given by:

$$\left[\frac{\bar{L}_\Delta}{\rho}\right]_{\text{det}}^{\text{med}} = \frac{\int_\Delta^{E\max}\left(\Phi_E^{\text{tot}}(E)\right)_{\text{med}}\left[{}^{L_\Delta(E)}/_{\rho}\right]_{\text{med}}\mathrm{d}E + \left\{\Phi_E^{tot}(\Delta)\left[{}^{S_{col}(\Delta)}/_{\rho}\right]_{\text{med}}\Delta\right\}}{\int_\Delta^{E\max}\left(\Phi_E^{\text{tot}}(E)\right)_{\text{med}}\left[{}^{L_\Delta(E)}/_{\rho}\right]_{\text{det}}\mathrm{d}E + \left\{\Phi_E^{tot}(\Delta)\left[{}^{S_{col}(\Delta)}/_{\rho}\right]_{\text{det}}\Delta\right\}} \qquad 2.30$$

and then

$$f(Q) = \frac{D_{\text{med}}}{\bar{D}_{\text{det}}} = \frac{\int_\Delta^{E\max}\Phi_E^\delta\left({}^{L_\Delta(E)}/_{\rho}\right)_{\text{med}}\mathrm{d}E + \left[\Phi_E(\Delta)\left({}^{S_{col}(\Delta)}/_{\rho}\right)_{\text{med}}\Delta\right]}{\int_\Delta^{E\max}\Phi_E^\delta\left({}^{L_\Delta(E)}/_{\rho}\right)_{\text{det}}\mathrm{d}E + \left[\Phi_E(\Delta)\left({}^{S_{col}(\Delta)}/_{\rho}\right)_{\text{det}}\Delta\right]} \qquad 2.31$$

where $\left\{\Phi_E^{tot}(\Delta)\left[{}^{S_{col}(\Delta)}/_{\rho}\right]_{\mathrm{med}}\Delta\right\}$ and $\left\{\Phi_E^{tot}(\Delta)\left[{}^{S_{col}(\Delta)}/_{\rho}\right]_{\mathrm{det}}\Delta\right\}$ account for the energy deposited by electrons with initial energies between Δ and 2Δ (Nahum, 1978 and 2009).

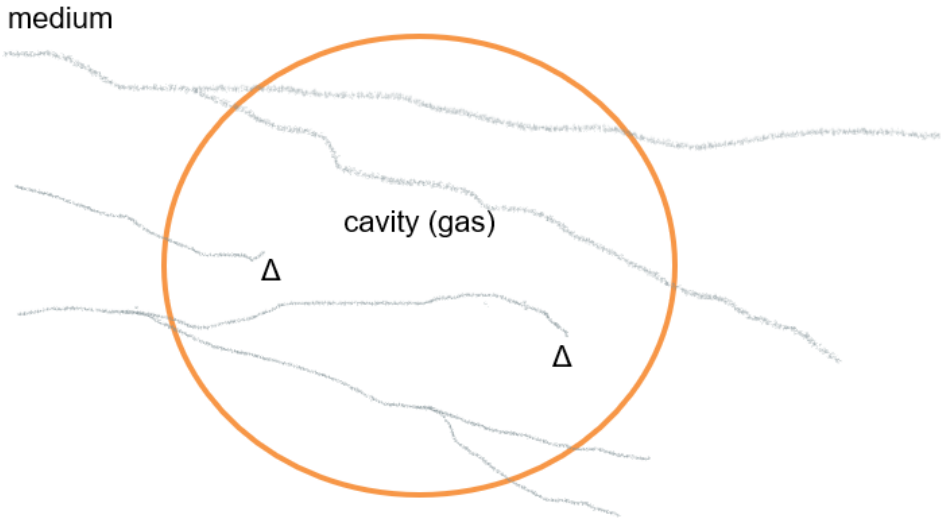


Figure 2.4 A graphical representation of the energy deposited in a cavity following the Spencer-Attix energy deposition model. The incident fluence of electrons, that contains all generations of electrons, Φ^{total}, is identical to that present in the uniform medium (Nahum, 2009).

3. Traceability of measurements in dosimetry for absorbed dose

3.1 Introduction

The international measurement system provides a framework for worldwide consistency by providing traceability through the calibration of equipment used to perform measurements. The international measurement system was established in 1875 when the Metre Convention, a treaty, was signed by representatives of seventeen nations (BIPM, 2006 and McDowell, 1997). The treaty allowed for the establishment and funding of the International Bureau of Weights and Measures, the BIPM. The BIPM is under the authority of the General Conference on Weights and Measures (CGPM) and the supervision of the International Committee for Weights and Measures (CIPM). The convention was slightly modified in 1921 but remains the foundation of the international agreement on units of measurements. On the 20 May 2019, when the revised international system of units (SI) was adopted by various countries, the BIPM had fifty-nine (59) member states (BIPM, 2019).

The CIPM currently has ten consultative committees that give inputs to the BIPM strategy through their technical expertise. The consultative committee for ionising radiation (CCRI), through its working group for dosimetry standards, is a group of laboratories that has activities related to the standards in dosimetry for absorbed dose to water in photon beams. The membership is decided by the CIPM, based on the participation of the laboratory in research and international comparisons (BIPM, 2018). Currently this committee is dominated by primary standard dosimetry laboratories (PSDL) owing to their research and development activities for dosimetry standards.

The International Vocabulary of Metrology, known as VIM, (BIPM, 2012) defines Primary standards as standards established using a primary reference measurement procedure, or created as an artefact, chosen by convention. These are instruments of the highest metrological quality that permit determination of a unit from its definition, the accuracy of which has been verified by comparison with comparable standards of other institutions at the same level (IAEA, 2000). The primary standards for dosimetry

that are developed and/or maintained by the PSDLs vary mainly between ionometric, graphite calorimeters to water calorimeters (Seuntjens, 2009). The BIPM maintains an ionometric primary standard that is used as an international reference standard for absorbed dose to water in a ^{60}Co beam (Burns, 2018). A calorimeter has been developed also and is used for comparisons in absorbed dose to water using high energy linear accelerators and Co-60 machines (Kessler, 2019).

For any measurements to be of quality and acceptable internationally, they need to be traceable to the international measurement system through an unbroken chain of calibration linked to a primary standard that has been compared internationally. For countries that do not have primary standards but are member states of the BIPM, their secondary standards may be calibrated at the BIPM directly against the primary standard. The IAEA, as an International Organisation with an agreement with the BIPM, also obtains its calibration traceability for absorbed dose to water from the BIPM through the calibration of its secondary standards. Secondary standards are reference Instruments calibrated by comparison with a primary standard (IAEA, 2000). The IAEA calibrates secondary standards for those countries that are not signatory to the metre convention treaty but are member states to the IAEA. In countries where there is no laboratory, the IAEA may calibrate end user equipment. Secondary Standard Dosimetry Laboratories (SSDLs) generally calibrate the end user equipment. There are some of the PSDLs that also play this role.

Comparisons are organised by the BIPM with national metrology institutes to ascertain measurement equivalence for primary standards, in various fields. In dosimetry, the comparisons for absorbed dose to water are conducted in a Co-60 machine and/or linear accelerator using one or more transfer reference standards because most primary standards are not easily transportable. The primary standard laboratories that participate in the comparisons with the BIPM, also participate in comparisons with members of their regional metrology organisation and can thereby provide a link for secondary standard laboratories to the international system. Degrees of equivalence are calculated for each comparison thus linking all participating laboratories. Comparisons are available also for end user in the form of audits. These audits assist

with the ensuring quality in radiotherapy and cover more than just reference measurements and cover the whole treatment chain.

3.2 Primary standards for absorbed dose to water

The PSDLs establish one or more primary standards for absorbed dose to water depending on their interest and capabilities. The PSDL then compares its standard to that of the BIPM to establish confidence and degrees of equivalence. Previously, absorbed dose to water standards were developed for Co-60 beams but more PSDL's now have access to linear accelerators and can provide calibrations in high energy photons and electrons (Seuntjens, 2009 and Pickard 2010).

The most direct and used method for the determination of absorbed dose to water for high energy photon beams is the calorimeter (Andreo, 2017). Calorimetry measurements for absorbed dose are not dependent on a characterised ionising radiation field, but their calibration traceability is entirely based on quantities such as temperature and electric power (Seuntjens, 2009; Andreo, 2017). Calorimetry rely on the measurements of the temperature change in the calorimeter medium. The absorbed energy appears as heat for most material (Andreo, 2017). Assumption is made that the energy deposited by ionising radiation appears as a temperature rise, leading to the mean absorbed dose to a medium of choice, D_m given by:

$$D_m = c_m \Delta T \qquad (3.1)$$

where c_m is the specific heat capacity of the absorbing material at constant pressure and ΔT is the temperature rise measured at the core, resulting from absorbed dose D_m (Seuntjens, 2009; Andreo, 2017). There are instances when the full conversion of the energy deposition into temperature rise is not accomplished. This is known as heat defect (Seuntjens, 2009). This must be well understood and taken into consideration for that calorimeter to be used as a primary standard. Primary standards for temperature are required to be able to measure the temperature change accurately. Depending on the calorimeter design, there are other corrections that need to be considered. The National Metrology Institutes (NMI's) have focused their

developments of calorimeters using low-Z materials water and graphite (Allisy-Roberts, 2005). Each material has its own advantages and challenges which are discussed in the following sections.

3.2.1 Water calorimeter

Water calorimeters are operated at 4 ^{o}C to effectively eliminate convective motion of the water that would disturb the temperature rise at the reference point of measurement (Andreo, 2017; Muir, 2017). This temperature, 4 ^{o}C, is where water is at its maximum density. For the calorimeter to be useful, very low uncertainties in temperature measurements are required. This is because very small increases in temperature are observed from radiation, 0.5 mK for an absorbed dose of 2 Gy (Muir, 2017). The temperature rise is measured inside a sealed small volume with highly purified water. Because of the low thermal diffusivity of water, the temperature distribution stays the same long enough to allow for accurate measurements. Having the purified water in a sealed glass detection vessel helps deal with challenges linked with handling the radiolysis induced defect and helps control the water purity (Andreo, 2017). Several correction factors need to be considered when determining the absorbed dose using the water calorimeter. Taking these into consideration, the measurement equation is given by:

$$D_w = c_w \Delta T k_c k_r k_p k_T \left(\frac{1}{1-h}\right) \qquad 3.2$$

where

c_w is the specific heat capacity for water, at constant pressure, which is 4205 J kg^{-1} K^{-1} at 4 ^{o}C (4182 J kg^{-1} K^{-1} at 20 ^{o}C) (Andreo, 2017);

k_c is a correction factor that corrects for the heat transport effects occurring during and after the irradiations;

k_r is a correction for the non-uniformity of the lateral dose distribution and is dependent on the position of the thermistors;

k_p is a radiation perturbation correction factor to account for the change of $D_{w,}$ at the reference point, due to the presence of the calorimetric detector;

k_T is a factor correcting for the effect due to the difference in the water temperature between the calorimetric measurements (4°C) and the ionization chamber calibrations (20°C).

There are now water calorimeters that can determine absorbed dose to water with an estimated standard uncertainty of 0.5 %, for a 95 % confidence level k = 2, for conventional reference fields, having taken into consideration all the correction factors (BIPM KCDB, 2019). Some of the PSDLs have performed measurements in small fields using their water calorimeters and the limitations are briefly discussed in 4.3.1.

3.2.2 Graphite calorimeter

Graphite calorimeters are designed such that the inner core, made of graphite, is connected to thermistors and placed inside a graphite jacket. There is a thermistor connected to the jacket independent of the one connected to the core. This assembly is then placed inside another graphite jacket which is then placed in a graphite phantom. These are each separated by vacuum gaps and reflective surfaces to minimise the heat exchange between the core and its surroundings as much as possible. This is a design that was proposed in 1974 by Domen and Lamperti, simplified (Seuntjens, 2009 and Andreo, 2017). The thermistors connected to the core and jacket are chosen and placed such that they do not significantly disturb the temperature rise. These thermistors are then connected to a DC or AC bridge, with the DC bridge being less noisy than the DC bridge (Seuntjens, 2009). Electrical heating is used and the response in the temperature is directly linked with electrical energy measurements.

There are three major modes of operating the calorimeter that are used by most laboratories (Seuntjens, 2002).

- The core and jacket temperature rise are kept the same during irradiation to minimise the heat flow. This is known as the quasi adiabatic mode.
- The temperature drift is kept at zero as the heat loss from the core is kept constant. This is known as the isothermal mode.

- The heat loss compensation mode where the temperature from the core and the jacket are added together to determine the heat loss of the core.

The uncertainty of measurement that may be obtained using a graphite calorimeter for determining absorbed dose to water is estimated to be 0.3 % to 0.5 %, for a 95 % confidence level k = 2, (BIPM KCDB, 2019) varying per laboratory. This is taking into consideration the conversion from absorbed dose to graphite to absorbed dose to water that needs to be performed. Measurements using a graphite calorimeter directly gives absorbed dose to graphite. Ionisation chambers and Monte Carlo simulations are mainly used for the conversion to absorbed dose to water.

There have been developments of graphite calorimeters for use in small fields at the National Physical Laboratory (NPL) in UK (Duane, 2012) and at McGill University (Renaud, 2013). But to date there is no known international comparison performed with the BIPM using graphite calorimeters for small fields.

3.2.3 Primary cavity ionisation chambers

Primary standard laboratories also developed cavity ionisation chambers for use as primary standards. Very low currents in the picoampere range are measured. This speaks to the design of the electrometer, cables and ionisation chamber that is required to ensure the leakage current is kept minimal. The chamber consists of a solid outer wall that is usually made of graphite and a collecting electrode. When the chamber is placed in a photon beam, the photons interact with the wall and produce secondary electrons which travel through the cavity and interact with the gas in the cavity and produce charge. The collecting electrode, which is usually positioned at the centre of the cavity, measures this ionisation charge when a polarising voltage is applied. The chamber design is such that its wall and the electrode are isolated from each other (Andreo, 2017). The volume of the cavity of the ionisation chamber together with other required correction factors like the wall correction factor, must be known precisely for it to be used as a primary standard.

The BIPM uses a cavity chamber to determine the absorbed dose to water for Co-60 beams. It is a plane parallel chamber with a disc shaped graphite collecting electrode at the centre of the measuring volume. The cavity chamber is covered with a thin polyethylene sleeve and positioned in a water phantom with its centre at the reference point for absorbed dose to water measurements (Picard, 2011a, 2011b, 2009). There is currently no studies of using primary cavity ionisation chambers in small fields.

3.3 Secondary standards for absorbed dose to water

Reference standards are used for transferring traceability from the primary standards to the secondary standards laboratories. Reference standards are defined, in VIM, as measurement standards designated for the calibration of other measurement standards for quantities of a given kind in a given organization or at a given location (BIPM, 2012). For absorbed dose to water measurements, the reference standard is a cylindrical ionisation chamber with a vented cavity volume between 0.1 cm^3 and 1 cm^3, an internal air cavity diameter not greater than 7 mm and an internal length not greater than 25 mm. The wall material should be of low atomic number and of thickness less than 0.1 g/cm^2.

Graphite walled ionization chambers usually have better long-term stability and more uniform response than plastic walled chambers (IAEA, 2000). As the measurements are performed in water, the chamber must be waterproof or have a waterproof sleeve. Even though there are well established easy to use reference standards for broad beams, this has not been well established for the small field measurements. There is also no one reference standard that can be used to cover broad fields and small fields that will be easy to use in a clinical set up. EBT3 film may be ideal for measuring from broad beams to small beams but considerable expertise and time is still needed to handle them. This is the situation with other detectors that may be used in small field dosimetry measurements (Casar, 2018). There are new detectors that are being introduced and still need to be characterised for full use in small field and their field output correction factor (FOCF) obtained together with their beam quality correction factors.

3.4 Dosimetry formalism

All beams need to be fully characterised before they are used clinically. This entails determining the lateral beam profiles, measuring the central axis percentage depth dose (*PDD*), the tissue phantom ratios (*TPR*) or tissue maximum ratios (*TMR*) and determining the output factor (OF), required for the calculation of treatment times. It also involves calibration of the beam under reference conditions described by guidance documents like the IAEA TRS 398 (IAEA, 2000) and the AAPM TG 51 (Almond, 1999 and McEwen, 2014). In this section the focus is on formalisms used for the calibration of the beam and determination of the output factors.

3.4.1 Calibration at a Secondary Standard Laboratory in a Co-60 beam

Calibration of reference standards in terms of absorbed dose to water is performed in a water phantom, at a reference depth of 5 g/cm^2, with a source to chamber distance of 100 cm, using a field size of 10 x 10 cm^2, in a Co-60 source at primary and secondary standard laboratories. Although there are primary standard laboratories that do offer the calibrations in high energy linear accelerator beams, there are however very limited number of secondary standard dosimetry laboratories that have access to them for performing calibrations. The majority that have their own facilities perform calibrations in Co-60. The primary and secondary standard laboratories perform calibrations under similar reference conditions. The absorbed dose to water under these reference conditions in a Co-60 beam using a reference standard is given by:

$$D_{w,Q_o}^{f_{ref}} = M_{Q_o}^{f_{ref}} N_{D,w,Q_o}^{f_{ref}} \qquad (3.3)$$

where:

$M_{Q_o}^{f_{ref}}$ is the electrometer reading obtained using a reference standard and its associated electrometer corrected for all influence quantities (temperature, pressure, humidity, polarity, ion collection efficiency, etc.) under reference conditions in a Co-60 beam designated as beam quality Q_o;

$N_{D,w,Q_o}^{f_{ref}}$ is the calibration coefficient, in terms of absorbed dose to water, supplied by the primary standard laboratory in a Co-60 beam.

When a user instrument, *uut*, is placed in the beam under the same reference conditions, the absorbed dose to water is then obtained by:

$$D_{w,Q_o}^{f_{uut}} = M_{Q_o}^{f_{uut}} N_{D,w,Q_o}^{f_{uut}} \quad (3.4)$$

where:

$M_{Q_o}^{f_{uut}}$ is the electrometer reading obtained using a user instrument and its associated electrometer and corrected for all influence quantities (temperature, pressure, humidity, polarity, ion collection efficiency, etc) under reference conditions in a Co-60 beam;

$N_{D,w,Q_o}^{f_{uut}}$ is the calibration coefficient, in terms of absorbed dose to water, for the user instrument. Because

$$D^{ref}{}_{w,Q_o} = D^{uut}{}_{w,Q_o} \quad (3.5)$$

combining equations (3.3) and (3.4) gives

$$N^{uut}{}_{D,w,Q_o} = \frac{M^{ref}{}_{Q_o}}{M^{uut}{}_{Q_o}} N^{ref}{}_{D,w,Q_o} \quad (3.6)$$

The uncertainties associated with this calibration from secondary standard laboratories can range from 0.8 % to 2 %, for a 95 % confidence level k = 2, (BIPM KCDB, 2019) depending on laboratory capabilities and their source of calibration traceability.

3.4.2 Reference beams

As it is not all the calibration laboratories that can perform calibrations in beam qualities like those used in the clinics, a factor is introduced to correct for the effects of the difference between the reference beam, Q_o, and the user beam, Q. Thus, the absorbed dose to water is determined using the formula (IAEA, 2000):

$$D_{w,Q} = M_Q N_{D,w,Q_o} k_{Q,Q_o} \quad (3.7)$$

Where:

M_Q is the electrometer reading in the end user beam corrected for all influence quantities (temperature, pressure, humidity, polarity, ion collection efficiency, etc.), under reference conditions as stipulated by the calibrating laboratory;

N_{D,w,Q_o} is the calibration coefficient, in terms of absorbed dose to water, in a Co-60 beam, supplied by the calibrating laboratory;

k_{Q,Q_o} is a factor to correct the calibration coefficient for the difference between the reference beam quality Q_o and the user beam Q. These may be provided from measurements by some primary standard laboratories or calculated using Monte Carlo or the data published in guidance documents like TRS-398 (IAEA, 2000). The data in the guidance documents like TRS 398 takes into consideration many published data points and eliminates possible outliers. The combined standard uncertainty associated with the calculated k_Q values published in the TRS 398 is estimated to be 0,8 % for Co-60 and 1 % for high energy photon beams (IAEA, 2000) and for those published in the AAPM's TG-51 the estimated uncertainty is 0.5 % (McEwen, 2014).

3.4.3 Cross calibration at the user's beam

The end users rely on the calibration of their cylindrical chambers in a 10 x 10 cm^2 reference beam as required by the IAEA TRS 398 or other similar guidance documents. The user then calibrates their beams using the calibration coefficient obtained from the PSDL or SSDL. End users may have a reference chamber that is sent to the PSDL or SSDL for calibration and then use that chamber to cross calibrate field instruments that are used for routine measurements, including those used for small field measurements. Conditions of measurement set up for cross calibration must be similar or as close as possible to those of when the calibrations were performed at the PSDL or SSDL. If this is not possible appropriate corrections must be applied i.e. if the beam quality is different from the calibration conditions, a beam quality correction factor needs to be applied (referred to as k_{Q,Q_0}). Equations (3.3) to (3.7) are used to determine the calibration coefficient for the field instrument, where *uut* will be the field instrument and the reference instrument is the one calibrated at

the SSDL. There are currently no calibration capabilities published in the BIPM CMC database that cover small fields (BIPM KCDB, 2019). Currently the end user must obtain traceability in reference fields and then transfer it to the small field through daisy chaining.

3.4.4 Output factor measurements

Output factor is the variation in dose at a reference depth with field size and normalized to a reference field size. For broad beams, it is determined as the ratio of the dosimeter readings measured under reference conditions and corrected for influence quantities to the dosimeter readings measured under non reference conditions and corrected for all influence quantities (IAEA, 2000). The measurements are usually performed at a reference depth of 10 cm in water for high energy photon beams, and the reference field size is 10 x 10 cm^2 (IAEA, 2000). The use of the ratio of the dosimeter readings only for output factor measurements is true only for broad beams because the dosimetry quantities are not influenced by field size (IAEA, 2017).

3.4.5 Beam quality index

The use of some of the detectors for measuring absorbed dose needs the user to know the spectral fluence distribution of the beam because of their energy dependency. Because of the practical challenges in measuring the spectrum in the clinical beams, the codes of practice suggested the use of the beam quality indices (Sauer, 2009). The determination of beam quality indices forms part of the quality assurance programme. The data is collected during the commissioning process and is used to verify the beam characteristics periodically.

There is no beam quality index that satisfies all possible requirements of being a unique index for the whole energy range of accelerators used in hospitals (IAEA, 2000). Some codes of practice e.g. AAPM TG 51 (Almond, 1999) use the percentage depth dose, $PDD(10)_X$, which is defined as the photon component of the percentage

depth dose at 10 cm depth for a field size of 10 x 10 cm^2 on the surface of a phantom at a source to surface distance (SSD) of 100 cm (Palmans, 2012 and Almond, 1999).

The IAEA TRS 398 (IAEA, 2000) uses the tissue phantom ratio, $TPR_{20,10}(10)$, which is defined as a ratio of the absorbed dose to water for a field size of 10 × 10 cm^2 at depths of 20 g/cm^2 and 10 g/cm^2, determined at a source to chamber distance of 100 cm (IAEA, 2000). $TPR_{20,10}(10)$ is independent of electron contamination from the incident beam (IAEA, 2000). In addition, a chamber is only positioned once in line with the beam centre and only the water level is varied during measurements and this minimizes systematic positioning errors.

The relation between these two beam quality indices for broad flattened beams is (IAEA, 2000; Palmans, 2012 and Followill, 1998):

$$TPR_{20,10}(10) = 1.2661\ PDD_{20,10} - 0.0595 \qquad (3.8)$$

where $PDD_{20,10}$ is the ratio of the percent depth dose at 20 cm and 10 cm for a field size of 10 x 10 cm^2 defined at the phantom surface with a Source to Surface Distance (SSD) of 100 cm.

The primary standard laboratories use these beam quality indices to specify the beam quality in which a detector was calibrated. Also, they are needed for selecting the beam quality correction factor, k_{Q,Q_o}, for when a detector is calibrated at a beam that is different than the beam used in the clinic.

4. Physics of small field dosimetry

4.1 Introduction

Small fields have been used for treatment in radiotherapy for many years. They have been used in stereotactic radiosurgery for several decades and more recently, been integrated into standard technologies. The absence of an international code of practice brought challenges to the user community as there was no co-ordinated guidance and individuals relied on what the manufacturers recommended or what they read in published papers as guidance for dosimetry measurements. As a result, the data measured at various centres compared by several authors showed significant differences, e.g. Das et al reported differences of up to 12 % for output factors measured in collimated photon beams for field diameters of 20 mm (Das, 2008). Derreumaux et. al. reported variations of 5 % to 10 % in output factors for field sizes equal to or greater than 12 mm x 12 mm and around 30 % for the smallest field size of 6 mm x 6 mm (Derreumaux, 2008 and 2011). Li et al reported differences in measured percentage depth dose (*PDD*) for 6 mm x 6 mm fields greater than 5 % (Li, 2006). These differences indicate the lack of consistency and accuracy in the measurements performed for small fields and could lead to undesired outcome of the treatment as the patients may be under treated or over exposed. The differences observed could have been due to the lack of co-ordinated approach in dosimetry for small fields as there was no international guidance documents and using detectors that might not be suitable for small static fields (Derreumaux, 2008 and 2011).

The bigger the variations in the data being compared the less the confidence in that data. The intention is to be able to deliver a dose to a patient with an accuracy that is within 5 % to the prescribed dose in line with the ICRU report 24 recommendation (ICRU, 1976). Thus, the accuracy in each step in the measurement chain leading to the treatment delivery must be minimised so that the desired accuracies are met with the desired confidence levels. The AAPM Task Group 142 report on Quality assurance of medical accelerators recommends that the relative dose parameters such as output factors be maintained with tolerances ≤ 2 % (Klein, 2009).

Guidance documents for dosimetry in broad beams were readily available like IAEA TRS 398 and AAPM TG 51. These cannot be used for dosimetry in small fields because the reference conditions required cannot be established for all the equipment. Also, the required FOCF for small fields are not available in those publications. In October 2008, a new formalism for the dosimetry of small and composite fields was suggested to the medical physics user community by the working group established by the IAEA in collaboration with the AAPM (Alfonso, 2008). The formalism was published with the intention to get the medical physics community to submit their comments before a code of practice was developed. This formalism provided a link from broad beam dosimetry formalism, to small static beams dosimetry. In June 2010 the Institute of Physics and Engineering in Medicine published its report on the Small Field MV Photon Dosimetry (IPEM, 2010).

Even though there were papers published on small field dosimetry, challenges with the published data showed inconsistencies and/or lack of information on whether the field size quoted in the publication is the geometrical field size or the irradiation field. There was lack of consistency in the distance used from the source whether it was source to detector or source to surface distance and also in the depth of measurements used (IAEA, 2017).

The IEC 60788 (IEC TR 60788, 2004; IAEA, 2017) defines the geometrical field size as the geometrical projection of the collimator opening by the radiation source on a plane perpendicular to the axis of the beam and the irradiation field size is defined in terms of the dimensions of an area in a plane perpendicular to the radiation beam axis defined by specified isodose lines. In broad beams a radiation field size can easily be achieved within 1 % to 2 % of the set field size, but the dosimetry is much less sensitive. In small field sizes this breaks down because of the partial source occlusion of the primary photon source and loss of LCPE (IPEM, 2010). The FWHM is determined by a position on penumbra curve that is lower because of a reduced central axis maximum dose value (IAEA, 2017). The FWHM of the field size measured is

therefore not consistent with the geometrical field size defined by the projected collimator settings (IAEA, 2017). This could lead to substantial errors in obtaining factors such as detector perturbation factors (IAEA, 2017; Derreumaux, 2011).

The IAEA code of practice for dosimetry of small static field in external beam radiotherapy, IAEA 483, was published in 2017. It gives guidance on the dosimetry and gives a formalism for performing measurements for reference dosimetry. It also provides data of the FOCF that are required for performing measurements of field output factor (FOF).

4.2 Characteristics of small field

There are three conditions that characterize a small field. Two of these are related to the beam and the third one to the detector used (Alfonso, 2008). One or more of these must be fulfilled for a field to be classified as a small field. These are (IPEM, 2010):

- Loss of Lateral Charged Particle Equilibrium (LCPE);
- Partial occlusion of the primary photon source by the collimating devices on the beam axis; and
- Volume averaging and perturbation (detector effects).

4.2.1 Lack of lateral charged particle equilibrium

Lack of lateral charged particle equilibrium (LCPE) happens when the beam radius is small in comparison to the maximum range of the secondary electrons (IPEM, 2010). The charged particles from the region outside the beam central axis scattered towards the central region are not enough to compensate for the charged particles leaving the central region (Andreo, 2017). The absorbed dose to be measured is then smaller than the maximum range of the secondary electrons produced through interaction in the irradiated medium (IPEM, 2010 and Andreo, 2017). This is due to the small field size that does not allow for the balance in the charged particles scattered. Only a fraction

of the energy transferred to kinetic energy of charged particles, for a given small volume of interest, will contribute to the energy deposition in the same volume of interest (Andreo, 2017). This impacts on the absorbed dose to water measurements as well as dose calculations in treatment planning, especially in the areas with tissue heterogeneities (ICRU, 2017).

For cavity theory to be applied under CPE in measurements using an ionisation chamber, the collision kerma and the absorbed dose are equal. Li et. al. and Papaconstadopoulos (Li, 1995 and Papaconstadopoulos, 2016), performed calculations to determine the range at which the collision kerma and the absorbed dose stops being equal using Monte Carlo simulation for different energies and various circular fields. Figure 4.1 shows the smallest beam radius for the various photon beam energies where $D_w / K_{col,w} \neq 1$ from data published by Papaconstadopoulos. The ratios were evaluated on the central axis of the beam, at a depth of 5 cm, SSD of 80 cm for Co-60 and SSD of 100 cm for all the other beams. The electron range increases with energy, so the beam radius at which the lack of CPE occurs increases as the beam energy increases. Because of the reduction in the charged particle range, as the photon energy is reduced the minimum radius of the broad beam decreases (Andreo, 2017). The IAEA TRS 483 (IAEA, 2017) expressed the relation between r_{LCPE} and beam quality *TPR 20,*10(10) as:

$$r_{LCPE}[cm] = 8.369 \times TPR_{20,10}(10) - 4.382 \qquad (4.1)$$

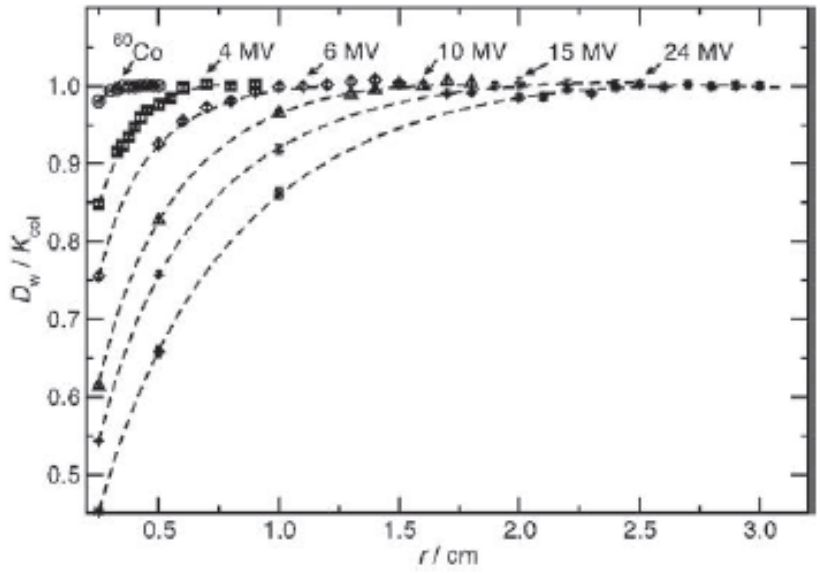


Figure 4.1 The ratios of the dose-to-water, D_w, to water-collision kerma, $K_{col,w}$, versus the radius of the beam for beam energies Co-60, 4 MV, 6 MV, 10 MV, 15 MV and 24 MV. The ratios were evaluated on the central axis of the beam, at a depth of 5 cm, SSD of 80 cm for Co-60 and SSD of 100 cm for all the other beams (Reproduced from the IAEA TRS 483 (IAEA, 2017) with permission from Papaconstadopoulos, McGill University, Canada).

4.2.2 Partial occlusion of the primary photon source

In a linear accelerator, a primary photon beam is created by a pencil electron beam that is accelerated in a waveguide then through bending magnets or accelerator flight tube into the bremsstrahlung target (Andreo, 2017; Podgorsak, 2005). The size of the electron beam hitting the target is determined by how the beam is tuned by the bending magnet and the steering magnetic fields. When an initially small electron beam hits a bremsstrahlung target, its size is slightly increased at the exit plane of the target. It is then further broadened by the flattening filter due to scattering. The collimators in a linear accelerator head are then used to provide desired radiation fields. When the collimator settings are decreased such that they shield part of the finite primary photon source, this effect is called partial source occlusion. Figure 4.2 illustrates this effect. As the field size is decreased, there is a limit in the size of the beam at which the partial

source occlusion results in the penumbra overlapping from opposite sides of the beam (IPEM, 2010), see figure 4.2. This results in the beam output being decreased (Andreo, 2017). The partial occlusion is dependent on the technique used to generate the beam and, on the source to collimator distance for a given source to detector distance (Das, 2008). Partial source occlusion also causes a reduction in the beam output and results in steep dose gradients.

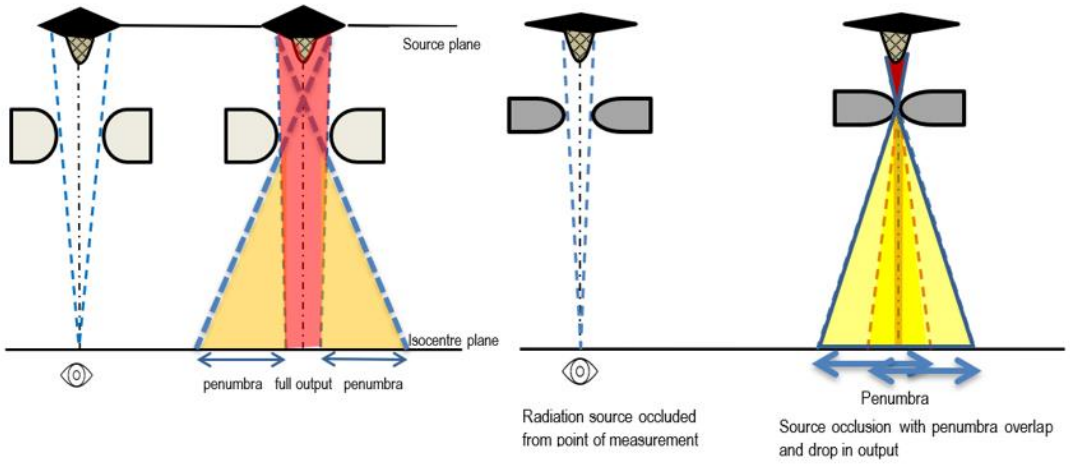


Figure 4.2 Illustration of the partial source occlusion. On the “full view of extended direct beam source”, the source is viewable from the plane of measurement and penumbra is separate. To the right is the “partial view of extended direct beam source”, the source is not viewable from the measurement plane of view and the penumbra is overlapping (IPEM, 2010).

4.2.3 Detector effects

A signal that is measured by a detector is considered to be averaged over its entire finite sensitive volume, and this is referred to as volume averaging (IPEM, 2010). If a detector that is larger than the beam being measured is used, the particle tracks will travel across a small fraction of that detector and the detector signal will be averaged over the whole detector sensitive size (Andreo, 2017). In addition, the presence of the detector itself in the beam causes perturbation of the charged particle fluence leading to a deviation from the Bragg Gray cavity theory conditions. Fluence perturbation becomes large and difficult to model in the presence of large dose gradients and the

absence of lateral charge particle equilibrium (IAEA, 2017). IAEA TRS 483 therefore recommends that for any detector, measurements should be restricted to beams of radii of at least r_{LCPE} plus half the size of the external volume of the detector to significantly decrease the effect of these effects (IAEA, 2017).

4.2.4 Energy spectrum of small fields

The spectrum of a photon beam in small fields is significantly different from that of a broad beam generated by the same source. This is due to changes caused by the collimation in the head of a linear accelerator and the changes in the phantom scatter due to the reduction in the beam size (IPEM, 2010; Andreo, 2017). The collimator in the linear accelerator head occludes the primary photon source when the field size is decreased, and the scattered photons generated in the collimator head do not reach the surface of the phantom. Subsequently, there is a reduction in the number of low energy photons scattered in the linear accelerator head that reach the central axis of the small field. Depending on the shape and material of a flattening filter in a collimator, there might be an increase in the photons scattered in the head, for off axis fields, causing the beam to be soft or hard (IAEA, 2017). The phantom scatter decreases for small fields compared to broad beams. And this reduction has a larger effect on the beam field output factor for most measurement depths than the head scatter.

There is a hardening of the photon energy spectrum at any point on the beam axis as the field size is decreased and an increase in the average photon energy. Because of this, there is a change of the ratio of mass energy absorption coefficients between water and the detector material and a potential change of the stopping-power ratio between water and the detector material. When the field is too small for LCPE to be achieved, this results in a shortage of low energy electrons reaching the central axis, resulting in an increase of the mean electron energy which can also affect the stopping power ratio (IAEA, 2017). Monte Carlo simulations have shown that the charged particle spectrum produced in water is less affected even though the photon fluence spectrum changes considerably as a function of field size (IAEA, 2017). As a result

the influence of field size on the water to air stopping-power ratio is found to decrease by not more than 0.6 % at a depth of 10 cm in a 6 MV photon beam over a range of field sizes from 10 x 10 cm^2 reference fields to 0.3 x 0.3 cm^2 (Sanchez-Doblado, 2003; Eklund, 2008). The variation is not larger than 1 % over a range of depths from the depth of dose maximum to 30 cm (Eklund, 2008).

4.3 Traceability for small photon fields

There are no primary standards that have been fully characterised and internationally compared for use in small static fields in radiotherapy. There has been work done by the PSDL's in characterising their standards and determining the beam quality correction factors for specific ionisation chambers (Krauss, 2011). The work has mainly been on water and graphite calorimeters. Each type has its advantages and challenges, further discussed below.

Existing calorimetry standards were mainly established for use in conventional reference beam qualities. There are primary standard laboratories that have performed studies using calorimeters for small field dosimetry. These include the national metrology Institutes for Germany (PTB), Nertherland (VSL), United Kingdom (UK) (IAEA, 2017). Renaud et.al. (2018), are working on a graphite calorimeter for dosimetry in small fields. This has been patented and will allow for use of the calorimeter at the clinic as the handling and measurement set up is less sophisticated than those used by the PSDL's. NPL UK has done some work on a graphite calorimeter for use in IMRT (Duane, 2012).

4.3.1 Water calorimeter

When a water calorimeter is used for measurements in small static fields, some limitations have been observed and these include the large heat loss correction factors linked to the temperature gradients and the heat loss corrections that are dependent on the irradiation time and subsequently the dose rate (Kraus, 2007; Kraus 2011).

High dose rates or short radiation time, which can be achieved in flattening filter free (FFF) photon beams, may assist to reduce the heat loss correction (Seuntjens, 2016) and allow for the use of water calorimetry for the determination of absorbed dose to water even in small fields.

4.3.2 Graphite calorimeter

Graphite calorimeters could possibly be the best option for reference dosimetry for small static fields. This relates to the design of the calorimeter because the volume over which the average dose is measured is thermally isolated from the environment. If the core is made smaller it does not necessarily affect the temperature rise that is measured. The temperature rise does not decrease as the calorimeter size is decreased (Andreo, 2017; Renaud, 2018). Côté et. al. has successfully designed and built a probe-format graphite calorimeter, aerrow-mini, that may be used routinely in clinical small fields. The simulation results as presented at the IAEA IDOS symposium showed great potential and future work was still to validate the simulated data and characterise the detector in small fields (Côté, 2019).

4.3.3 Detectors used for small field dosimetry

The choice of detector for performing measurements needed for the small field dosimetry is critical. In 2007 it was reported that a Farmer type chamber was used to collect commissioning data (ASN, 2007), which resulted in a radiation incident. For air filled ionisation chambers, the variation of the stopping power ratio with field size has shown to be negligible however the perturbation correction factors vary significantly with those of the broad beams such that the Bragg-Gray theory breaks down (Andreo, 2017). Using perturbation correction factors determined for broad fields in small fields may underestimate the conversion from cavity signal to absorbed dose to water. There are detectors that perform better than air filled ionisation chambers in small fields in terms of perturbation effects and energy dependency. These detectors also have a sensitive area that is water equivalent; the density of the sensitive region is the same as that of water and the radiation sensitive volume is small compared to the radiation

field. Solid-state detectors can be small without losing the capability of measuring the signal. Their main disadvantage is the energy and dose rate dependency (Andreo, 2017). Diamond detectors have a notable dose rate dependency because of recombination. In beams where there is a large contribution of low energy photons, as in broad photon beams, silicon diodes over-respond because of the interaction of the photons with silicon which has a higher energy-absorption coefficient than water.

Diamond detectors are dose rate dependent due to recombination even though their energy dependence is near water equivalent (Andreo, 2017). Liquid ionisation chambers are small and water equivalent however they require recombination and temperature corrections. All detectors that are currently available in the market present some advantages and disadvantages for use in small field dosimetry. This makes it crucial to quantify the measurement uncertainties to ascertain which detector gives the best uncertainties to meet the accuracies required for the desired treatment outcome.

4.4 Dosimetry formalism in small fields

4.4.1 Reference dosimetry

With the developments in technology, not all machines are able to achieve a 10 x 10 cm^2 field size. Alfonso et al (2008), introduced a concept of a machine specific reference (msr) field, which was adopted with slight modifications in IAEA TRS 483 (IAEA, 2017). The msr field is usually defined as the largest field size that the machine is able to achieve and smaller than 10 x 10 cm^2. It must extend beyond the outer boundaries of a detector used by a distance r_{LCPE}, where r_{LCPE} is the radius of the lateral charged particle equilibrium (IAEA, 2017). The r_{LCPE} establishes the relation between the field size and the detector size for which the lateral charged particle equilibrium exists.

Based on the absorbed dose to water formalism explained in section 3.4 and incorporating the Alfonso formalism, the absorbed dose to water for the msr field will then be given by the following formula (Alfonso, 2008; IAEA, 2017):

$$D_{w,Q_{msr}}^{f_{msr}} = M_{Q_{msr}}^{f_{msr}} N_{D,w,Q_o}^{f_{ref}} k_{Q_{msr}Q_o}^{f_{msr},f_{ref}} \quad (4.2)$$

where:

$M_{Q_{msr}}^{f_{msr}}$ is the electrometer reading in the msr field corrected for all relevant influence quantities (temperature, pressure, humidity, polarity, ion collection efficiency, etc);

$N_{D,w,Q_o}^{f_{ref}}$ is the absorbed dose to water calibration coefficient, for the detector, provided by the calibration laboratory at their conventional 10 x 10 cm^2 reference field, f_{ref}, with beam quality Q_o; and

$k_{Q_{msr}Q_o}^{f_{msr},f_{ref}}$ is a correction factor for the variance in the response of the detector in a conventional beam, $f_{ref,}$ with beam quality Q_o with that in the msr field with beam quality Q_o.

However, equation 4.2 may be used when the factor $k_{Q_{msr}Q_o}^{f_{msr},f_{ref}}$ is available for the detectors being used and some are published in guidance documents like the IAEA TRS 483 (IAEA, 2017). This factor is defined as

$$k_{Q_{msr},Q_o}^{f_{msr},f_{ref}} = \frac{N_{D,w,Q_{msr}}^{f_{msr}}}{N_{D,w,Q_o}^{f_{ref}}} = \frac{D_{w,Q_{msr}}^{f_{msr}} \Big/ M_{Q_{msr}}^{f_{msr}}}{D_{w,Q_o}^{f_{ref}} \Big/ M_{Q_o}^{f_{ref}}} \quad (4.3)$$

where:

$N_{D,w,Q_{msr}}^{f_{msr}}$ is the absorbed dose to water calibration coefficient, for the detector, provided by the calibration laboratory for the msr field, f_{msr}, of beam quality Q_{msr};

$N_{D,w,Q_o}^{f_{ref}}$ is the absorbed dose to water calibration coefficient, for the detector, provided by the calibration laboratory at their conventional 10 x 10 cm^2 reference field, f_{ref}, with beam quality Q_o;

$D_{w,Q_{msr}}^{f_{msr}}$ is the absorbed dose to water for the msr field;

$M_{Q_{msr}}^{f_{msr}}$ is the electrometer reading in the msr field corrected for all relevant influence quantities (temperature, pressure, humidity, polarity, ion collection efficiency, etc.);

$D_{w,Q_o}^{f_{ref}}$ is the absorbed dose to water for the reference field, f_{ref}, with beam quality Q_o;

$M_{Q_o}^{f_{ref}}$ is the electrometer reading in the reference field corrected for all relevant influence quantities (temperature, pressure, humidity, polarity, ion collection efficiency, etc.).

The beam quality correction factors have been determined by some PSDL's using calorimeters and Monte Carlo simulations for some of the ionisation chambers. Most of the data currently published in guidance documents and other sources relies on the Co-60 being the reference beam quality. Should the laboratory be using a reference beam that is different to a clinical beam to perform calibrations, and guidance documents have Co-60 k_{Q,Q_o} factors, the required factor can be determined as (IAEA, 2017; Andreo, 2017):

$$k_{Q,Q_o} = k_{\text{ref,clin}} = \frac{N_{D,w,\text{ref}}}{N_{D,w,\text{clin}}} = \frac{N_{D,w,\text{ref}}}{N_{D,w,^{60}\text{Co}}} \frac{N_{D,w,^{60}\text{Co}}}{N_{D,w,\text{clin}}} = k_{\text{ref},^{60}\text{Co}} k_{^{60}\text{Co},\text{clin}} = \frac{k_{\text{ref},^{60}\text{Co}}}{k_{\text{clin},^{60}\text{Co}}} \quad (4.4)$$

The beam quality correction introduces uncertainties associated with its determination. To be able to use generic beam correction factors the beam quality must be determined. Depending on which guidance document is being used, the beam quality may be specified as tissue phantom ratio, $TPR_{20,10}$ (IAEA, 2000) or the percentage depth dose, $PDD(10)$ (Almond, 1999).

4.4.2 Field output factor

The definition given in 3.4.4 of the output factors (OF) applies also in small fields except that for small fields the ratio of detector readings may not be used because of the dependency of the dosimetric quantities such as the perturbation factors with the field size (IAEA, 2017). FOCFs need to be applied to the calculated ratio of the charge measurements, which would have been corrected for all influence quantities. This is then referred to as the field output factor (FOF). In summary, the FOF for small fields is the ratio of the dose measured under non reference conditions to the dose measured under reference conditions (IAEA, 2017).

4.4.3 Field size

There is no exclusive definition for field size in small fields. The IAEA TRS 483 (IAEA, 2017) defines the equivalent square field (S_{clin}) as shown in equation 4.5 for square or rectangular fields:

$$S_{\text{clin}} = \sqrt{AB} \qquad 4.5$$

where A and B are the in plane and cross plane dosimetric field widths determined during the FWHM measurements. For circular fields

$$S_{\text{clin}} = r\sqrt{\pi} = 1.77r \qquad 4.6$$

where *r* is the FWHM radius. Equations 4.5 and 4.6 were used in this study for calculating the equivalent square field for small fields.

4.4.4 Beam quality Indices

The water to air stopping power ratio has very small variations with field size. Because of this, it is suggested that the beam quality index, as detailed in section 3.4.5 for broad beams, may be used for small field sizes (Andreo, 2017). The variation with field size seen in the stopping power ratios and the perturbation factors is included in the FOCF, which is also dependant on field size (IAEA, 2017). The definition given in section 3.4.5 for $TPR_{20,10}(10)$ is for square fields. For machines that cannot achieve 10 x 10 cm^2 reference fields, the following equation is recommended to be used to determine the virtual beam quality index $TPR_{20,10}(10)$, as used in broad beam dosimetry (IAEA, 2017):

$$TPR_{\ 20,10}(10) = \frac{TPR_{\ 20,10}(S)+c(10-S)}{1+c(10-S)} \qquad (4.7)$$

where *S* is the equivalent square field size in cm for the machine specific reference field closest to 10 x 10 cm^2. $TPR_{20,10}(S)$ is the ratio of absorbed dose to water at the depths of 20 g/cm^2 and 10 g/cm^2 in water for an equivalent square field size of $S \times S$ cm^2 defined at a source to detector distance (SDD) of 100 cm, $c = (16.15 \pm 0.12) \times 10^{-3}$. The approach is considered valid for 4 cm ≤ *S* ≤ 12 cm. This range for the

model equation 4.7 is justified by Palmans's observation that the dependency of $TPR_{20,10}(S)$ on S is approximated to be linear for 4 cm ≤ S ≤ 12 cm (Palmans, 2012). The model used to estimate the constants has not been tested for field sizes less than 4 x 4 cm^2 as this study used standardized data that ranged from 4 x 4 cm^2 to 40 x 40 cm^2 (BJR-25, 1996). The beam quality indices are still used to link the calibration beam quality or the machine specific reference beam to a clinical beam (IAEA, 2017).

5. Introduction to measurement uncertainty

Estimating measurement uncertainties for measurement capabilities is something that is standard practise for primary and secondary standard laboratories who have a quality management system following the international standard on general requirements for the competence of testing and calibration laboratories, ISO/IEC 17025:2017 (ISO, 2017). Estimation and publishing of uncertainties is not a common practice amongst physicists in hospitals. This is also evident in the data published for static small fields by several authors that lack estimation of uncertainties for several steps in the determination of correction factors (IAEA, 2017). This is also observed in some conference presentations.

There is guidance on the estimation of uncertainties for measurements performed in hospitals by physicists (IAEA, 2016; van der Merwe, 2017). The ICRU 83 report (ICRU 2010) recommends that for reporting purposes, as part of clinical trials, publications, etc., the uncertainties associated with the relevant quantities and parameters should be estimated and presented. There is still some confusion as to what uncertainty of measurement is and how to estimate it and the misunderstanding of the differences between measurement uncertainty, measurement error and measurement accuracy. Even though there is now an international code of practice for small field dosimetry (IAEA, 2017), there is still a need of quantifying the accuracies related to the implementation of the code for each portion of measurements leading to the treatment delivery.

This section aims at explaining the terminology that is used with reference to estimation of uncertainties and measurement accuracies. This is the terminology adopted in the metrology environment and defined in various international standards like VIM (BIPM JCGM, 2008), GUM (BIPM JCGM, 2012). The work of this study aims to show how to quantify the accuracy of measurements performed for small static fields at the hospitals and thus determining the associated measurement uncertainties. Understanding the terminology and the quantification of uncertainties will assist with consistency in the data published and used by the end users.

There have been different approaches in dealing with measurement uncertainties. Previously, it was based on an error approach also known as true value approach (BIPM JCGM, 2008). This approach determines an estimate of the true value that is as close as possible to a single true value. The deviation from that true value is set to be from two kinds of errors, random and systematic. An assumption is made that these errors are distinguishable and must be treated differently. There is no rule on how these are combined to determine the total error. An upper limit of the absolute value of the total error could be estimated and loosely named uncertainty (BIPM JCGM, 2008). In the uncertainty approach, the aim of the measurements is to determine that interval of reasonable values to what is measured, assuming no mistakes were made whilst performing measurements. There are factors that may affect the measurements. Evaluating these may decrease the interval but never reduce it to a single value. Each factor influencing a measurement result contributes to the magnitude of the interval. In instances where there are no factors affecting the measurements, the scale of the measuring instrument will limit the resolution of the measured value (BIPM JCGM, 2008).

5.1 Terminology

5.1.1 Measurement accuracy and measurement precision

Measurement accuracy is defined as the closeness of what is being measured with its true value or a standard. According to VIM the concept of measurement accuracy is not a quantity and is not given a numerical quantity value. It should not be used interchangeably with measurement precision as they mean different things. Measurement precision is the closeness of agreement between various measurements of the same quantity (BIPM JCGM, 2008; 2012). The intention is for the measurements to be of high precision and high accuracy and never be of low accuracy and low precision nor low accuracy and high precision. Depending on the uncertainty of measurements to be achieved, high accuracy and low precision measurements could be acceptable. Low accuracy and low precision measurements

have a high probability of not representing the true value. Whereas the low accuracy and high precision could precisely miss the true value. Low accuracy and high precision show a pronounced systematic error. Whereas the low accuracy and low precision show a more pronounced random error. Figure 5.1 adapted from references Streiner, 2006 and Ratcliffe, 2015 shows this graphically. For treatment deliveries in radiotherapy especially using the small fields the intent is to deliver the dose to the tumour with high precision and high accuracy and sparing the normal tissues. Without the knowledge of the measurement uncertainty in the dose delivery limits the knowledge of the risks associated with that treatment delivery.

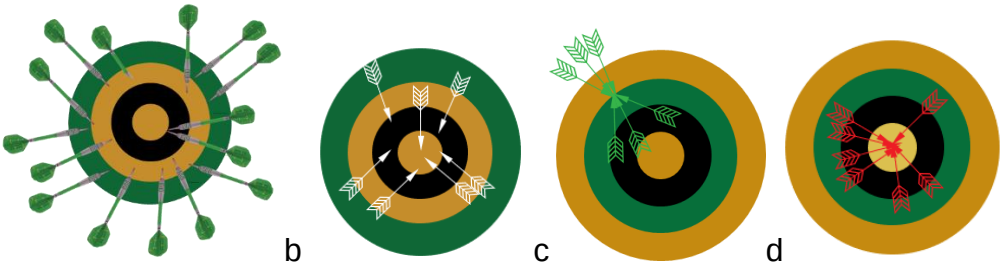


Figure 5.1 Representation of (a) low accuracy and low precision, (b) high accuracy and low precision, (c) low accuracy and high precision, and (d) high precision and high accuracy (Streiner, 2006).

5.1.2 Measurement repeatability

Measurement repeatability is the ability to perform measurements precisely for various measurement sets following the same measurement procedure, using the same measuring system, same operator and under the same conditions. The standard deviation of the mean for a set of data will give an indication of the repeatability of the measurements indicating how each measurement varies from the mean value. It is given by:

$$u_{R=} \frac{s}{\bar{x}\sqrt{n}} \times 100 \qquad 5.1$$

where *s* is the standard deviation of the measurement readings, $\bar{x}$ is the average of the measurement readings and *n* is the number of measurement readings. It may also be referred to as the standard uncertainty.

5.1.3 Measurement reproducibility

Measurement reproducibility is the ability to precisely reproduce a measurement using different operators, different measurement systems and may even be at different locations.

5.1.4 Measurement error

Measurement error is the difference of the measured quantity from its reference value (BIPM JCGM, 2008). For this work, measurement error should not be confused with a mistake. Measurement error may be systematic or random. Random measurement error varies unpredictable whereas the systematic error varies in a predictable manner. Systematic error may be known or unknown and is correctable when known.

5.1.5 Measurement uncertainty

Each measurement performed provides information about the quantity being measured, the measurand. There is no measurement that will be exact. There is always a dispersion of the values being measured even when the conditions are the same for each measurement set up. What characterises the spread of the values that is allotted to what is being measured, based on the information used, and is non-negative is known as the associated measurement uncertainty (BIPM JCGM, 2008; 2012). The estimation of measurement uncertainties involves establishing an itemised description of contributors to the uncertainty, uncertainty budget, and evaluating type A and type B uncertainties. It is usually presented in a table format. Type A standard uncertainties are those evaluated by statistical means of a measured quantity for defined conditions. Type B standard uncertainties are those defined by means other than statistical evaluation of a series of observation. When the measurement uncertainty is stated as a standard deviation it is referred to as a

standard measurement uncertainty (BIPM JCGM, 2008; 2012). The measurement uncertainty helps define the accuracy of measurements.

The basis of an uncertainty budget is the measurement model, also referred to as a functional relationship, used for the calculation of the measurand (BIPM JCGM, 2009). Each input quantity, which is usually known, in the measurement model contributes to the measurement uncertainty together with the associated correction factors, covariances, applied probability distribution, and degrees of freedom (BIPM JCGM, 2008; 2012). The output quantity is what is of interest. The covariance, also referred to as a correlation, is determined for input quantities that could be related. It gives a measure of strength of the relationship of those input quantities. If the input quantities are independent of each other than the covariance is zero. For each input quantity in the model equation a sensitivity coefficient, which show how the input quantities are related to the measurand, needs to be calculated.

The probability distribution functions are used to model the information about what is being measured. It gives an indication of the possible values that the measurand might be. When evaluating Type A uncertainty contributors, it is usually assumed that the probability distribution best describing the input quantity is a *Gaussian* distribution, shown in figure 5.2, for a given number of readings repeated under the same conditions, independently (ISO, 2006; BIPM JCGM, 2009). This is applicable when one has substantial data. When the data being evaluated is small, the probability distribution can be a *t-distribution* (ISO, 2006; BIPM JCGM, 2009), as shown in figure 5.2. For Type B uncertainty contributors, it is usually known that the value lies within an interval. The commonly used probability distributions are a rectangular or triangular distribution (see figure 5.3). The width of the probability distribution function gives us an indication of the accuracy of what is measured.

Uncertainties of measurements may be reported as expanded measurement uncertainties, U. The expanded uncertainty is a product of the combined standard uncertainties, u_i, with the coverage factor, k. The coverage factor depends on the confidence level to the estimation, which also depends upon the type of probability

distribution of the output quantity in a measurement model and on selected coverage probability (BIPM JCGM, 2012). It is obtained from a table of student's *t* factors using the effective degrees of freedom for all the uncertainty components published in GUM (BIPM JCGM, 2012). For this work *k* = 2 equal to confidence level of 95 % was used. The effective degree of freedom is given by the equation (5.2):

$$V_{eff} = \frac{u_c^4}{\sum_i^n \frac{u_i^4}{v_i}} \qquad 5.2$$

where u_c is the combined standard uncertainty, u_i is the i^{th} uncertainty component, v_i is the degrees of freedom of the i^{th} component and n is the total number of components.

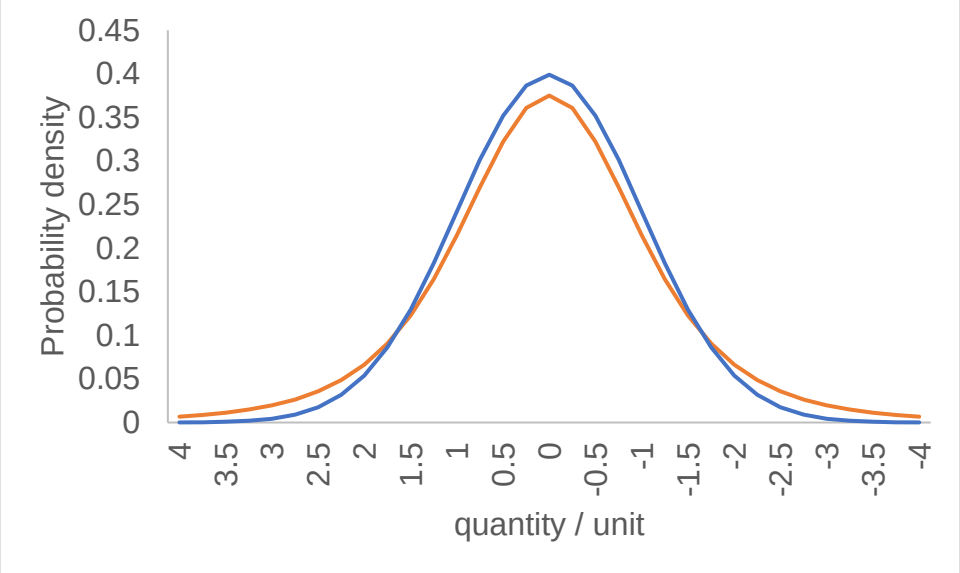


Figure 5.2 A Gaussian distribution (continuous black curve) and a t-distribution with four degrees of freedom (broken red curve) ('unit' denotes any unit) (BIPM JCGM, 2009).

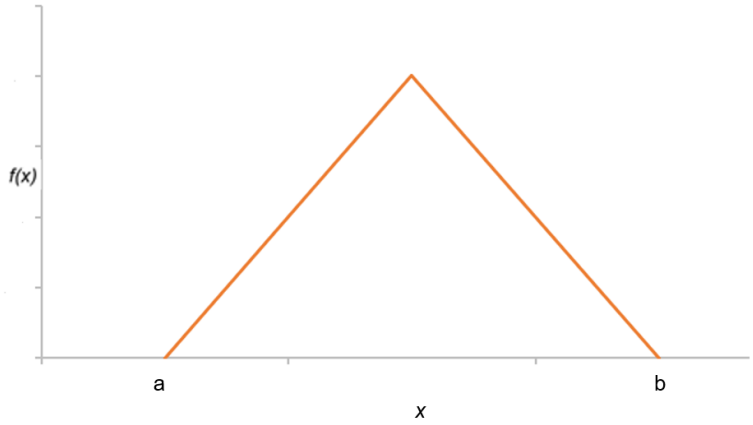


Figure 5.3 A triangular distribution with limits a and b (BIPM JCGM, 2009).

In this work the estimation of uncertainties is going to be done following the GUM framework (BIPM JCGM 2009). In short, this entails:

a) Defining the output quantity, the measurand.
b) Identifying and estimating the input quantities on which the measurand depends.
c) Developing a measurement model linking the measurand and the input quantities.
d) Allotting a probability distribution to the input quantities, a_i.
e) Estimating the standard uncertainty for each input quantity, u_i.
f) Determining the sensitivity coefficient, c_i which is obtained by performing a partial derivative of the model equation.
g) Determining the overall uncertainty, $U = \sqrt{\sum_i (a_i u_i c_i)^2}$.

6. Experimental: Materials and Methods

The study was performed at the Charlotte Maxeke Johannesburg Academic Hospital (CMJAH), Radiation Oncology department. The waiver of ethics clearance was issued by the University of the Witwatersrand, Human Research Ethics Committee (Medical).

6.1 Materials

6.1.1 Irradiators and data collecting system

Figure 6.1 a and b shows the irradiators that were used. The Siemens Primus (S/N 4193) had 82 leaves of 1 cm projection width at the isocentric plane, in the X axis (cross plane) direction, and a conventional asymmetric collimator in the Y axis (in plane) direction. The central leaf pair was centred on the cross plane major axis. Small photon fields were produced using the MLC and jaw, and also using tertiary demountable set of stereotactic circular cones. The cones manufactured by Brainlab had radii of 30 mm, 25 mm, 20 mm, 17.5 mm, 15 mm, 12.5 mm, 10 mm and 7.5 mm. Figure 6.2 shows the unit with a stereotactic cone attached. The field size of the machine was fixed at 5 x 5 cm^2 when the cones were used. The 6 MV photon energy beam was used. The smallest field size that could be achieved on the linac was 0.6 x 0.5 cm^2.

The Equinox Co-60 unit (S/N 2009) had a source size of 1.5 cm in diameter and the source was 80 cm from the isocentre. It had dual asymmetric collimators. The smallest symmetric field size that could be achieved was 1 x 1 cm^2.

(a) 

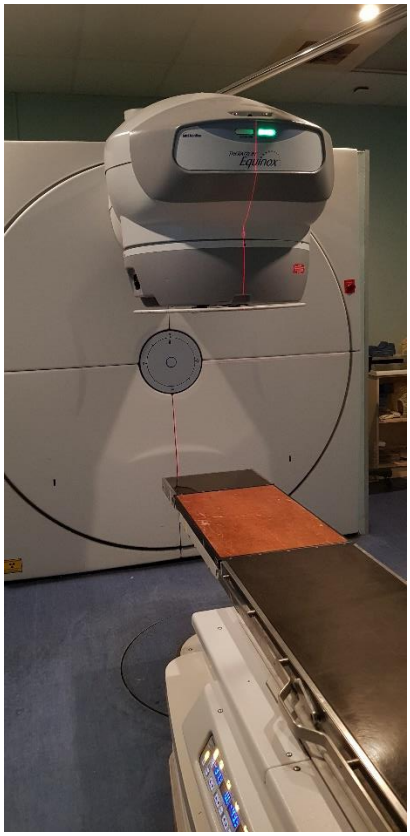
(b) 

Figure 6.1 Treatment units from CMJAH that were used for the study (a) Siemens Primus linear accelerator and (b) Equinox 80 Co-60 unit.



Figure 6.2 The Siemens Primus linac head at CMJAH with a demountable tertiary collimator attached.

A motorised PTW MP3 water phantom, as shown in Figure 6.3, with a scanning range of 60 x 50 x 40.8 cm^3 was used for data acquisition. It is a 3D beam acquisition system consisting of a 3D stainless steel moving mechanism driven by three high speed stepper motors. According to the manufacturer's specifications, it had a precision stepper motor which allows for movement of the detector with a speed of 50 mm/s and a positioning accuracy of 0.1 mm.



Figure 6.3 The motorised PTW MP3 water tank that was used for the measurements at CMJAH.

6.1.2 Detectors and electrometers

The following detectors were used in this study: PTW types 60012 and 60019, which were solid-state detectors and PTW types 30018, 31016, 31010, 31021, 30013, 31006 and 34091, which were ionisation chambers (see figure 6.4). Specifications provided by the manufacturer were used for all, as detailed in the PTW detector brochures. The details of the detectors are given in tables 6.1 and 6.2.

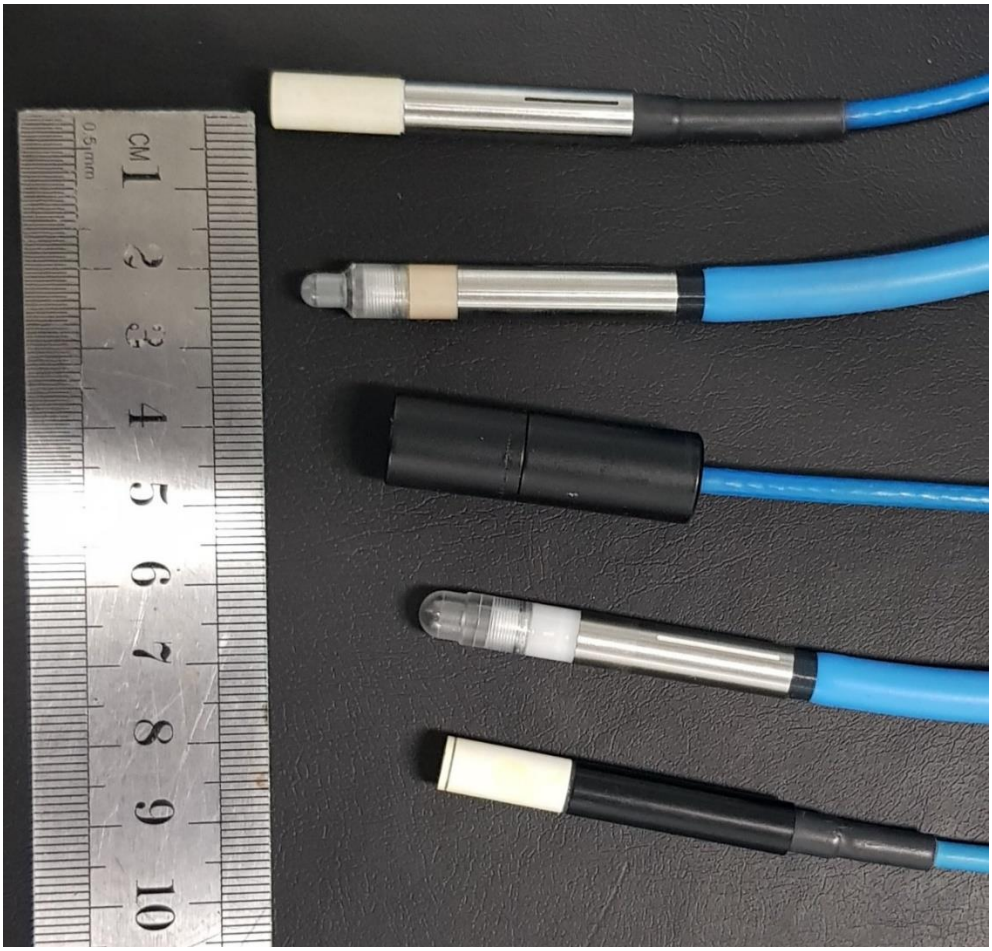


Figure 6.4 Picture showing small field detectors used in the study. From top to bottom they are PTW 60012, PTW 31016, PTW 31018, PTW 31021 and PTW 60019.

The PTW 60012 and PTW 60019 detectors were oriented parallel to the beam. The PTW 31016, PTW 31018 and the PTW 31021 detectors could be positioned parallel or perpendicular to the beam. The PTW 31010 and PTW 30013 ionisation chambers were positioned perpendicular to the beam. A PTW tandem with an external voltage was used for the measurements and a PTW Unidos E used for some of the reference dosimetry measurements.

Table 6.1 Specifications of the solid-state detectors used during the study provided by the manufacturer.

Solid-state detector description	**Dimensions of a detectors**	**Orientation relative to the beam**	**Nominal sensitive volume**	**Dimensions of sensitive volume**	**Reference point**	**Applied voltage (V)**	**Minimum field size recommended for use**
PTW 60012 unshielded diode E with a p-type silicone diode	diameter was 7 mm, length 45.5 mm	Axial	0.0025 mm^3	radius 0.56 mm and a depth of 2.5 µm	0.6 mm from the detector tip	zero	1 x 1 cm^2
PTW 60019 microDiamond	diameter was 7 mm, length 45.5 mm	Axial	0.004 mm^3	radius of 1.1 mm and thickness of 1 µm	1 mm from the detector tip	zero	1 x 1 cm^2

Table 6.2 Specifications of the ionisation chambers used during the study provided by the manufacturer.

Ionisation chamber description	**Inner electrode**	**Orientation relative to the beam**	**Nominal sensitive volume**	**Dimensions of sensitive volume**	**Reference point**	**Applied voltage (V)**	**Minimum field size recommended for use**
PTW 31018 liquid filled microLion	Graphite	Axial	1.7 mm^3	radius of 1.25 mm and depth of 0.35 mm	0.975 mm from the entrance window, on chamber axis	800	1 x 1 cm^2
PTW 31016 PinPoint 3D ionisation chamber	Al of purity 99.98 %, with diameter of 0.3 mm	Radial	0.016 cm^3	radius of 1.45 mm and length of 2.9 mm	2.4 mm from chamber tip, on chamber axis	400	2 x 2 cm^2
PTW 31006 Pinpoint Ionization Chamber	Al of purity 99.98 %,	Axial	0.015 cm^3	radius of 1 mm and length of 1.45 mm	3.4 mm from tip, on chamber axis	400	2 x 2 cm^2
PTW 31010 vented cylindrical and semiflexible	Al of purity 99.98 %, with diameter of 1.1 mm	Radial	0.125 cm^3	radius of 2.75 mm and a length of 6.5 mm	4.5 mm from the chamber tip, on chamber axis	400	2 x 2 cm^2

Ionisation chamber description	**Inner electrode**	**Orientation relative to the beam**	**Nominal sensitive volume**	**Dimensions of sensitive volume**	**Reference point**	**Applied voltage (V)**	**Minimum field size recommended for use**
PTW 31021 cylindrical, semiflex 3D thimble	Al of purity 99.98 %, with diameter of 0.8 mm	Axial and Radial	0.07 cm^3	radius of 2.4 mm and a length of 4.8 mm	3.45 mm from the chamber tip, on chamber axis	400	2.5 x 2.5 cm^2
PTW 30013 Farmer type, waterproof	Al of purity 99.98 %, with diameter of 1.1 mm	Radial	0.6 cm^3	radius of 3.05 mm and a length of 23.0 mm	13 mm from chamber tip, on chamber axis	400	5 x 5 cm^2
Ionisation chamber description	**Total area density**	**Orientation relative to the beam**	**Nominal sensitive volume**	**Dimensions of sensitive volume**	**Reference point**	**Applied voltage (V)**	**Maximum field size recommended for use**
PTW T-Ref chamber type 34091, vented plane parallel and waterproof	206 mg/cm^2	Perpendicular to the entrance window	10.53 cm^3	radius of 40.8 mm and a depth of 2 mm	Inside the entrance window, at the centre	400	5 x 5 cm^2 at 20 cm distance to water surface

6.2 Methodology

For small static fields, accurate lateral beam profile measurements are critical for the determination of the actual radiation field size, which is defined as the Full Width Half Maximum (FWHM) of the lateral beam profile. PTW Mephysto mc^2 version 7.42 software was used to perform beam profile scans and the field sizes were calculated as the FWHM. The profile was measured at a depth of 10 cm in water and a SAD of 100 cm.

Major axes dose profiles were measured at depth 10 cm at the source to axis distance (SAD) of 100 cm for the linac for set field sizes of 10 x 10 cm^2, 6 x 6 cm^2, 4 x 4 cm^2, 3 x 3 cm^2, 2 x 2 cm^2, 1 x 1 cm^2 and 0.6 x 0.6 cm^2. The same set of field sizes were used for the Co-60 measurements (except the smallest field size achievable was 1 x 1 cm^2) and measurements were taken at depth 10 cm at the SAD of 80 cm.

6.2.1 Alignment of the water phantom with the gantry and positioning of a detector

The settings of the gantry head and the collimator were verified using a spirit level. The water tank was then visually aligned with the gantry and the alignment of the scanning arm was confirmed using a spirit level when the tank was filled with water.

Each detector was initially positioned on the beam central axis using the co-ordinates of the water tank for the cross plane (X) and in plane (Y) settings and aligning it with the field using the projection of the machine cross hair. This was verified along the axes as well using the light projection of the cross hair (see figure 6.5). For determining the zero depth position on the central axis for detectors that were used in the parallel orientation relative to the beam, the detector was fully immersed in water and brought to the surface until it just broke the surface of the water. That was considered as its initial null point and then, using the engineering diagrams provided by the

manufacturer, the position of its effective point of measurement at the null point followed. This is shown in figure 6.6.

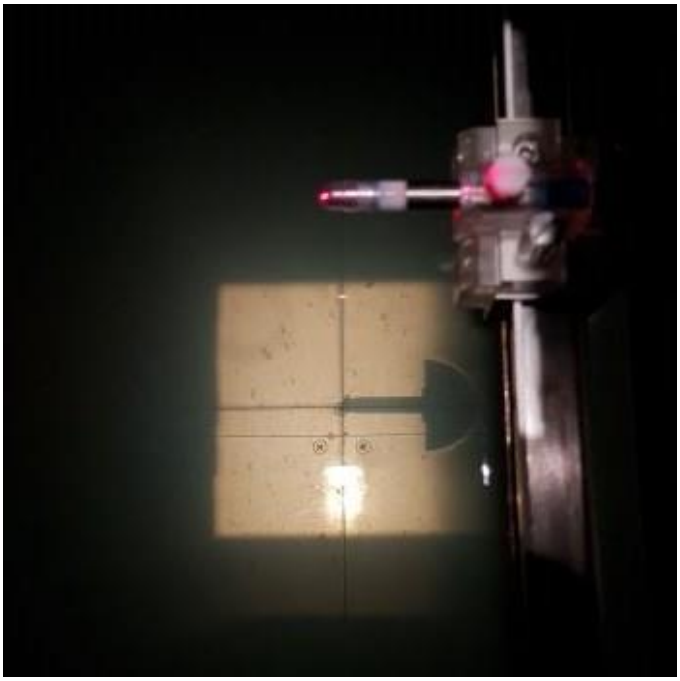


Figure 6.5 Positioning of a detector using the machine cross hair when the detector is oriented perpendicular to the beam. The tip of the detector was positioned such that it just touches the projection of the cross hair. Then the detector travel along the axes was checked using the projected machine cross hair as the detector travelled along each axis.

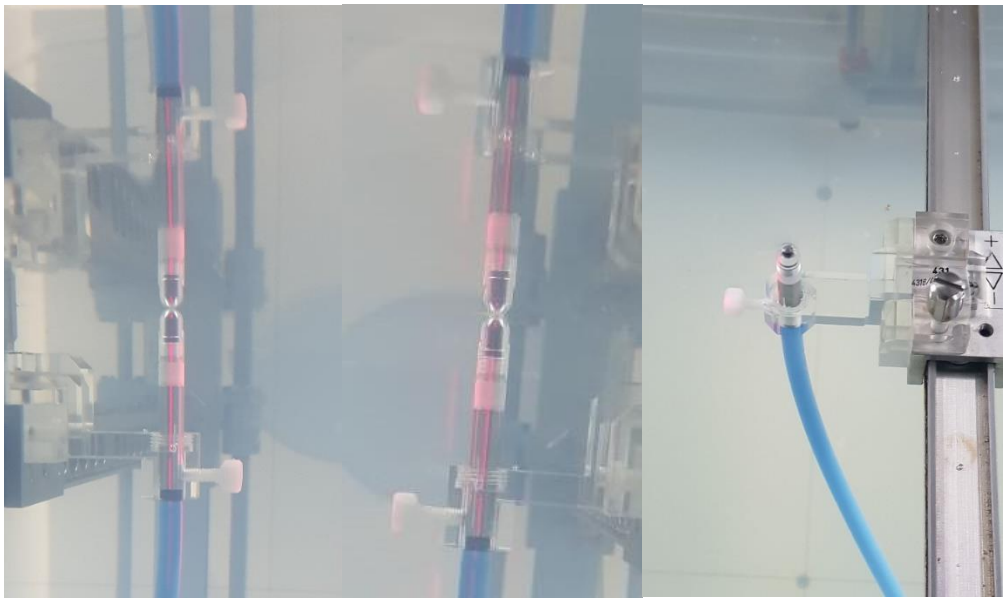


Figure 6.6 Pictures showing the sequential positioning of the reference point of a detector on the central axis of the beam when the detector is oriented parallel to the field. Picture on left showing the tip of the detector positioned few mm from the water surface, centre picture showing the detector on the water surface and the picture on the right showing the reference point of the detector on the central axis of the beam. The dimensions specified by the manufacturer were used for the setting up.

When the detector was oriented perpendicular to the beam, the detector was fully immersed in water and then brought up to the surface using the reflection of the detector. This is shown in figure 6.7. Then the engineering diagrams provided by the manufacturer were used to position the detector at its effective point of measurement.

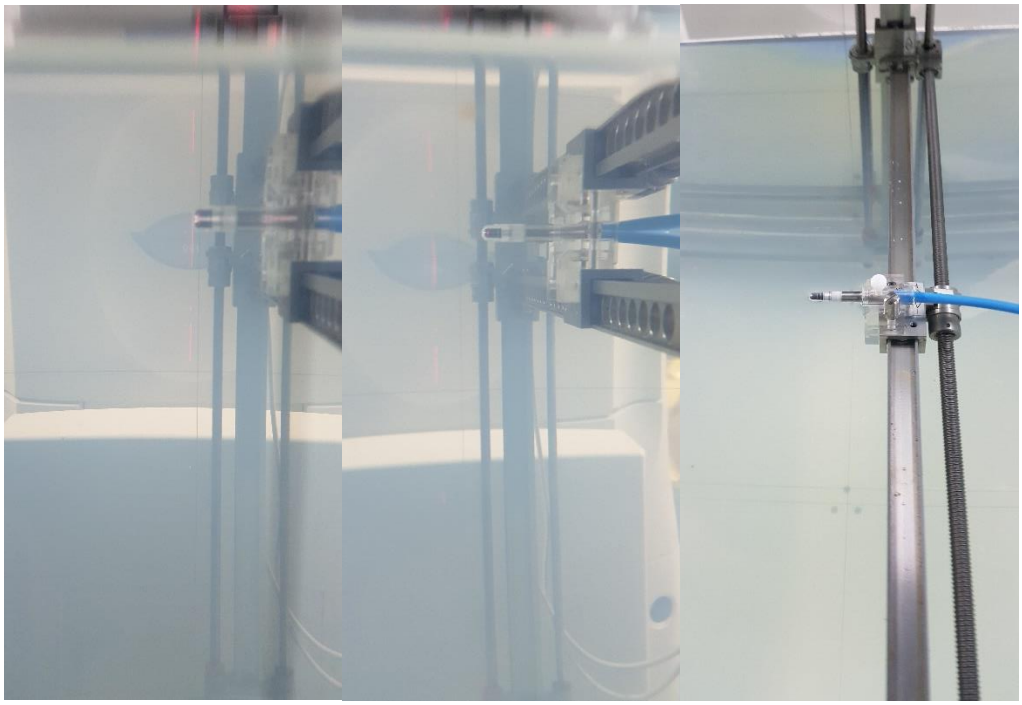


Figure 6.7 Pictures showing the sequential positioning of the reference point of a detector on the central axis of the beam when detector is oriented perpendicular to the field. Picture on left showing the central axis of the detector positioned few mm from the water surface, centre picture showing the central axis of the detector on the water surface and the picture on the right showing the reference point of the detector on the central axis of the beam. The dimensions specified by the manufacturer were used for the set up.

Unless specified, the gantry and collimator settings were at 0° and the depth of measurement was 10 cm. The zero gantry setting was confirmed by measuring cross plane beam profiles at depths 5 cm, 10 cm and 20 cm for a set field size of 3 x 3 cm^2. This was verified for each independent set up of the water phantom. The positioning of the detector was corrected until the Central Axis (CAX) determined was less than the resolution of the stepper motor, which was 0.1 mm.

6.2.2 Determination of the equivalent square field size

In the clinics, the equivalent square notion is used as it is not always possible to know when commissioning a machine all the possible shapes of fields that will be treated. Using the empirical Sterling formula, which is used mainly for rectangular fields, the equivalent square (ESQ) in broad beams is calculated as (Mayles, 2017):

$$ESQ = \frac{4Area}{Perimeter} = \frac{2WL}{(W+L)} \qquad 6.1$$

where *W* is the width and *L* is the length of the field. Cranmer-Sargison (Cranmer-Sargison, 2013) described a method for calculating the effective field size which was adopted by the IAEA TRS 483 working group (IAEA, 2017) as a way of calculating the equivalent square field for small fields. To differentiate between the two methods ESQ will be used for the Sterling equivalent square field and S_{clin} will be used for the IAEA TRS 483 equivalent square field. S_{clin}, is determined as

$$S_{\mathrm{clin}} = \sqrt{AB} \qquad 6.2$$

where *A* and *B* are the in plane and cross plane dosimetric field widths determined during the FWHM measurements. This is only applicable for fields that are square or rectangular with uneven in-plane and cross-plane FWHM on condition that $0.7 < A/B < 1.4$ (IAEA, 2017). Except for the equivalent square field sizes lower than 0.6 cm, this ratio requirement was usually met. Equation 6.1 works on the premise of equal scatter conditions which presents challenges for small fields as there is no scatter and equation 6.2 on the equal area (Cranmer-Sargison, 2013). For circular fields

$$S_{\mathrm{clin}} = r\sqrt{\pi} = 1.77r \qquad 6.3$$

where *r* is the FWHM radius. This practise is based on equal area of field sizes rather than the empirical equivalent square concept used in broad beam guidance documents, which considers equal photon scatter contributions (IAEA, 2017).

The FWHM was determined from the lateral beam profiles and the equivalent square field sizes calculated using both methods. The difference of the field sizes in the equivalent square field and its impact on the FOF was determined. A PTW 60012 and a PTW 31018 were used for these measurements.

Various detectors were used to determine the variation of the equivalent square field determined with choice of a detector. Measurements were performed on a single day using a PTW 31018, PTW 60019, PTW 60012, PTW 31021 and PTW 31016. For measurements performed on various random days a PTW 60012, PTW 60019, PTW 31018, PTW 31016 and PTW 31010 were used. This exercise was performed using the machine jaws and using Brainlab demountable circular cones. For the measurements with cones, lateral beam profiles were measured using a PTW 60019, PTW 60012, and PTW 31021 and equivalent square fields were calculated and compared.

6.2.3 Determination, constancy and reproducibility of field output factors

6.2.3.1 Determination of the central axis for small field measurements and its impact on the accuracy of the treatment data

Reference dose measurements for small fields are dependent on the precise location of the CAX. The detector is positioned at the CAX when reference dose and FOF measurements are performed. It is thus crucial to accurately determine the CAX position. In small fields and unflattened beams, the point of maximum dose in a profile is difficult to determine accurately because of the size and/or resolution of most detectors. The information about the detectors used in this study is provided in section 6.1.2. The CAX determined from the scans as explained in section 6.2.1, for each detector, was then used to position each detector to perform the reference dose measurements. The centre of the radiation field was determined using an automated central axis deviation calculation. A step size of 0.1 mm and a dwell time of 0.4 s was used for performing measurements for all field sizes. The accuracy of positioning a detector at CAX was evaluated and how this impacted on the treatment data by evaluating the FOF measurements performed with that CAX.

6.2.3.2 Determination of field output correction factors.

Part of the commissioning data includes FOF measurements. These are defined as the absorbed dose to water at a reference depth in a non-reference field divided by the absorbed dose to water at a reference depth in a reference field for reference fields (Mayles, 2007; IAEA, 2017). Because of the independence of the dosimetric quantities on field size in broad beams, their FOF are determined as the ratio of their detector readings. But in small fields the dosimetric quantities such as perturbation factors, have a field size dependency. Because of this a FOCF is needed for the detector reading ratio (Andreo, 2017; IAEA, 2017).

For FOF measurements, data were collected in a 6 MV beam at 10 cm depth in a water phantom, gantry and collimator at 0^o unless otherwise stated and 100 MU were delivered to the reference point of a detector for each data point at a SAD of 100 cm for the linac. At least three series of measurements were performed for each data point. Detectors used were a PTW 31018, PTW 60019, PTW 60012, PTW 31021 and PTW 31016. The measurements with field sizes using the cones, were performed at depths 5 cm and 10 cm using a PTW 60019, PTW 60012, and PTW 31021. These depths were chosen because the electrons scattered from the collimator are negligible at these depths and thus there is no contribution from the electron contamination to the measurements.

For measurements using a Co-60 machine, the FOF data were collected at 10 cm depth in a water phantom, gantry and collimator at 0^o and irradiation delivered to the reference point of a detector for each data point at a SAD of 80 cm, for one minute. At least three series of measurements were performed for each data point using a PTW 31006, PTW 31016, PTW 31010, PTW 60019 and PTW 60012.

The FOF were calculated using equation 6.4 for clinical, non-reference field f_{clin} with respect to the 10 × 10 cm^2, machine specific reference field, f_{ref}. A scenario assuming the machine cannot achieve a reference field size of 10 x 10 cm^2, the biggest cone

size (diameter 3.0 cm) was assumed to be the machine specific reference field and the FOF were calculated using equation 6.4 but with respect to the 3.0 cm cone size.

$$\Omega_{Q_{\mathrm{clin}}Q_{\mathrm{ref}}}^{f_{\mathrm{clin}}f_{\mathrm{ref}}} = \frac{M_{Q_{\mathrm{clin}}}^{f_{\mathrm{clin}}}}{M_{\mathrm{ref}}^{f_{\mathrm{ref}}}} k_{Q_{\mathrm{clin}},Q_{\mathrm{ref}}}^{f_{\mathrm{clin}},f_{\mathrm{ref}}} \qquad 6.4$$

The FOCFs published in the IAEA TRS 483 were used for the calculation of the FOF at 6 MV. No FOCF was applied for the Co-60 data as there is currently no published data. From the results of Co-60 data a conclusion will be made on whether there is a need for the FOCF in the Co-60 beam.

6.2.3.3 Determination of the field output correction factor for the PTW 31021 detector

For a detector that did not have published data, the PTW 31021, the FOF were calculated using a PTW 60012 and PTW 60019 as reference detectors. Then equation 6.5 was used to calculate the FOCF (IAEA, 2017)

$$k_{Q_{\mathrm{clin}},Q_{\mathrm{msr}}}^{f_{\mathrm{clin}},f_{\mathrm{msr}}}(\mathrm{sfd}) = \frac{M_{\mathrm{Q_{clin}}}(\mathrm{ref}) \times k_{Q_{\mathrm{clin}},Q_{\mathrm{msr}}}^{f_{\mathrm{clin}},f_{\mathrm{msr}}}(\mathrm{ref}) \Big/ M_{\mathrm{Q_{msr}}}(\mathrm{ref})}{M_{\mathrm{Q_{clin}}}(\mathrm{sfd}) \Big/ M_{\mathrm{Q_{msr}}}(\mathrm{sfd})} \qquad 6.5$$

where the M_Q(ref) is the reading of a reference detector in a field of quality Q corrected for influence quantities and M_Q(sfd) is the reading of a detector in the small field corrected for influence quantities. The acronyms clin and msr representing clinical field and machine specific reference field respectively. The results from using equation 6.5 were compared with values obtained using an analytical function method proposed by Sauer et. al. This method used an analytical function given in 6.6 to estimate the FOF for the semiflex 3D thimble chamber (PTW 31021) detector (Sauer, 2007).

$$\Omega(S_{\mathrm{clin}}) = P_{\infty} \frac{S_{\mathrm{clin}}^{n}}{l^{n} + S_{\mathrm{clin}}^{n}} + S_{\infty}(1 - e^{b \cdot S_{\mathrm{clin}}}) \qquad 6.6$$

where P1, S1, l, n and b are the fitting parameters, adjusted according to a routine, which optimizes the maximum likelihood estimation (MLE) (Casar, 2019 and Sauer, 2007). These FOF were normalised to the FOF of the 10 x 10 cm^2 field.

6.2.3.4 Variation of the field output factors with detectors

The beams were scanned using various detectors, given in section 6.2.3.2 for various field sizes. The choice of field sizes used for the linac were 10 x 10 cm^2, 6 x 6 cm^2, 4 x 4 cm^2, 3 x 3 cm^2, 2 x 2 cm^2, 1 x 1 cm^2 and 0.6 x 0.6 cm^2. Initially the intention was to use 0.5 x 0.5 cm^2, but the machine was not physically able to achieve this square field size. For the Co-60 measurements, the field sizes were 10 x 10 cm^2, 6 x 6 cm^2, 4 x 4 cm^2, 3 x 3 cm^2, 2 x 2 cm^2 and 1 x 1 cm^2. The field sizes were measured at various time intervals chosen based on the availability of the machine. Some of the data were after a calibration of the MLC's for the linac. This was done to determine the repeatability and reproducibility of measurements and the variation of the measured field size between the calibration of MLC and immediately after the calibration of MLC in order to determine how the variation of the measured field sizes affects the accuracy of the measured FOF data. The FOFs determined were compared with silver data, from the British Journal of Radiology (BJR) 25 (BJR-25, 1996), data from some of the local hospitals obtained from their treatment planning data and data obtained from other centres participating in the IAEA coordinated research project [E24021: "Testing of Code of Practice on Small Field Dosimetry"].

As the linac had a capability of attaching cones, data were also collected for this set up. The machine jaws were at 5 x 5 cm^2 for all the cone measurements. The alignment of the machine with the water tank, was performed as previously stated in section 6.2.1 without the cone attachment. Once this was verified to be within the required uncertainty the cone was attached. The cones used were circular and of diameters 30 mm, 25 mm, 20 mm, 17.5 mm, 15 mm, 12.5 mm, 10 mm and 7.5 mm. The scanning was performed along the major axes.

6.2.3.5 Variation in the determination of field size and field output factor with detector orientation

Measurements were performed to check if there was any variation in the data obtained with a PTW 31018 and PTW 31021 oriented parallel and perpendicular to the beam.

The measurements were performed in a 6 MV beam only. The water phantom was not moved when the orientation of an ionisation chamber was changed. This was to minimise contributors to the measurement uncertainties that could lead to different results from the two orientations. For each chamber orientation set up, lateral scans were performed to confirm the CAX and determine field sizes. The FOFs were then measured at the CAX.

Another set of data were obtained with the detectors oriented parallel to the beam in order to determine the field size however, FOF measurements were performed with the ionisation chamber oriented perpendicular to the beam. The smallest field size was used to confirm the positioning of a detector as it was expected that a deviation from the CAX would contribute significant errors in the determination of FOF.

6.2.3.6 Variation of equivalent square field size, S_{clin}, with MLC movement and calibration and its effect on field output factor

MLC calibrations were scheduled to be performed at least every three months on the linac. The field sizes were measured at various time intervals, chosen randomly. Some of the measurements were taken at 37 and 94 days after a calibration of the MLC's. This was done to determine the repeatability and reproducibility of the field size within the calibration period of the MLC, and how the variation of the measured field sizes affected the accuracy of the FOF data.

6.2.3.7 Variation of equivalent square field size, S_{clin}, and the field output factor measurements with induced gantry and collimator errors

The impact of errors in gantry settings of a linac was verified using a PTW 60012, PTW 60019 and PTW 31018 for field sizes 10 x 10 cm^2, 6 x 6 cm^2, 4 x 4 cm^2, 3 x 3 cm^2, 2 x 2 cm^2,1 x 1 cm^2 and 0.6 x 0.6 cm^2. The detector was positioned with its reference point at CAX with collimator and gantry at 0^o. The gantry was then deliberately varied by 0.5^o, 1^o, 1.5^o, 2^o and 5^o. The CAX was determined as detailed in section 6.2.3.1 for each field size and gantry angle and used to position the detector's reference point for performing reference dose and charge measurements. The variation of the field size

and the calculated FOFs with the different induced gantry errors were calculated. The exercise was also performed for different collimator settings using a PTW 60019 and PTW 31018.

Likewise, data were collected with the collimator at 5^{o} and the gantry varied to 0.5^{o}, 1^{o}, 1.5^{o}, 2^{o} and 5^{o}; and with the gantry at 5^{o} and collimator setting varied to 0.5^{o}, 1^{o}, 1.5^{o}, 2^{o} and 5^{o}. The detectors used for this were a PTW 60019 and a PTW 31018. These measurements were performed in the linac 6 MV photon energy beam only. The detectors were oriented parallel to the beam.

6.2.4 Measurements with and without a reference chamber

A PTW 34091 plane parallel chamber (T-Ref), was placed in the field as shown in figure 6.8. The distance of the chamber from the surface of the water was 30 cm. The intention of using the T-Ref was to establish whether there is any significant difference in the data collected with or without the T-Ref for small static fields data. Percentage depth dose and the FOF measurements were performed.



Figure 6.8 The setup of a PTW 34091 ionization chamber placed 30 cm from the surface of the water.

6.2.5 Beam quality Indices

$TPR_{20,10}(S)$ was measured as a ratio of measurements in water at SAD 100 cm using different detectors. The results were used to calculate $TPR_{20,10}(10)$ using equation 4.7. Also, the relation between $TPR_{20,10}$ and $PDD_{20,10}$ as given in equation 3.8 was compared with the results obtained. These data were collected for a PTW 60019, PTW 60012, PTW 31021, PTW 31018, PTW 31016 and PTW 31010 detectors.

6.2.6 Traceability of measurements with different small field detectors

Ionisation chamber calibrations in terms of absorbed dose to water are performed at reference conditions described in protocols like the IAEA TRS 398 (IAEA, 2000) in a Co-60 beam (Q_0), a field size of 10 x 10 cm^2 using an ionisation chamber at a depth in water of 5 g/cm^2 or 10 g/cm^2 and source to chamber distance of 100 cm. A calibration coefficient $N_{D,w,Q0}$ is then calculated for that ionisation chamber and its electrometer,

if calibrated as a unit. When the ionisation chamber together with its associated electrometer, referred to in this document as a detector, are used in a different beam quality, Q, than the one used for performing the calibrations, the absorbed dose to water is then given by equation 3.7. However, not all machines that use small fields can achieve a 10 x 10 cm^2 reference field.

Alfonso et. al. (Alfonso, 2008) suggested a new formalism that was also adopted, with some adjustments, by the IAEA protocol (IAEA, 2017). The formalism allows for the small static field dosimetry to be traceable to a broad beam calibration by introducing a machine specific reference (msr) field for machines that cannot establish a conventional reference field. This formalism was tested when calibrating small field detectors using a PTW 30013 that was traceable to an SSDL under conventional conditions. Small field detectors were cross calibrated, also known as daisy chaining, against a 0.6 cc Farmer type chamber at an SSD of 90 cm, depth 10 cm. The cross calibration was performed at a “virtual” machine specific reference (msr) field of 6 x 6 cm^2 for linac and the Co-60 machine. The calibration coefficients were then determined for the small field chamber in the “virtual" msr fields. The measurements were corrected for influence quantities. The small field detectors were then used for measurements in the small fields using the calibration coefficient obtained in a “virtual” msr field. The absorbed dose to water in a small field was obtained using the equation 6.7 where $N_{D,w,Q\mathrm{msr}}$ is a calibration coefficient determined in the “virtual” msr field and M_{Qsf} is the dosimeter reading corrected for all influence quantities other than beam quality in a small field.

$$D_{w,Q_{\mathrm{sf}}} = M_{Q_{\mathrm{sf}}} N_{D,w,Q_{\mathrm{msr}}} \qquad 6.7$$

6.3 Estimation of uncertainties

6.3.1 Reference measurements

The IAEA TRS 483, code of practise for small static fields, followed the formalism suggested by Alfonso et al (Alfonso, 2008), with some variation, for small fields and introduced a concept of a machine specific reference (msr) field (IAEA, 2017). This is

for machines where a reference 10 x 10 cm^2 field side cannot be achieved. The msr field needs to have dimensions very close to the reference field to minimise the uncertainty in the calibration coefficient caused by the difference in calibration conditions and that of the msr field. The msr field must extend beyond the outer boundaries of the detector used by a distance r_{LCPE}, where r_{LCPE} is the radius of the lateral charged particle equilibrium of the users beam quality (IAEA, 2017). The r_{LCPE} establishes the relation between the field size and the detector size for which lateral charged particle equilibrium exists. The absorbed dose to water for the msr field is then given by using equation 4.2.

To estimate the combined standard uncertainty in the determination of the absorbed dose to water for small fields, equation 4.2 is a model equation used for identifying uncertainty contributors. The identified uncertainty contributors were:

- u_M uncertainty associated to the electrometer readings;
- u_{NDW} uncertainty associated with the calibration coefficient provided by the calibration laboratory;
- u_{kQ} uncertainty associated with the k_Q factors;
- u_R repeatability, and
- u_{STD} short- and long-term stability of a standard detector.

More than one set of measurements were performed to obtain the required data, and the uncertainty linked to the repeatability (u_R) of the measurements and the measurement setup, also contributed to the overall uncertainty. This was determined as explained in 5.1.2. The short- and long-term stability of a standard detector contributed to measurement uncertainty. This was determined by observing the behaviour of a detector over a short term and a long term when the detector was irradiated with a reference source and taking into consideration all influence quantities and correcting for them. The chamber response for any day is corrected for decay of the source to the first day of observation. Then the standard deviation is used assess the data. This uncertainty contributor in this work is given as u_{STD}. Then,

$$\boldsymbol{u_{D_w}} = \sqrt{\boldsymbol{u_M}^2 + \boldsymbol{u_{NDW}}^2 + \boldsymbol{u_{k_Q}}^2 + \boldsymbol{u_R}^2 + \boldsymbol{u_{STD}}^2} \qquad 6.9$$

6.3.1.1 Uncertainty linked to the electrometer reading $M_{Q_{msr}}^{f_{msr}}$, u_M

The measurement uncertainty associated with the dosimetry system, electrometer and a detector, is dependent on the resolution of the electrometer and the repeatability of the measurements performed using that dosimetry system. The repeatability is given by the standard deviation of the mean of the measurements. The resolution of the detector is given by the manufacturer on the instrument specification. The best practice is to have more than three readings per data point, and this contributor is identified as u_{elec}. Because the data is dispersed assuming a constant source output, a Gaussian probability density function is chosen. The electrometer needs to be traceable to the international system for the units of measurement. If the electrometer is calibrated together with the detector then its calibration co-efficient will be combined with that of the detector together with its associated uncertainty. But should the electrometer be calibrated independently then it will have its own calibration coefficient with its associated uncertainty of measurements. It is common practice in South Africa that the detector is calibrated together with its detector and one calibration coefficient is given as described in 6.3.1. For this study it will be assumed that the electrometer and detector were calibrated as a unit.

The electrometer readings are corrected for all influence quantities such as ambient conditions, variation of the end user beam to that of the calibrating laboratory. The correction for the ambient conditions is based on the measured temperature, pressure and relative humidity. Each of the instruments used need to be calibrated. There is an uncertainty linked to the calibration of the instrument together with its resolution. Depending on the procedure applied at each facility, ambient condition correction may be performed for each point or the ambient conditions are measured with the first and last point and an average used to correct that data set. Correction for each point yields less uncertainty in the correction factor compared to that of the average used for each data point especially when there are drastic changes in pressure which cannot be controlled during measurements. For this work, the temperature and pressure measurements were taken at the beginning and end of each set. These uncertainty contributors are referred to as u_T, u_P and u_H indicating uncertainty linked to temperature, pressure and relative humidity measurements.

The positioning of a detector during the setup has an impact on the readings. This also speaks to the beam profile flatness and ability to position the detector on the same position of the beam profile especially for those that are not flat. This is more significant when using small fields and flattening filter-free (FFF) beams as the beam profile slopes significantly compared to broader beams. The other contributing factor to the positioning of a detector is the ability of the moveable collimators to move back to the same position for each field size. The variation of this capability contributes to the measurements. These uncertainty contributors related to the positioning of the detector are collectively referred to as u_{pos}. For these contributors, it was assumed that the data is dispersed, and a Gaussian probability density function was chosen.

$$\boldsymbol{u_M = \sqrt{u_{elec}{}^2 + u_T{}^2 + u_P{}^2 + u_H{}^2 + u_{POS}{}^2}} \qquad 6.10$$

6.3.1.2 Uncertainty linked to the calibration coefficient $N_{D,w,Q_o}^{f_{ref}}$, u_{NDW}

This uncertainty contributor is imported from the calibration laboratory. There are calibration laboratories that can provide calibration coefficients or calibration factors for user reference standards in beam qualities like those of the end user. The calibrations are mainly performed in a ^{60}Co beam and their estimated relative expanded uncertainty, for a 95 % confidence level k = 2, ranges from 0.7 % to 3.5 % according to the BIPM key comparison database (KCDB) where the calibration measurement capabilities for various national metrology institutes have been published. For the calibration laboratories that disseminate traceability using the photon beam energies, the estimated relative expanded uncertainty, for a 95 % confidence level k = 2, ranges from 0.8 % to 2.5 % according to the BIPM KCDB. This uncertainty is classified as a type B, and as a rectangular distribution as it is the range value given as a calibration coefficient with its uncertainty (JCGM, 2009).

In instances that the end user has a calibration coefficient for its reference chamber from a PSDL/SSDL and needs to cross calibrate their field chamber, the chambers are placed in a water phantom with their reference point at a reference depth

alternately under the same reference conditions. Using equation 4.2 the calibration coefficient may then be determined as follows:

$$\left[N_{D,w,Q_o}^{f_{ref}}\right]_{field} = \frac{\left[M_{Q_{msr}}^{f_{msr}} N_{D,w,Q_o}^{f_{ref}} k_{Q_{msr}Q_o}^{f_{msr},f_{ref}}\right]_{ref}}{\left[M_{Q_{msr}}^{f_{msr}}\right]_{field}} = \frac{\left[D_{w,Q_{msr}}^{f_{msr}}\right]_{ref}}{\left[M_{Q_{msr}}^{f_{msr}}\right]_{field}} \qquad 6.11$$

If the end user obtained the calibration coefficient/factor for their reference standard in an msr field already then:

$$\left[N_{D,w,Q_o}^{f_{ref}}\right]_{field} = \frac{\left[M_{Q_{msr}}^{f_{msr}}\right]_{ref}}{\left[M_{Q_{msr}}^{f_{msr}}\right]_{field}} N_{D,w,Q_o}^{f_{ref}} \qquad 6.12$$

The uncertainty contributors are similar to those discussed in section 6.3.1.

6.3.1.3 Uncertainty linked with the k_Q values, u_{kQ}.

If end users obtain their traceability from institutes using a Co-60 beam and are performing measurements in a linear accelerator photon beam, a correction for the variation of the beam quality from that used for calibrating the reference detector to the one used at a clinic is needed. $k_{Q_{msr}Q_o}^{f_{msr},f_{ref}}$ is a correction factor for the variance in the response of the detector in a reference beam, f_{ref}, with beam quality Q_o with that in the msr field with beam quality Q_{msr}. Some primary standard laboratories that have linear accelerators can provide $k_{Q_{msr}Q_o}^{f_{msr},f_{ref}}$ for various beam qualities and will provide the uncertainty associated with its measurement. Most end users however depend on published data for these. Protocols like the IAEA TRS 398, AAPM TG51 and IAEATRS 483 publish $k_{Q_{msr}Q_o}^{f_{msr},f_{ref}}$ for some detectors and Q_{msr}. The IAEA TRS 398 and IAEA TRS 483 estimated the relative standard uncertainty to their published $k_Q^{f_{ref}}$ data to be 1 % (IAEA, 2017). The data published in the AAPM TG 51 have an associated uncertainty of 0.5 % (McEWEN, 2014 and IAEA, 2017). The data published in the IAEA was used for the $k_Q^{f_{ref}}$ and the associated uncertainty is estimated not to exceed 1 %. These estimated uncertainties only apply to the data published in these guidance documents. The k_Q values published are given dependant on the detector choice and the beam quality index of the machine, $TPR_{20,10}(10)$ or PDD (10,10), measured in broad beams. For small static fields, these may be measured at a machine specific reference field

(msr) if the machine cannot achieve a 10 x 10 cm^2 field size and the $TPR_{20,10}(10)$ calculated using equation 4.7.

6.3.2 Relative measurements

The field output factors were determined following the IAEA TRS 483 guidelines and using equation 6.4. Equation 6.4 was used as the model equation to identify the uncertainties linked to the determination of the field output factors, $u_{\Omega_{\text{clin}}}$. The identified uncertainty contributors were:

- $u_{M_{\text{clin}}}$ and $u_{M_{\text{msr}}}$ uncertainty associated with the determination of $\boldsymbol{M_{Q_{\text{clin}}}^{f_{\text{clin}}}}$ and $\boldsymbol{M_{Q_{msr}}^{f_{msr}}}$ respectively,
- u_{FOCF} uncertainty of the FOCF.

Therefore

$$u_{\Omega_{\text{clin}}} = \sqrt{u_{M_{\text{clin}}}^2 + u_{M_{\text{msr}}}^2 + u_{FOCF}^2} \qquad (6.13)$$

6.3.2.1 Uncertainty associated with the determination of $\boldsymbol{M_{Q_{clin}}^{f_{clin}}}$ and $\boldsymbol{M_{Q_{msr}}^{f_{msr}}}$

The uncertainties linked to the determination of $\boldsymbol{M_{Q_{\text{clin}}}^{f_{\text{clin}}}}$ and $\boldsymbol{M_{Q_{msr}}^{f_{msr}}}$ are u_{MC} and u_{MM} respectively. The significant contributors to these that were identified were the uncertainty in the positioning of the detector in the point of the maximum dose, u_{pos}, and the uncertainty of electrometer reading u_{elec}. The u_{elec} was estimated based on the repeatability of the electrometer readings corrected for influence quantities and taking into consideration the variation of the beam output. The contributors to u_{pos} were:

- The uncertainty contributed by the reproducibility of the collimating system, u_{col}, identified by determining the collimator's ability to produce the required field size with the same centre. This was determined by measuring the dose at CAX repeatedly whilst keeping all parameters constant except for the collimator settings. The initial dose measurements were taken at a field size of

investigation. Then the field size increased to maximum field size of the study and then brought back to the field size under investigation. As an example, for the estimation of uncertainty in the field size of 0.6 x 0.6 cm^2 the collimator settings were changed from 0.6 x 0.6 cm^2 to 10 x 10 cm^2 and back to 0.6 x 0.6 cm^2 and dose measurements taken. This was repeated at least three times.

- The uncertainties associated with the determination of the beam centre, the determination of CAX. This was determined for each field size by repeating the measurements of CAX whilst keeping all parameters the same.
- The uncertainty of the scanning system, u_{scn}, which includes the accuracy, resolution and reproducibility of the scanning system.

Therefore

$$u_{pos} = \sqrt{u_{col}^2 + u_{scn}^2 + u_{cax}^2} \qquad (6.14)$$

6.3.2.2 Uncertainty associated with the FOCF, u_{FOCF}

As the FOCFs that were used were those published in the IAEA TRS 483, the uncertainties published were also used. For this the uncertainty in determining the S_{clin}, $u_{S_{clin}}$, contributes to u_{FOCF} as these are looked up on the table using the determined S_{clin}.

For the detector that did not have published FOCF, equation 6.5 was used to calculate them. The uncertainty contributors were:

- uncertainty associated with the FOCF of the reference detector, $u_{FOCF}(ref)$, as published in the IAEA TRS 483;
- uncertainty associated with $M_{Q_{clin}}(ref)$ and $M_{Q_{msr}}(ref)$, u_{rmc} and u_{rmm} which are uncertainties linked to the measurements performed using a reference detector in a clin and msr beams respectively;
- uncertainty associated with $M_{Q_{clin}}(sfd)$ and $M_{Q_{msr}}(sfd)$, u_{smc} and u_{smm} which are uncertainties linked to the measurements performed using a small field detector (sfd) in a clin and msr beams respectively.

The uncertainties associated with measurement of various *M* is determined as described in section 6.3.2.1. For the calculated FOCF,

$$u_{\mathrm{FOCF}} = \sqrt{u^2_{\mathrm{FOCF}}(\mathrm{ref}) + u^2_{\mathrm{rmc}} + u^2_{\mathrm{rmm}} + u^2_{\mathrm{smc}} + u^2_{\mathrm{smm}}} \qquad (6.15)$$

7. Results and discussions

7.1 Alignment of the water phantom with the gantry

Measurements were performed to ensure the water tank was positioned exactly perpendicular to the beam. Minor adjustments in gantry settings were made until the maximum difference in the CAX obtained from sequential cross plane profile measurements measured at depths of 5 cm, 10 cm and 20 cm was 0.5 mm. This equates to a 0.2^{o} mechanical tilt of the gantry or an offset in the beam focussing system or an asymmetry in the central leaf pair and was factored into the uncertainty of the measurements. About 5 % of the measurement set ups had to be adjusted because there was a tilt of more than 0.2^{o}. For each set up therefore, reliance was not only on physical (visual and sprit level) settings but also on the results from these initial profile measurements.

7.2 Determination of the equivalent square field size

Table 7.1 shows calculated S_{clin} and ESQ determined using equations 6.1 and 6.2 in the 6 MV beam and the FOFs measured with a PTW 60012 detector. The formulae give values that differ by ≤ 0.008 cm when the length and width values do not differ substantially. The data show a difference that increases as the field gets smaller and the measured length and width differ more from each other. The difference in the nominal field size of 2 x 2 cm^2 is 0.02 cm and increases to 0.04 cm and 0.05 cm for the nominal field sizes of 1 x 1 cm^2 and 0.6 x 0.6 cm^2 respectively. These differences are insignificant as they are smaller than the positioning uncertainty and the resolution of the stepper motor for setting up the detectors. For elongated fields where the length or width is bigger relative to the other, equation 6.1 will be dominated by the side that is bigger and not so for equation 6.2, suggested by Cranmer-Sargison and adopted in the IAEA TRS 483. Further studies need to be performed for elongated fields where the length or width will be significantly larger than the other side.

When comparing the FOFs determined using these calculated field sizes the difference is only noticeable at the set field sizes ≤ 1 cm, where it is 0.2 % for set field size of 1 x 1 cm^2 and 0.5 % for set field size of 0.6 x 0.6 cm^2. The uncertainty associated with the field size measurements using a PTW 60012 detector is 0.06 cm and the highest uncertainty in the determination of the FOF is 1.7 % both for a coverage factor of k = 2, equal to confidence level of 95 %. As the percentage difference in the FOFs is less than the associated uncertainty of measurement the conclusion is that the use of equation 6.1 or 6.2 would yield results within the measurement uncertainty of 0.06 cm for the determination of the S_{clin}.

Table 7.1 S_{clin} and ESQ determined using equations 6.1 and 6.2 in the 6 MV beam and the FOFs obtained with a PTW 60012. The uncertainties associated with the measurements of the field size was 0.06 cm.

Nominal field size (cm^2)	Measured field size (cm^2)	S_{clin} (cm)	ESQ (cm)	FOF using S_{clin}	FOF using ESQ
10 x 10	10.012 x 9.816	9.913	9.916	1.000	1.000
6 x 6	5.984 x 5.707	5.843	5.836	1.010	1.010
4 x 4	3.994 x 3.717	3.852	3.844	1.015	1.015
3 x 3	3.012 x 2.667	2.833	2.821	1.017	1.017
2 x 2	2.038 x 1.653	1.833	1.813	1.014	1.014
1 x 1	1.123 x 0.686	0.873	0.834	0.989	0.987
0.6 x 0.6	0.764 x 0.391	0.572	0.524	0.967	0.962

Table 7.2 shows data obtained when using a PTW 31018 detector for measuring and calculating S_{clin} and ESQ determined using equations 6.1 and 6.2 in a 6 MV beam and the FOFs. The biggest difference observed in the calculated equivalent square was 0.03 cm for set field size of 0.6 x 0.6 cm^2 and its associated FOF showed a variation of 0.3 %. There was no significant difference in the FOFs for the rest of the set field sizes. The uncertainty associated with the measurements of the FOFs using a PTW 31018 detector was estimated to be 2.9 % for the smallest field size. As the difference is smaller than the uncertainty these results also indicate that equation 6.1 or 6.2 may be used and will yield acceptable uncertainties.

Table 7.2 S_{clin} and ESQ determined using equations 6.1 and 6.2 in the 6 MV beam and the FOFs obtained with a PTW 31018. The uncertainties associated with the measurements of the field size was 0.06 cm.

Nominal field size (cm²)	Measured field size (cm²)	S_{clin} (cm)	ESQ (cm)	FOF using S_{clin}	FOF using ESQ
10 x 10	10.016 x 9.687	9.825	9.848	1.000	1.000
6 x 6	6.025 x 5.668	5.826	5.840	0.996	0.996
4 x 4	4.023 x 3.647	3.815	3.825	0.994	0.994
3 x 3	3.026 x 2.658	2.823	2.829	0.994	0.994
2 x 2	2.046 x 1.657	1.833	1.830	0.993	0.993
1 x 1	1.126 x 0.708	0.881	0.868	0.994	0.994
0.6 x 0.6	0.817 x 0.406	0.569	0.541	1.009	1.012

7.2.1 Equivalent square field determined using various detectors in MLC fields, measured over a period of 333 days

The equivalent square field size results of the measurements performed using various detectors for set field sizes using MLC and jaw is given in Table 7.3. All the detectors were positioned parallel to the beam. The data show an average of S_{clin} determined over a period of 333 days on 14 different days. Over this period, 8 MLC calibrations were performed. The highest uncertainty in the determination of the equivalent square field size was ≤ 0.06 cm. The S_{clin} determined varied within the uncertainty of its measurements. This is different than the data obtained by Casar et. al. (Casar, 2019) who observed that S_{clin} was nearly identical to the nominal field sizes for set field sizes ≥ 1 cm, and differed significantly for the two smallest fields, regardless of the energy or collimation (or linac) being used. For these data, even the smallest fields agreed to within the uncertainty of measurements. Comparing the data obtained using the ionisation chambers and the data obtained using the solid-state detectors the difference is not significant. A two tailed t-test assuming unequal variances was used, and the p-value was more than 0.05. The differences shown in table 7.3 could be due

to the repeatability and reproducibility of setting up the water tank on the different 14 days.

From the data presented in table 7.3 it is concluded the 3-monthly calibration of the machine yielded results that were within the measurement uncertainty for the determination of S_{clin}. However, the MLC calibration should be monitored between the services because it could affect the FOF measurements.

Table 7.3 The variation of the equivalent square field size as measured with different detectors for field sizes defined by an MLC and jaw. The result is the average of more than three sets of measurements obtained over a period of 333 days in the same 6 MV beam.

Nominal field size (cm)	PTW 60012	PTW 60019	PTW 31018	PTW 31016	PTW 31010	Average (cm)	Std dev (cm)
10 x 10	9.91	9.95	9.85	9.83	9.80	9.87	0.06
6 x 6	5.84	5.93	5.84	5.83	5.81	5.85	0.05
4 x 4	3.85	3.91	3.74	3.82	3.79	3.82	0.06
3 x 3	2.83	2.90	2.84	2.84	2.80	2.84	0.04
2 x 2	1.83	1.90	1.84	1.85	1.82	1.85	0.03
1 x 1	0.87	0.94	0.89	0.91	0.95	0.91	0.03
0.6 x 0.6	0.57	0.61	0.58	0.60		0.59	0.02

7.2.2 Equivalent square field determined using various detectors in MLC fields, measured in the same session

Figure 7.1 shows a variation of S_{clin} when measurements are performed in the same session using the detectors PTW 31018, PTW 60019, PTW 60012, PTW 31021 and PTW 31016 in the 6 MV beam for field sizes defined by an MLC and jaw. For each data point, the detector was positioned independently. The tank was set up once for that day and then used for all the measurements with the detectors. On 2 December 2017 data were measured using PTW 60012, PTW 60019 and PTW 31021 detectors; and on 27 January 2018 PTW 60012 and PTW 31018 detectors were used. For the

data collected on 3 February 2018, PTW 60012, PTW 31018 and PTW 31021 detectors and on 24 Feb 2018 the PTW 31018, PTW 60019, PTW 60012, PTW 31021 and PTW 31016 detectors were used. An inter-quartile range was used to evaluate if the data had any outliers for each day. Only the data measured on the 24 February 2018 had outliers and four out of the six outliers were measured using the PTW 31021 detector. The data on 24 February 2018 were measured three days before the calibration of the MLC and this contributed to the data being outliers. These outliers were not included in the calculation of the standard deviation of the mean as shown in figure 7.1.

Data measured on the 2 December 2016 showed the highest variation. The data measured using the PTW 31021 detector was significantly different than the data measured using the PTW 60012 and PTW 60019 detectors. The t-test performed on the data obtained using solid-state detectors with that of the PTW 31021 ionisation chamber yielded P values that were less than 0.05 implying the differences are significant. For the data measured on the 3 Feb 2018, the variation between the measurements performed using solid-state detectors was less than 0.7 % except for the smallest field size where it was about 6 %. The variation between measurements obtained using each solid-state detector and the PTW 31021 was more than 1 % increasing to about 24 % for the smallest field. The t-test calculated from the data obtained using solid-state and the PTW 31021 detectors indicated that the difference was significant, with a p value less than 0.05. The variation observed indicates that the PTW 31021 detector is not ideal for measuring small field sizes ≤ 2 cm. The variations is attributed to the perturbation factors of the detectors. Besides the detector choice, the ability of the MLCs to travel reproducibly to the required position could also be a contributor to the variations observed. The AAPM TG 142 recommends that the leaf positioning accuracy be 1 mm (Klein, 2009). The equivalent square field determination had a standard deviation that was lower than 1 mm for all measurements. This implies that the leaf positioning was within the recommended tolerance. The tolerance of 1 mm is, however, probably too generous for field sizes of S_{clin} < 1 cm as this would significantly impact the uncertainty in the FOF. From this study, it is recommended that the tolerance be 0.6 mm, as per the estimated measurement uncertainty, for field sizes of S_{clin} < 1 cm.

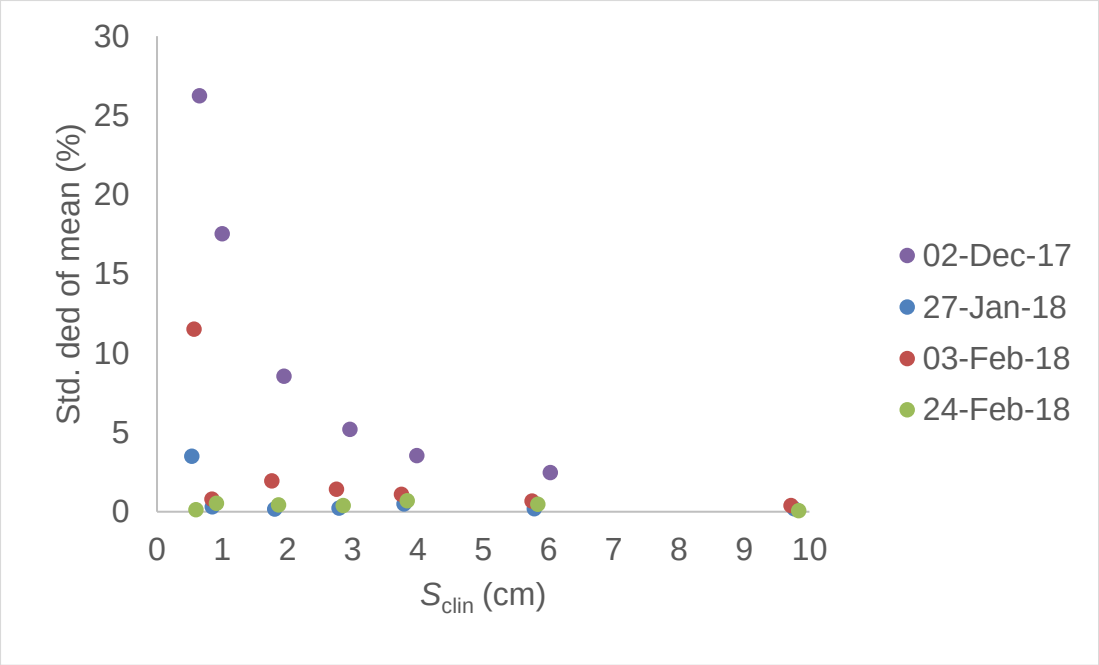


Figure 7.1 Standard deviation of the mean for measurements of S_{clin} that were performed using the detectors PTW 31018, PTW 60019, PTW 60012, PTW 31021 and PTW 31016 on the same day but measured on four different days, in a 6 MV beam for field sizes defined by an MLC and jaw.

7.2.3 Equivalent square field determined using various detectors in cone fields

Table 7.4 shows the variation of the equivalent square field size, S_{clin}, measured on same day at depth 10 cm in water at a SAD of 100 cm using PTW 60019, PTW 60012, and PTW 31021 detectors for a set of stereotactic cones of different diameters. Data were measured on the same day and the machine field size was 5 x 5 cm^2 for all cones. The variation in the data, expressed as the standard deviation, ranged from 0.03 cm to 0.06 cm and is shown in table 7.4. The variation is ≤ 0.06 cm which is the uncertainty for the field size measurements and is due to the detector choice and the setting up of each detector for the experiment.

Table 7.4 The equivalent square field size, S_{clin}, measured at depth 10 cm in a water phantom at a SAD of 100 cm using PTW 60019, PTW 60012, and PTW 31021 detectors for a set of stereotactic cones of different diameters. The data were measured on the same day.

Nominal cone diameter (cm)	S_{clin} (cm)	
	Average	Std dev
3	2.44	0.06
2.5	2.01	0.06
2	1.57	0.06
1.75	1.36	0.06
1.5	1.14	0.06
1.25	0.96	0.05
1	0.78	0.01
0.75	0.54	0.03

Table 7.5 shows the variation of the equivalent square field size, S_{clin}, measured at depth 10 cm in water phantom at an SAD of 100 cm using PTW 60019, PTW 60012, and PTW 31021 detectors for a set of stereotactic cones of different diameters on various days. These data were collected over a period of 28 months on four different days. Comparing the data using solid-state detectors the variation is ≤ 0.02 cm for all the cones. The variation in the data for all three detectors indicates that the solid-state detectors seemed to be more in agreement with each other than the air ionization chamber, PTW 31021. The results of the PTW 31021 air ionization chamber shows that it should not be used for measuring equivalent square field sizes ≤ 2 cm. This agrees with the results discussed in section 7.2.2. The PTW 31021 detector was positioned parallel to the beam for these measurements.

Table 7.5 The variation in the equivalent square field size, S_{clin} measured at depth 10 cm in a water phantom at a SAD of 100 cm using a PTW 60019, PTW 60012, and PTW 31021 detectors for a set of stereotactic cones of different diameters. The data were measured on four different days over a period of 28 months.

Nominal cone diameter (cm)	S_{clin} (cm)				
	PTW 60012	PTW 60019	PTW 31021	Average	Std dev
3	2.50	2.48	2.38	2.45	0.06
2.5	2.07	2.05	1.96	2.03	0.06
2	1.63	1.62	1.52	1.59	0.06
1.75	1.43	1.41	1.31	1.38	0.06
1.5	1.19	1.18	1.09	1.16	0.06
1.25	1.01	1.00	0.91	0.98	0.05
0.75	0.58	0.56	0.52	0.55	0.03

Table 7.6 shows the data of the variation of the equivalent square field size, S_{clin}, with detector choice for field sizes achieved using demountable cones measured at depth 5 cm in water at a SAD of 100 cm. The decision to perform a set of measurements at depth of 5 cm was to allow data to be compared with those of other centres that performed measurements at depth 5 cm. The standard deviation varied from 0.02 cm to 0.03 cm, which is within the uncertainty of 0.06 cm for measurements of field size. The PTW 31016 detector was positioned parallel to the beam.

Table 7.6 The variation of the equivalent square field size, S_{clin}, for demountable cones measured at a depth of 5 cm in water at a SAD of 100 cm using PTW 60012, PTW 60019 and PTW 31016 detectors.

Nominal cone diameter (cm)	S_{clin} (cm)				
	PTW 60012	PTW 60019	PTW 31016	Average	Std dev
3	2.51	2.49	2.44	2.48	0.03
2.5	2.08	2.06	2.02	2.05	0.03
2	1.64	1.63	1.59	1.62	0.02
1.75	1.43	1.41	1.37	1.40	0.03
1.5	1.20	1.19	1.16	1.19	0.02
1.25	1.02	1.00	0.98	1.00	0.02
1.0	0.80	0.79	0.76	0.78	0.02
0.75	0.59	0.57	-	0.57	0.02

7.3 Determination, constancy and reproducibility of field output factors

7.3.1 The impact of no CAX correction on the accuracy of the treatment data

Table 7.7 shows how a failure to correctly position a detector at the CAX impacts the FOF data. The PTW 31018 was set up as described in section 6.2.1 using the manufacturer's specification and lateral scans were performed to determine the equivalent square. The CAX that was determined from the profile measurements was not used to correct the zero position of the detector. The highest impact, as expected, was for equivalent square field ≤ 0.83 cm and this translated into $\underline{\geq}$ 13 % error in the FOF. This shows the importance of verifying CAX and not relying only on the set up using visual positioning, the manufacturer's specifications of a detector and an automated water tank positioning system. The CAX of the radiation field needs to be established for each detector and for each independent measurement set up.

Table 7.7 The variations in CAX and how they impact on the S_{clin} and the FOF data measured using a PTW 31018 detector.

S_{clin} (cm)	Variation in CAX (mm)		Variation (absolute)		Variation (%)	
	CAX IN	CAX Cross	S_{clin} (mm)	$\Omega_{Q_{clin},Q_{msr}}^{f_{clin},f_{msr}}$	S_{clin}	$\Omega_{Q_{clin},Q_{msr}}^{f_{clin},f_{msr}}$
5.76	1.03	1.51	0.1	0	0.1	0
3.77	1.06	1.69	0.1	0	0.1	0
2.74	1.02	1.69	0.1	0	0.3	0.1
1.75	1.04	1.65	0.1	0	0.3	0.2
0.83	1.01	1.54	0.2	0.1	2	13
0.52	0.84	1.64	0.2	0.1	2	32

7.3.2 Determination of field output correction factors.

When the project started the IAEA TRS 483 was not published and the data obtained for the FOFs with no correction factors for detectors as a function of S_{clin} and energy, showed a significant difference in the data. The various detectors used were those that are recommended in the IAEA TRS 483 guidance document except for the PTW 31021 detector which was not available when the CoP was published. Figure 7.2 shows the variance of field output factors versus S_{clin}, when various detectors were used to measure field size with no FOCF. This variation is pronounced for equivalent square fields ≤ 2 cm.

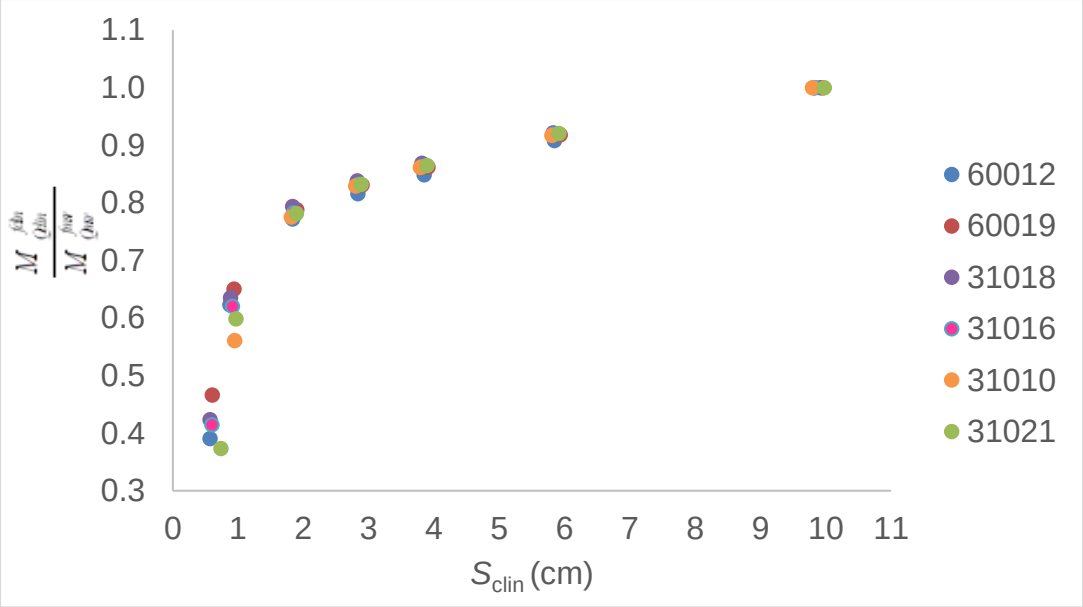


Figure 7.2 Variance of field output factors versus S_{clin}, when various PTW detectors were used to measure field size with no FOCF.

7.3.3 Determination of the field output correction factors for the PTW 31021 detector

Figure 7.3 shows the FOCFs that were determined using equation 6.5 that is published in the IAEA TRS 483 (IAEA, 2017) and those determined using the analytical function in equation 6.6 (Sauer, 2007). These may be used whether the ionisation chamber is orientated parallel or perpendicular to the beam. The data for those that were calculated using equation 6.6 are labelled Sauer-P and Sauer-T meaning the detector was oriented parallel and perpendicular to the beam respectively. For the rest of the data they were determined using a PTW 60012 and a PTW 60019 as reference detectors. Data are labelled #-P-60012 and #-T-60012 where # is the sequence in which the measurements were taken; P refers to detector orientation parallel to the beam and T refers to detector orientation perpendicular to the beam. The other numbers are the model numbers of the detectors. A two tailed student t-test showed that the difference between the FOCFs determined using both these methods is not significant as it yielded a p-value that was more than 0.05.

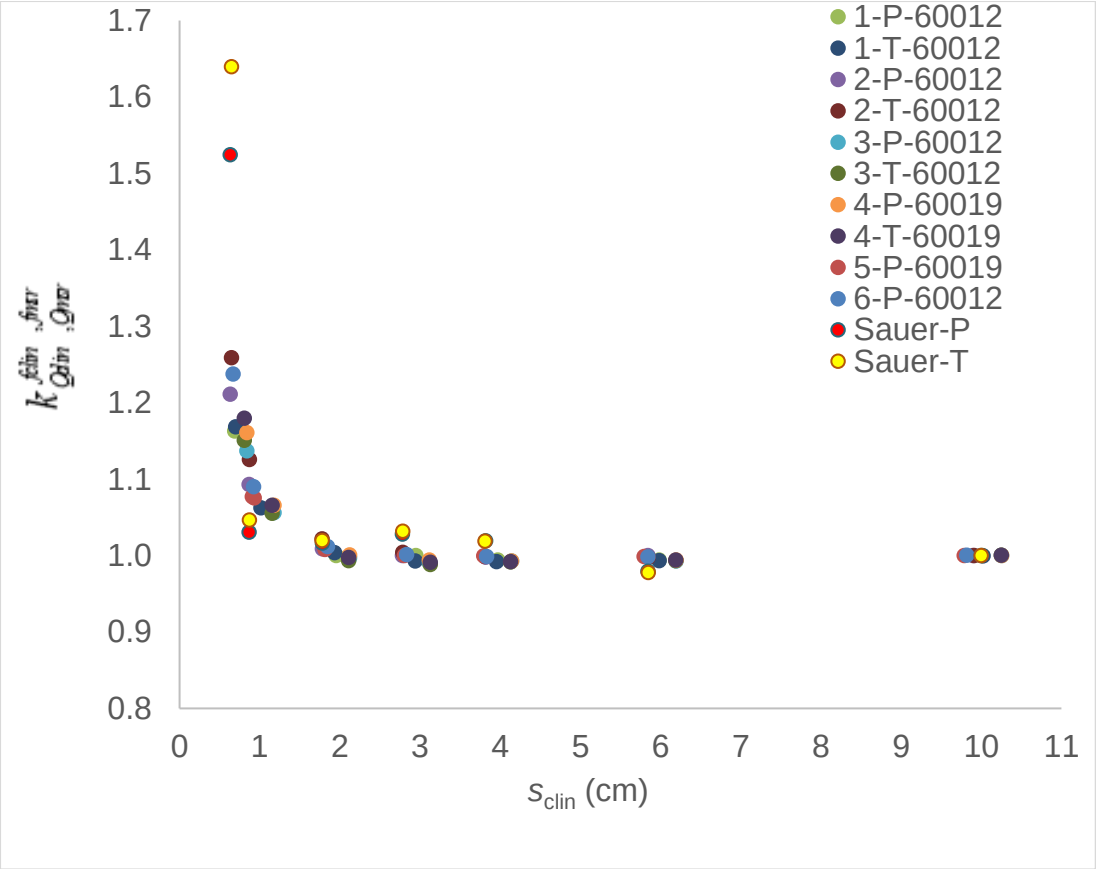


Figure 7.3 FOCFs derived for the PTW 31021 detector and determined from the FOCFs for the PTW 60019 and PTW 60012 detectors as published in the IAEA TRS 483. The graph also shows factors for the PTW 31021 determined using the analytical function suggested by Sauer (Sauer, 2007) and given as Sauer-P and Sauer-T. Data are labelled #-P-60012 and #-T-60012 where # is the sequence in which the measurements were taken; P refers to detector orientation parallel to the beam and T refers to detector orientation perpendicular to the beam. The other numbers are the model numbers of the detectors.

An inter-quartile range was used to evaluate if the data presented in figure 7.3 had any outliers and outliers were removed to calculate the average FOCFs given in table 8. It is not recommended to use this detector for $S_{clin} \leq 1$ cm as the FOCFs are more than 5 % and the relative measurement uncertainties for the FOCF more than what is needed for the desirably outcome of the dosimetry data. The relative measurement uncertainty given in table 7.8 is for a coverage factor of $k = 2$, equal to confidence level of 95 %.

Table 7.8 FOCF derived for the PTW 31021 from data presented in figure 7.3 together with the associated relative measurement uncertainty for a coverage factor of k = 2, equal to confidence level of 95 %.

S_{clin} (cm)	FOCF	u_{FOCF} (%)
10.0	1.000	0.2
6.0	0.996	0.6
4.0	0.995	0.7
3.0	1.00	1.1
2.0	1.00	1.9
1.0	1.08	2.0
0.8	1.2	26

7.3.4 Variation of the field output factors with detectors for a linac beam

FOFs determined using detectors PTW 60012, PTW 60019, PTW 31018, PTW 31016 and PTW 31021 are shown graphically in figure 7.4. The FOCFs for the PTW 31021 detector that were determined and reported in section 7.3.3 were used to calculate the FOFs. The FOFs using various detectors were determined over a period of 333 days on 14 different days during which MLC calibrations were performed periodically, at least every three months. Even though the data had been corrected using the FOCFs published in the IAEA TRS 483 (IAEA, 2017) there is still some variation observed in the FOF results shown. For all equivalent square field sizes, the variation in FOFs was more pronounced for $S_{clin} \leq 1$ cm: it was 3.6 % for S_{clin} of 1 cm and 2.6 % for S_{clin} of 0.6 cm. The estimated uncertainties of measurements for the field output factors measured at S_{clin} of about 0.6 cm were 1.7 %, 1.7 %, 2.9 % and 5.0 % when using PTW 60012, PTW 60019, PTW 31018 and PTW 31016 detectors respectively. For the S_{clin} of about 1 cm the estimated uncertainties were 1.3 %, 1.3 %, 2.1 %, 2.9 %, 7 %

and 6 % when using PTW 60012, PTW 60019, PTW 31018, PTW 31016, PTW 31021 and PTW 31010 detectors respectively. The biggest contributor to the uncertainty of measurements is the uncertainty from the FOCF. Eliminating the data from the detectors that has uncertainties ≥ 5 % for both S_{clin}, the variation decreases to 1.9 % for the S_{clin} of 1 cm and remains 2.6 % for S_{clin} of 0.6 cm. The variation observed is attributed to the size and perturbation of each detector leading to different measurement uncertainties in the determination of the detectors' FOCF. The uncertainty of measurement of the FOCF, as given in the IAEA TRS 483, for the S_{clin} of 0.6 cm was 0.7 %, 0.7 %, 1.4 % and 2.5 % when using PTW 60019, PTW 60012, PTW 31018 and PTW 31016 detectors respectively (IAEA, 2017).

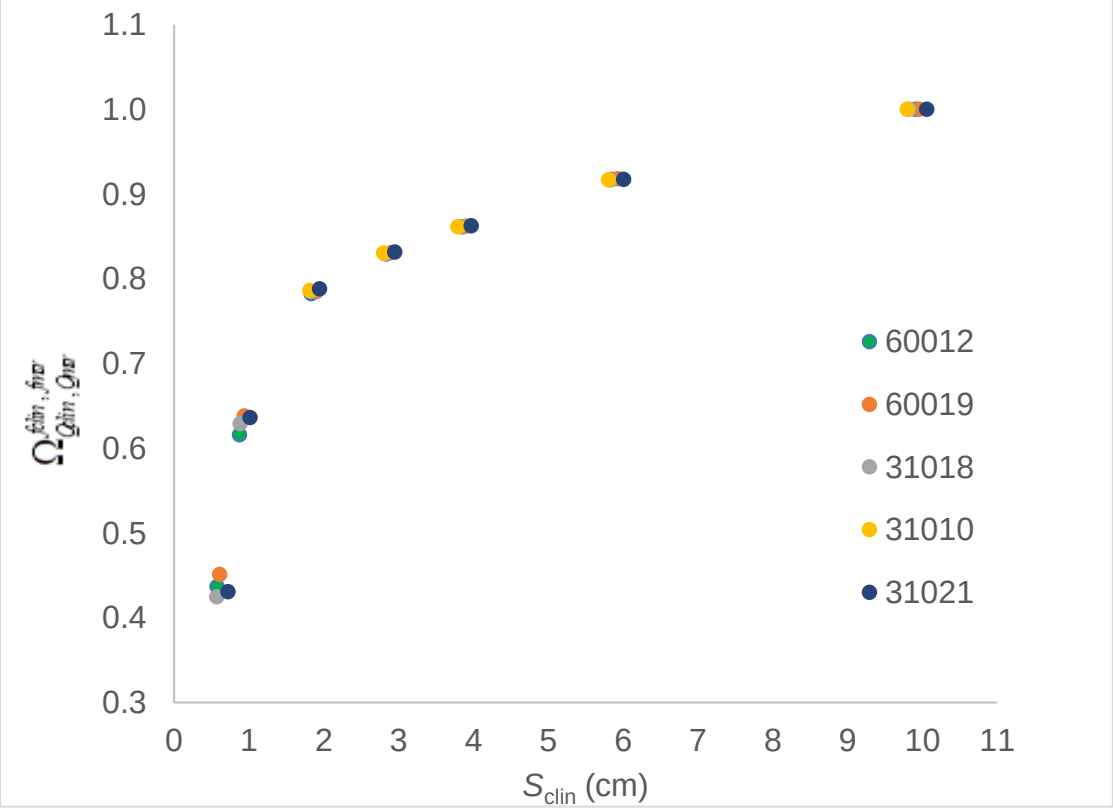


Figure 7.4 The FOFs versus the equivalent square field, $S_{clin,}$ determined using detectors PTW 60019, PTW 31018, PTW 31010, PTW 31021 and PTW 60012. The measurements were performed over a period of 333 days on 14 different days at various MLC calibration intervals, and the average of all the measurements is displayed here.

Data from other centres in South Africa were obtained. The data submitted by these centres were based on their treatment planning system dataset, which were measured before the publication of the IAEA TRS 483. Figure 7.5 shows the graphical representation of these data. Both centres were using an ELEKTA Synergy with Agility head. An average of the data measured by various detectors from this study, shown in figure 7.4, was used for the comparison. Centre E submitted data down to equivalent square field of 2 cm and centre D down to equivalent square field of 1 cm. The variation in the small S_{clin} that was common from these centres (4 cm, 3 cm and 2 cm) was about 1 % for all the field sizes. When comparing data from centres D and E, the highest variation in the FOF data was 1 % for the S_{clin} of 2 cm. An inter-quartile range was used to evaluate if the data submitted by centres D, E and the average of those determined at centre A had any outliers and none were found. The data from centre E, labelled as E were measured data and E - M were data obtained from the treatment planning system. The variation in the FOF data was < 1.1 % and the estimated uncertainty of measurement for the FOF at S_{clin} of 2 cm was 1.1 %.

Data from the BJR 25 (BJR-25, 1996) were also compared with the data from these centres, as shown in figure 7.5. Variations of more than 4 % were observed at the S_{clin} of 4 cm. The data for the field sizes < 4 cm were extrapolated. Comparing these data with data measured for this study shows variations > 5 % from S_{clin} of 3 cm and lower. This leads to a conclusion that the BJR data published for 6 MV should not be used for field sizes ≤ 4 cm.

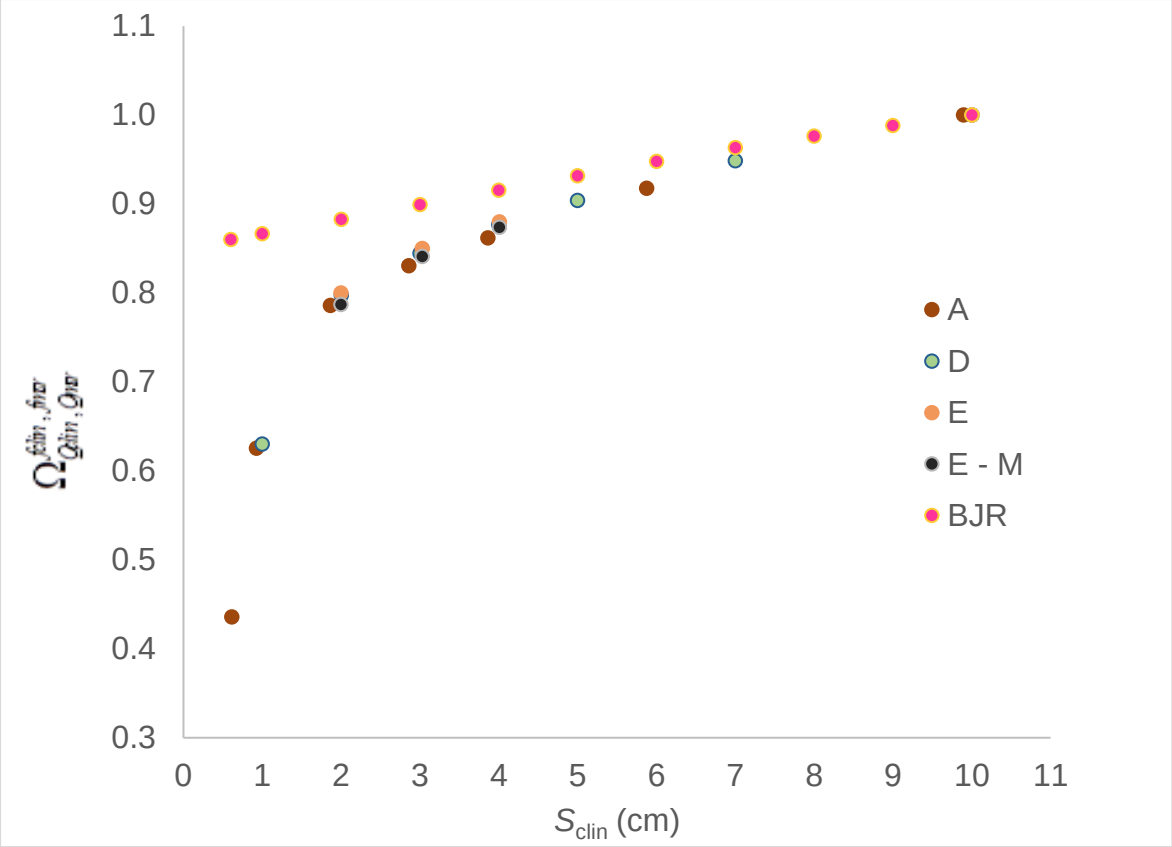


Figure 7.5 The measured FOF versus the equivalent square field, S_{clin}, from this study (A), and at centres D (D) and E (E and E-M). Data from treatment planning systems of centres D and E are labelled D and E-M respectively. BJR-25 data are also plotted (BJR-25, 1996).

Figure 7.6 shows data obtained for FOFs versus S_{clin} obtained using various detectors when the fields were defined by stereotactic cones in a 6 MV beam at a depth of 5 cm in water. An MLC calibration was not performed between the data sets and the data sets were repeated two weeks apart. Data were normalised to the msr field of cone diameter 3 cm, which was the biggest diameter cone available. The ionisation chamber, PTW 31016, was used down to the cone with diameter 1 cm. For the S_{clin} measurements, the highest standard deviation of the mean was 0.03 cm, which is within the uncertainty of measurements for measuring field size (0.06 cm). The variation in the FOFs determined by the various detectors was 2 % for cone diameter of 1 cm and 1 % for the 1.5 cm and 1.25 cm diameter cones. The FOFs varied by 0.5 % for the other cone diameters. These variations were due to the differences in the detector design leading to the different uncertainties of the detectors' FOCF. Using

an inter-quartile range, there were no outliers in the data for FOFs determined using these detectors. The uncertainty in determining the FOF using the PTW 31016 detector for S_{clin} of 2 cm to 1 cm ranges from 1.1 % to 2.3 % compared with those for the other detectors, which ranged from 1.1 % to 1.3 % respectively. It can be concluded that the variation is within the uncertainty of measurements.

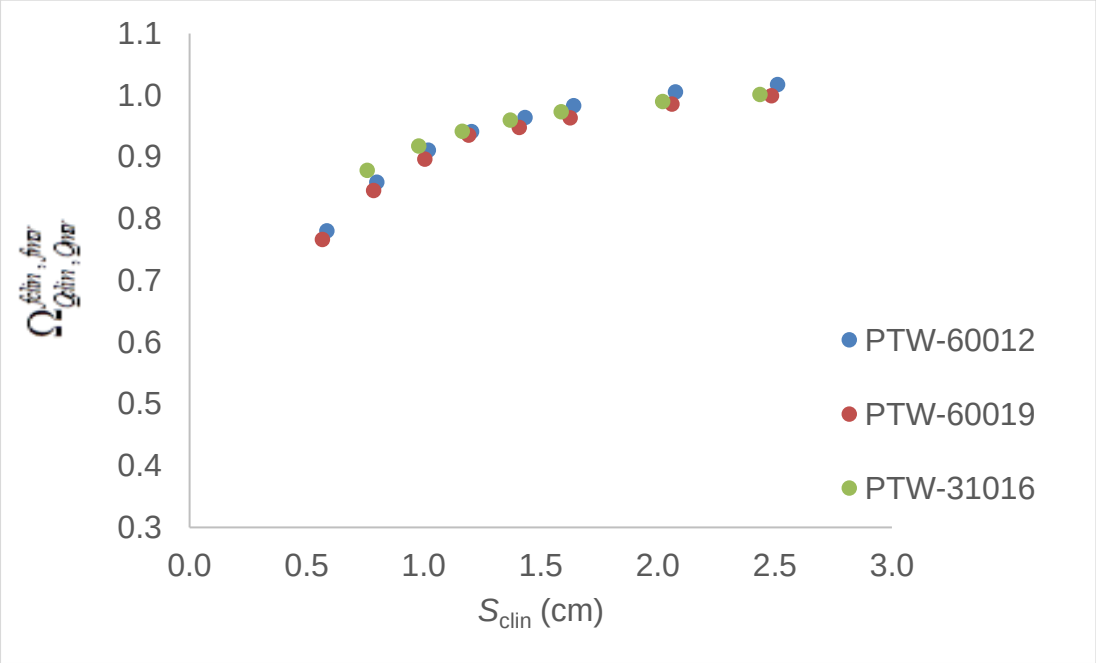


Figure 7.6 FOF versus equivalent square field measurements obtained from data using various detectors and demountable stereotactic cones at CMJAH in a 6 MV beam. The depth of the measurements was 5 cm in water with SAD of 100 cm.

Figure 7.7 shows a plot of the average data for the FOF versus S_{clin} obtained using various detectors (figures 7.8 to 7.10), and demountable cones at CMJAH (A) compared to the data from other centres (B and C). These measurements were performed in a 6 MV beam at depth 10 cm. The types of linacs used by centres A, B and C were the Siemens Primus, TrueBeam STx® and an Elekta Synergy respectively. Centre A fixed the jaw opening at 5 x 5 cm^2, centre B fixed jaw opening at 4 x 4 cm^2 for cones with a diameter > 1.0 cm and at 3 x 3 cm^2 for cones with diameter ≤ 1.0 cm, and centre C fixed their jaw opening at 6 x 6 cm^2. Centre C submitted data for cone diameters ≤ 1.5 cm. The FOCFs published in the IAEA TRS 483 (IAEA, 2017) were used by each centre. The maximum diameter of the cones varied from centre to

centre but data were normalised to the FOF of the conventional reference field size of 10 x 10 cm^2. Centre A used a SAD technique for their reference dosimetry data with centres B and C using a SSD technique. This was corrected for in the data presented. The cones with similar diameter sizes amongst all three centres were 1.5 cm, 1.25 cm and 1.0 cm.

There were no outliers on the data from measurements performed by these centres for the common cone diameters. The calculated standard deviations in the FOF data for cones with diameters 1.5 cm, 1.25 cm and 1.0 cm were 1 %, 0.7 % and 0.8 % respectively. These variations were within the measurement uncertainty for the determination of FOFs, as shown in table 7.15 to be ≤ 1.3 %. Figure 7.8 shows the data obtained using diamond detectors (PTW 60019); figure 7.9 shows data collected using diode detectors (PTW 60012, PTW 60017, PTW 60016 and IBA SFD) and figure 7.10 using ionisation chambers (PTW 31021 and PTW 31016). The data collected using the ionisation chambers were performed by centres A and B only. The reproducibility of the measurement set up from centre to centre contributed to the variation that is observed using these detectors. Data submitted by centre C when using diodes showed a % difference of about 4 %. This is evident in figure 7.9. This is because the PTW 60016 has a shield that causes perturbation effects in small fields. For the data measured using ionisation chambers, shown in figure 7.10, there is a notable variation for S_{clin} ≤ 1.5 cm agreeing with the earlier conclusion that the PTW 31021 is not ideal for use in S_{clin} < 2 cm.

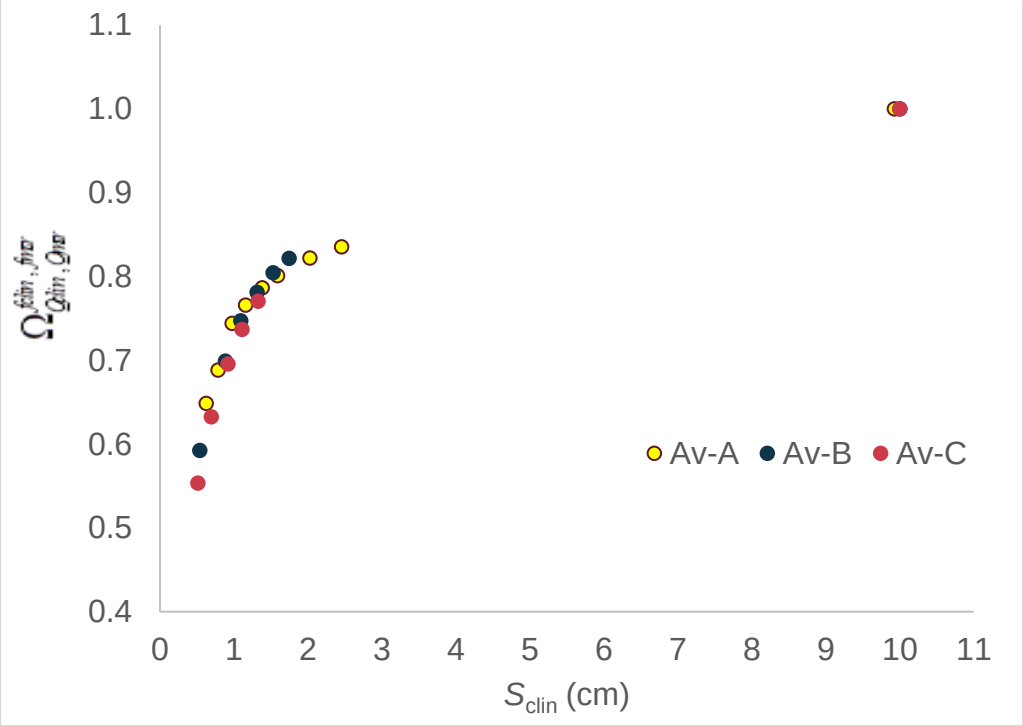


Figure 7.7 A plot of the average data for FOF versus S_{clin} measurements obtained from data using various detectors when the field is defined with Brainlab demountable cones at centres A, B and C. The depth of measurements was 10 cm and 6 MV was used by all centres. All data were normalised to 10 x 10 cm^2 field size.

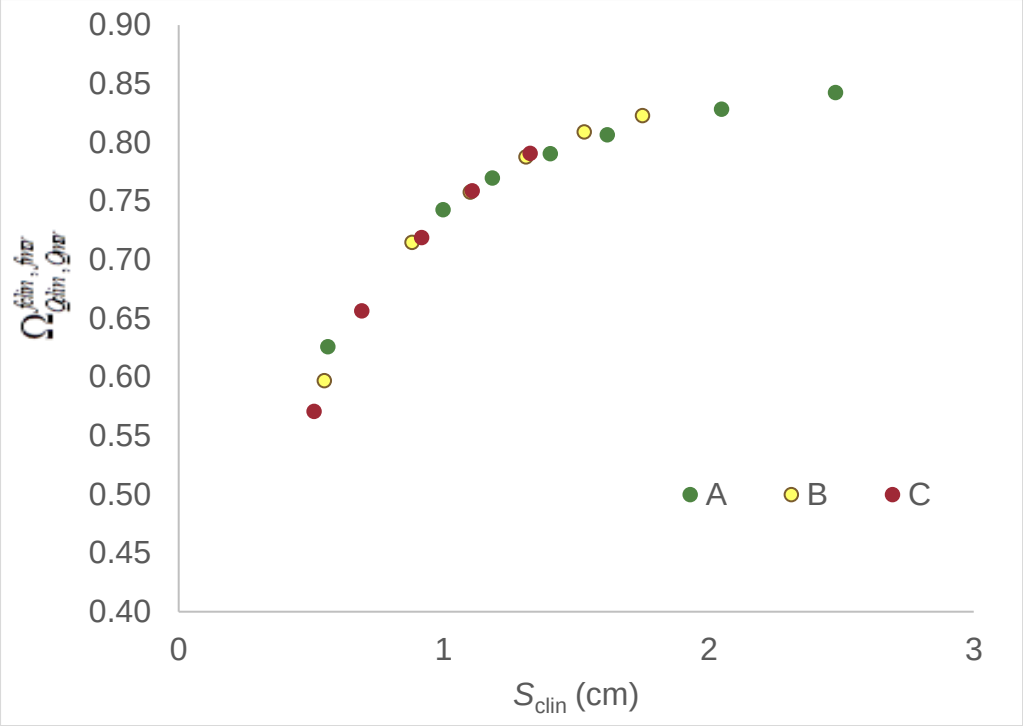


Figure 7.8 Data for FOF versus S_{clin} measurements obtained from data using only synthetic diamond detectors, PTW60019, when the field is defined with Brainlab demountable cones at centres A, B and C. The depth of measurements was 10 cm and 6 MV was used by all centres. All data were normalised to 10 x 10 cm^2 field size.

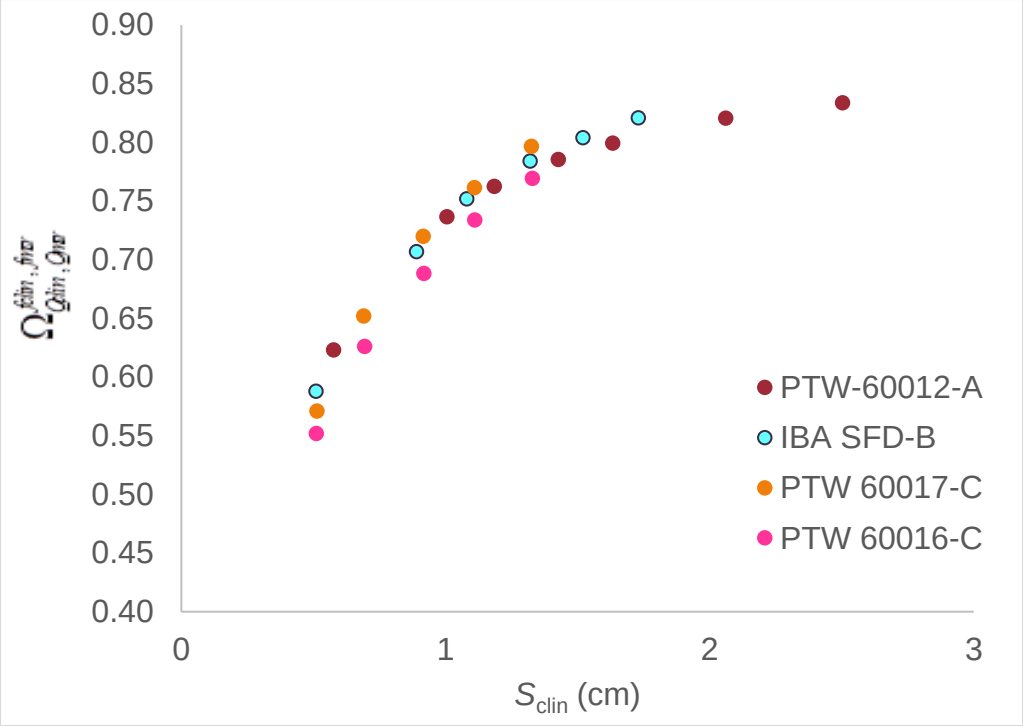


Figure 7.9 Data for FOF versus equivalent square field measurements obtained from data using diode detectors (PTW 60012, PTW 60017, PTW 60016 and IBA SFD) when the field is defined with Brainlab demountable cones at centres A, B and C. Depth of measurements was 10 cm and 6 MV energy was used by all centres. All data were normalised at 10 x 10 cm^2 field size.

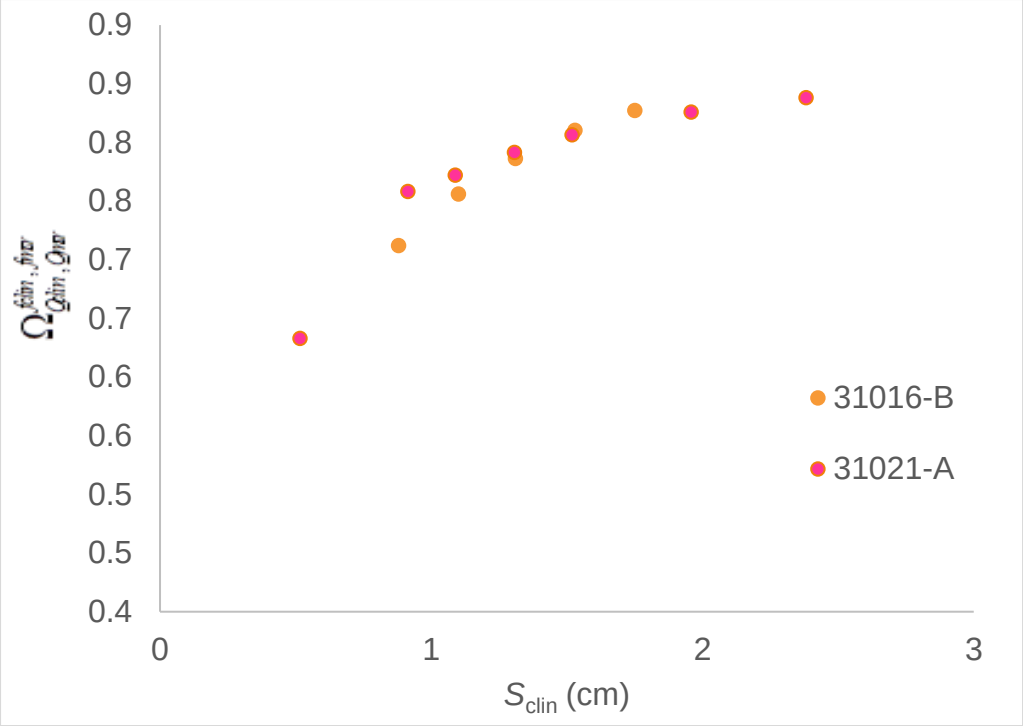


Figure 7.10 Data for FOF versus S_{clin} obtained from data using ionisation chambers when the field is defined with Brainlab demountable cones at centres A and B. The depth of measurements was 10 cm and 6 MV was used by all centres. All data were normalised at 10 x 10 cm^2 field size.

Centre C also performed measurements at depth 5 cm and their data compared to centre A data are shown in figure 7.11. A two tailed t-test assuming unequal variances was used to determine whether there was a significant difference in the data. All the p-values were more than 0.05 implying the difference was not significant. The variation in the data for the cone with diameters 1.5 cm, 1.25 cm and 1.0 cm is about 1.9 %, 1.7 % and 2 %. This variation is within the uncertainty of measurement for FOF measured using a PTW 31016 which are > 2 % for the associated S_{clin}.

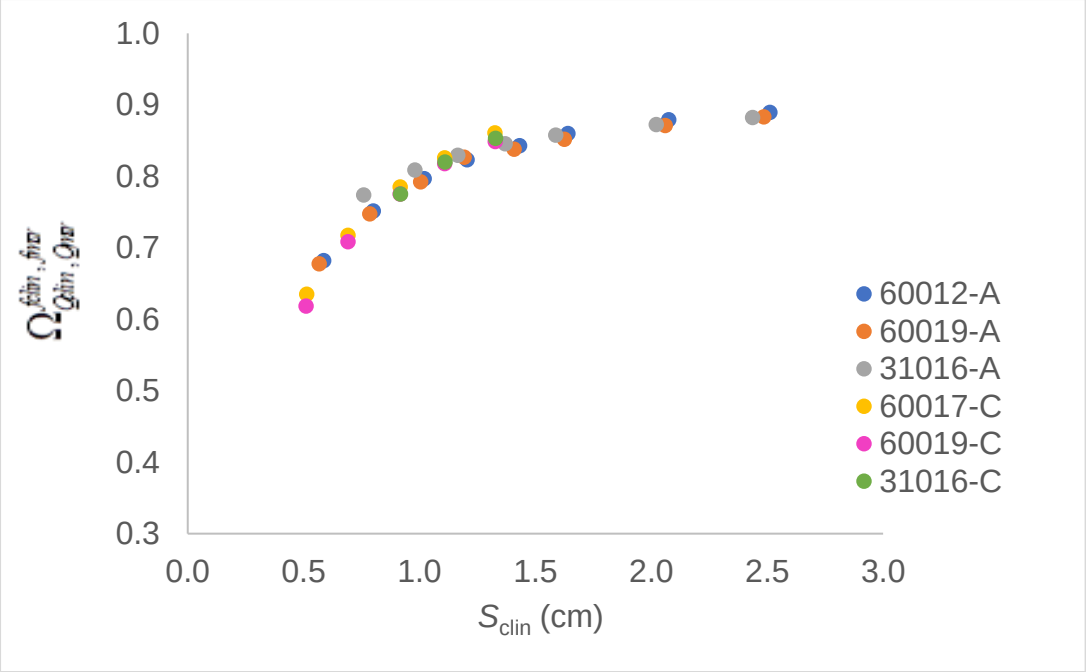


Figure 7.11 FOF versus S_{clin} obtained from data using various PTW detectors when the field is defined with Brainlab demountable cones at centres A and C. The depth of measurements was 5 cm.

7.3.5 Variation of the field output factors with detectors in a Co-60 beam

Data for the FOFs using a Co-60 teletherapy beam were determined using PTW 31006, PTW 31016, PTW 31010, PTW 60012 and PTW 60019 detectors. The variation in the FOFs using these detectors was ≤ 1.1 % for all the fields except for the S_{clin} of 0.8 cm where it was about 7.5 %. If the data from the PTW 31010, PTW 31006 and PTW 31016 detectors are eliminated in accordance with the manufacturer's recommendations, the variation of the FOF at the S_{clin} of 0.8 cm decreases to 0.7 %, which is within the measurement uncertainty for FOF. The recommendation from the manufacturer is to use these detectors in field sizes ≥ 2 x 2 cm^2. This is based on the validity of Bragg-Gray cavity theory in minimising the fluence perturbation (Andreo, 2017). Also, volume averaging is expected at these field sizes (Wuerfel, 2013). The IAEA TRS 483 recommended that measurements should be restricted to beams of radii of at least r_{LCPE} plus half the size of the external volume of the detector (IAEA, 2017), and the PTW 31010, PTW 31006 and PTW 31016 do meet this criteria for use in S_{clin} of 0.8 cm. The variation observed can therefore be attributed to the size and

perturbation of the detectors. The data obtained prove that they require a FOCF. It was then concluded that the PTW 31010, PTW 31006 and PTW 31016 detectors should not be used for S_{clin} < 2 cm, without a FOCF.

Comparing FOF Co-60 data that were measured with the BJR 25 (BJR-25, 1996) data, the BJR 25 data were higher than that measured by about 5 % at S_{clin} = 6 cm and increases to about 8 % for S_{clin} = 4 cm. This is higher than the uncertainty of measurements for FOF in those S_{clin}. Data from BJR were measured down to the field size of 4 cm and then extrapolated to 0 cm (BJR-25, 1996). The data shown for 0 cm > S_{clin} < 4 cm were extrapolated in this study. From this observation it can be concluded that the BJR 25 data should not be used for field sizes ≤ 4 cm and new data need to be determined experimentally. These data, in line with the recommendations made by Followill et. al., could be used by the centres to verify their measured FOF data and should not be used as the golden data due to the nuances in machine heads that may affect the FOF measured (Followill, 2012).

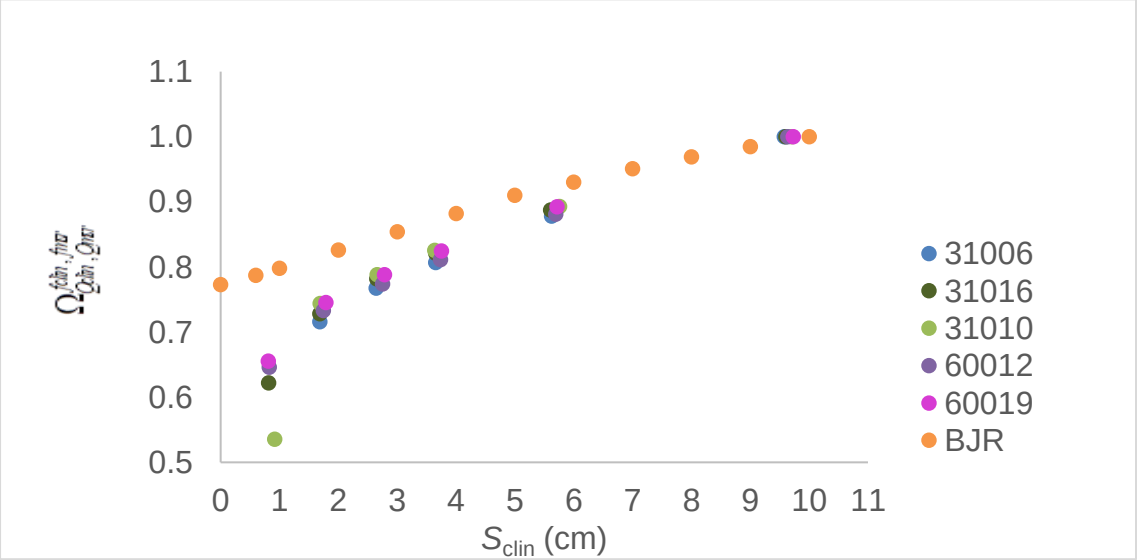


Figure 7.12 FOF versus S_{clin} measured using various PTW detectors in a Co-60 beam. No FOCFs were applied. BJR-25 data were also plotted (BJR-25, 1996).

7.3.6 Variation of equivalent square field size, S_{clin}, with MLC movement and calibration and its effect on field output factor

Figure 7.13 shows the FOFs versus S_{clin} measured using a PTW 60012 detector over a period of 333 days on 11 different days during which MLC calibrations were performed at least every three months. Measurements were performed in a 6 MV beam. These data show that there was some variation even though data were measured using the same detector. The variation in the S_{clin} was at most 0.1 cm for all field sizes, which did not yield any significant variation in the FOFs except for the equivalent square field sizes ≤ 1.8 cm. The variation observed for the S_{clin} of 1.8 cm, 0.8 cm and 0.6 cm were 0.01 cm, 0.04 cm and 0.04 cm respectively. The uncertainty of measurement for the determination of S_{clin} was estimated to be 0.06 cm indicating that the variation was within the uncertainties estimated.

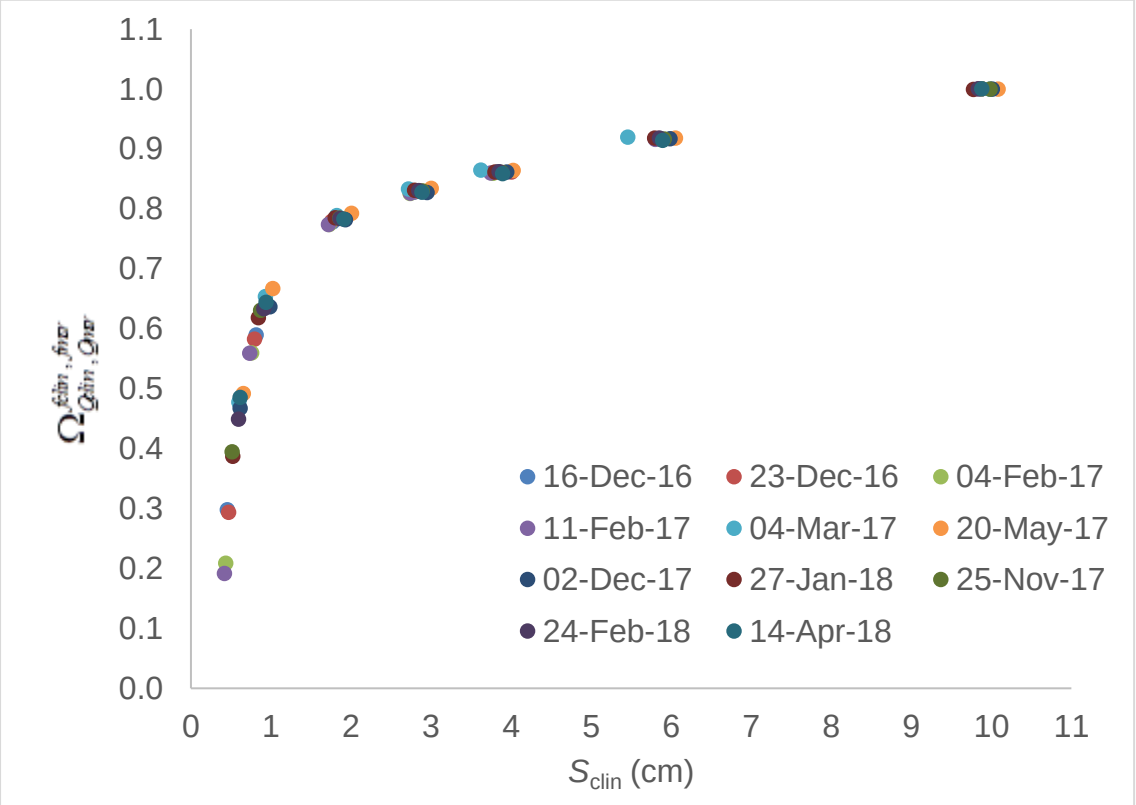


Figure 7.13 FOFs versus equivalent square field measured using a PTW 60012 detector over a period of 333 days on 11 different days. MLC calibrations were performed at least every three months. The data were for a 6 MV beam.

Figure 7.14 shows the variation of the FOF versus equivalent square field measured using various detectors over a period of 117 days on 6 different days during which MLC calibrations were performed at least every three months when only the S_{clin} measured using a PTW 60012 detector was used. These data eliminate the uncertainty contributed by using various detectors to measure the field size. Focusing on the $S_{clin} \leq 2.8$ cm, the data show that the variation is within the estimated uncertainty of measurements for the S_{clin} and is ≤ 0.04 cm. The estimated uncertainty for the determination of S_{clin} was 0.06 cm. This S_{clin} variation results in the FOFs varying by about 9 % for the smallest S_{clin} of about 0.6 cm. The uncertainty in the determination of the FOF was estimated to be 1.7 %.

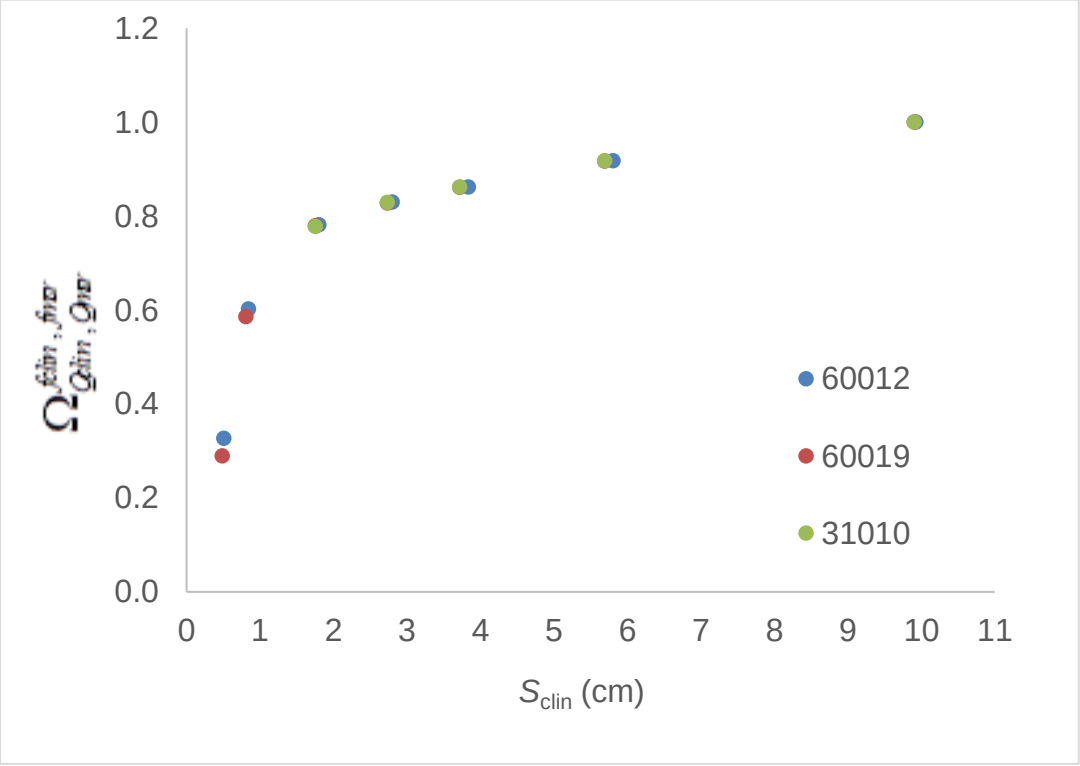


Figure 7.14 FOF versus equivalent square field measured using various PTW detectors over a period of 117 days on 6 different days during which MLC calibrations were performed at least every three months. The equivalent square field data were obtained from the measurement with the PTW 60012 detector. Data were for a 6 MV beam.

Figure 7.15 shows the variation of the FOFs versus equivalent square field measured using a PTW 60012 detector over a period of 57 days over four different days. These measurements were performed within the calibration period of the MLCs. The S_{clin} varied from 0.02 cm to about 0.04 cm with the highest observed variation at S_{clin} of 0.8 cm and 4 cm. The S_{clin} variation is within the estimated uncertainty of measurements for the field size determination, which is 0.06 cm. The FOF values calculated varied by less than 0.4 % for all equivalent square field sizes except for 0.8 cm and 0.4 cm where they varied by 3 % and 22 % respectively. MLCs were calibrated in November 2016 and two sets of data were measured in December 2016 and another two in February 2017. Comparing the FOFs that were measured in December and those measured in February the variation was about 5 % and 50 % for the S_{clin} of 0.8 cm and 0.4 cm respectively. The student t-test performed on the FOF data obtained also showed that the data set obtained in December compared with February were significantly different as the P values were less than 0.05. The uncertainty of measurements for determining the FOFs using the PTW 60012 detector was estimated to be 1.7 %. The variation observed is not acceptable as it is higher than the estimated uncertainty. This variation is attributed to the performance of the MLC and jaw, to be able to create the exact same field size each time they are programmed, especially closer to the recalibration period. The impact of this is that the field size used will not be what is anticipated and therefore, a limit should be imposed on the minimum field size that is used for complex treatment deliveries. Alternatively, more periodic MLC calibrations should be performed.

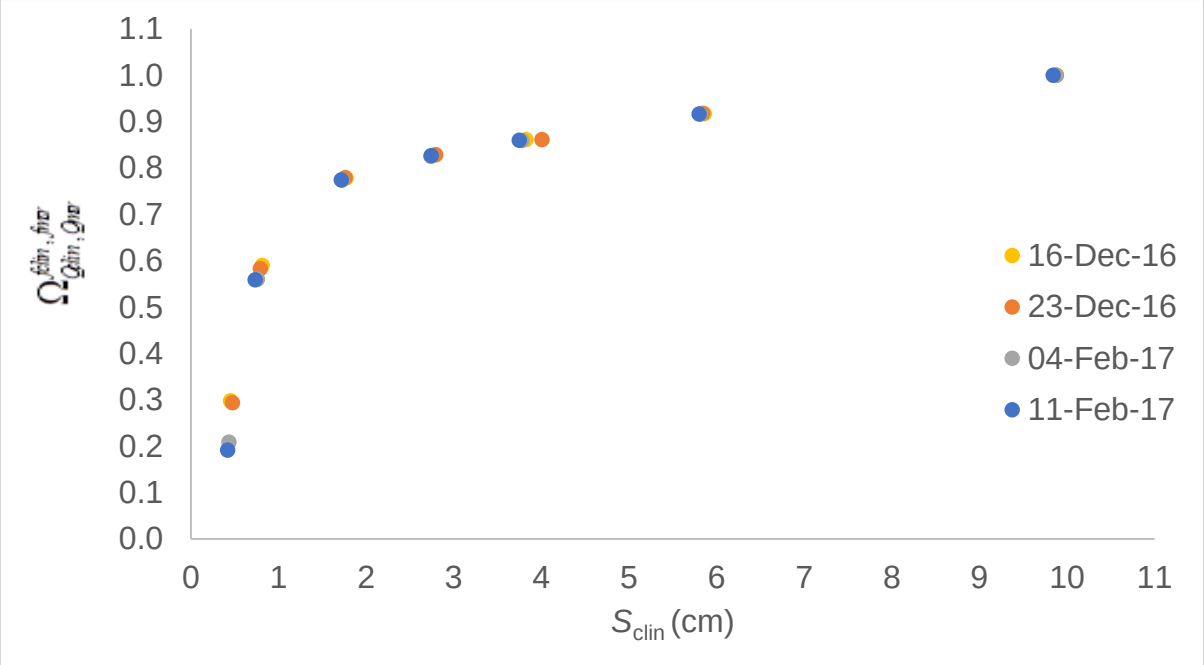


Figure 7.15 The variation of the FOFs versus equivalent square field measured using a PTW 60012 detector over a period of 57 days over four different days. There was no MLC calibration during this period.

Figure 7.16 shows the plot of the standard deviation of the mean versus S_{clin} for the FOF data and the equivalent square field data that were measured over a period of 294 days, during which there was one MLC calibration, and the measurements were repeated on three different days. The data were measured using a PTW 60019 detector. The variation of S_{clin} observed at the equivalent square fields of about 0.9 cm and 0.6 cm was 0.02 cm and 0.04 cm respectively and their corresponding FOFs varying by about 1 % and 6 % respectively. The rest of the equivalent square field variations were between 1 % and 2 % with their associated FOFs varying by ≤ 0.1 %. The uncertainty of measurements for determining the FOFs using the PTW 60019 detector is estimated to be 1.7 % for S_{clin} of 0.6 cm. This implies that the variation observed at this S_{clin} is significant and need to be taken into consideration when comparing the baseline data with data measured on any other day. The measurement repeatability is affected by the performance of the MLC and jaw, to be able to create the exact same field size each time they are programmed. These data also show the importance of having the MLCs calibrated frequently. The variations observed contribute to the uncertainty of measurement for the determination of the FOF. A limit should be imposed on the minimum field size that is used for complex treatment

deliveries in a centre. Alternatively, more periodic MLC calibrations should be performed.

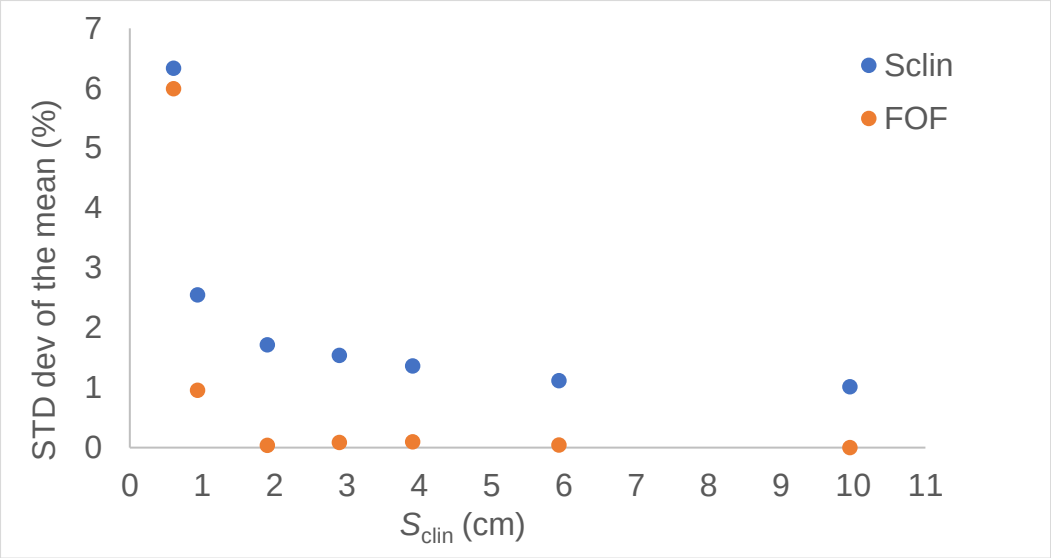


Figure 7.16 The standard deviation of the mean versus S_{clin} for the FOF and equivalent square field data that were measured over a period of 294 days during which there was one MLC calibration. The data were measured using a PTW 60019 detector.

Figures 7.17, 7.18 and 7.19 show plots of the standard deviation of the mean versus S_{clin} for the FOF and equivalent square field data that were measured over a period during which MLC calibrations were performed at least every three months, using different detectors. Measurements performed using a PTW 60012 detector were obtained over a period of 333 days on 11 different days. Those measured using a PTW 31021 detector were obtained over 329 days on 3 different days and those measured using a PTW 31018 detector obtained over 399 days on 4 different days. From the data, it was observed that the percentage variation in the FOFs consistently increased with the decrease in S_{clin} and the variation was more pronounced at $S_{clin} \leq 1$ cm.

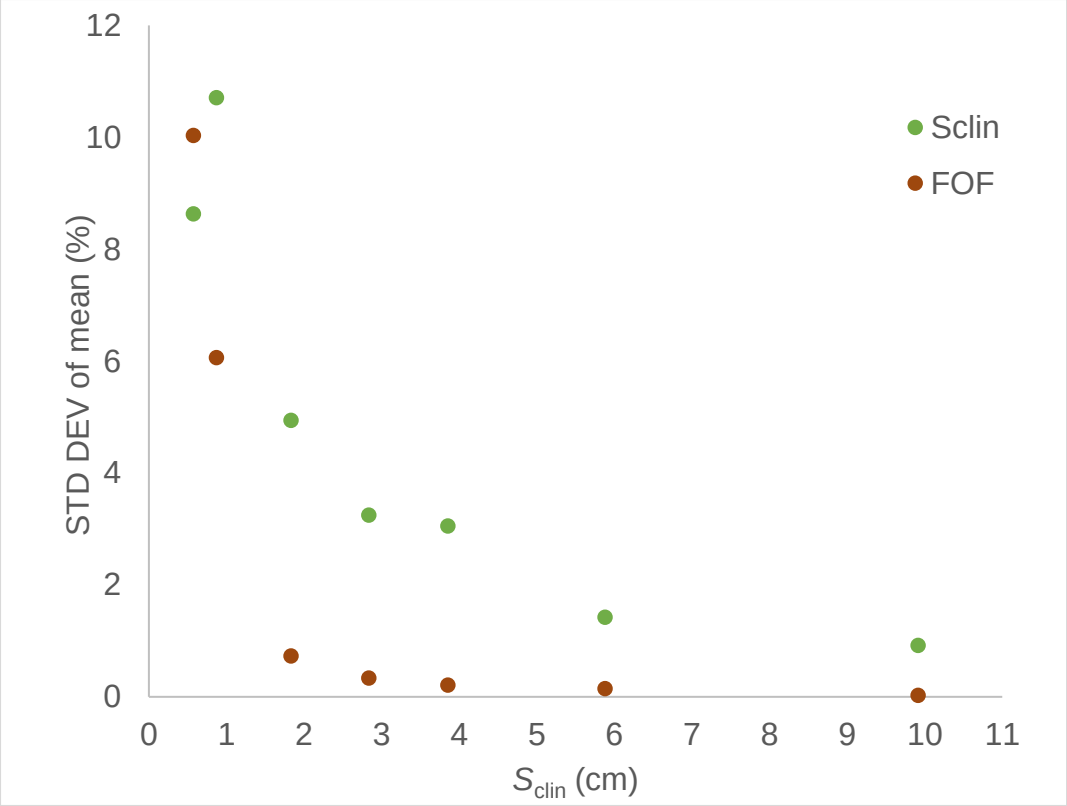


Figure 7.17 The plot of the standard deviation of the mean versus S_{clin} for the FOF and equivalent square field data that were measured over a period of 333 days on 11 different days during which MLC calibrations were performed at least every three months. The data were measured using a PTW 60012 detector.

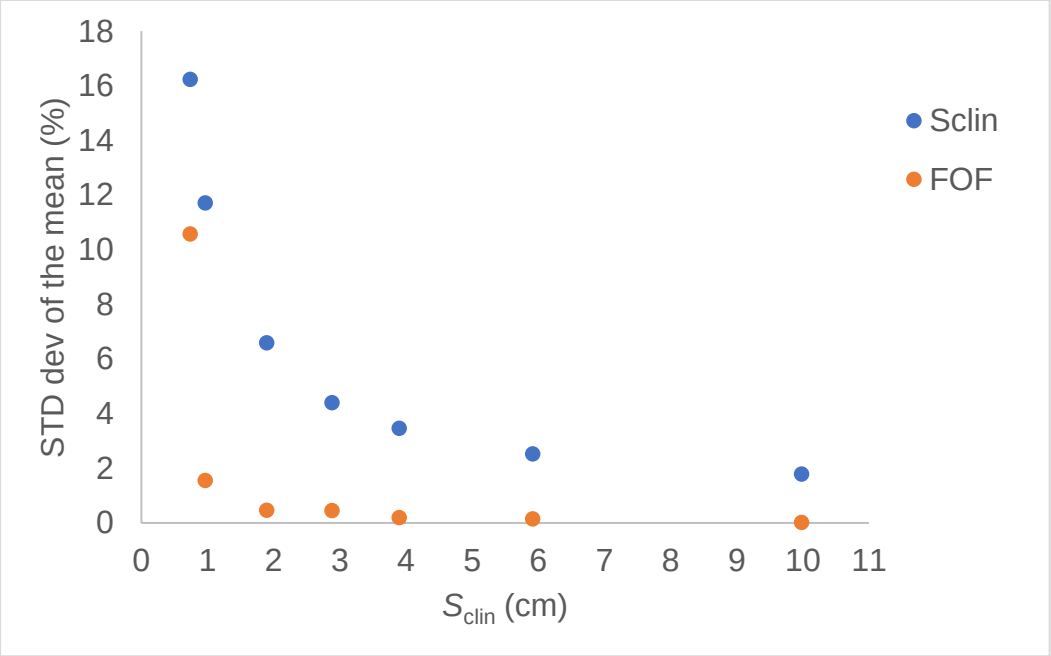


Figure 7.18 The plot of the standard deviation of the mean versus S_{clin} for the FOF and equivalent square field data that were measured over a period of 329 days on 3 different days during which MLC calibrations were performed at least every three months. The data were measured using a PTW 31021 detector.

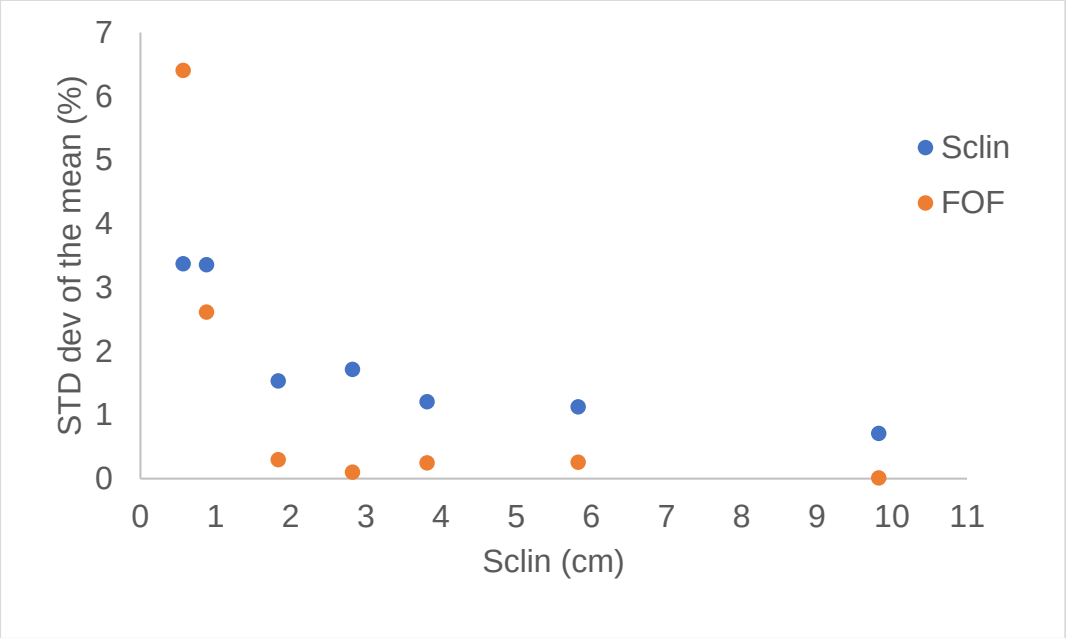


Figure 7.19 The plot of the standard deviation of the mean versus S_{clin} for the FOF and equivalent square field data that were measured over a period of 399 days on 4 different days during which MLC calibrations were performed at least every three months. The data were measured using a PTW 31018 detector.

Data in this section showed that MLC calibration should be monitored between the machine services because it could affect the FOF measurements. It also showed that FOF data for S_{clin} ≤ 1 cm must be monitored and verified between and after the MLC calibrations as the results showed significant variations.

7.3.7 Variation of equivalent square field size, S_{clin}, and the field output factor measurements with induced gantry and collimator errors

Data collected when the gantry rotation errors were introduced showed the highest variation in S_{clin} of about 4 % for gantry angle at 1.5º when using a PTW 60012 detector. All other variations were ≤ 3 %. This translates into a variation in the FOF of 2 %. The highest variation in FOF was about 5 % for a gantry angle of 1.5º when measured using a PTW 31018 detector. The highest variation in the FOF was observed for the S_{clin} of 0.6 cm and at a gantry angle of 5º, the percentage difference

was about 4 % when measured using a PTW 31018 detector. For the gantry angle of 5^{o} and for the smallest S_{clin} of 0.6 cm the highest variation was determined using a PTW 31018 detector and observed to be about 4 %.

For data collected whilst varying the collimator angle, the highest variation in the determination of S_{clin} was about 5 % for S_{clin} of 0.6 cm, when using a PTW 31018 detector which translates into a variation of about 4 % in the FOF. When using a PTW 60019 detector the difference in the FOF data for the smallest S_{clin} is 4 % for the collimator angles of 1.5^{o} and 2^{o} and 3 % for collimator angle of 5^{o}.

The difference in the CAX when a combination of gantry and collimator errors were introduced was 0.1 mm for the in plane measurements for detectors PTW 60019 and PTW 31018. For cross plane measurements, the difference increased to 0.4 mm for the PTW 60019 detector data whereas for the PTW 31018 detector the highest variation was 0.3 mm. Tables 7.9 and 7.10 shows this cross plane CAX data. The cross plane is collimated by the MLC and the in plane by conventional jaws. This is likely to be the reason why the variation in CAX in the cross plane is more than it is for the in plane. Because of the dose gradients in small fields, these errors could prevent the delivery of the intended dose if not corrected. The data obtained show how critical it is to verify the mechanical gantry and collimator settings to ensure the accuracy of the data collected or dose delivered.

Table 7.9 Difference in the cross plane CAX determined when performing lateral beam profile measurements with the gantry at 0° and collimator at 0° compared with those when mixed gantry and collimator errors were introduced using a PTW 60019 detector.

Cross plane CAX variation (mm)						
Set FS (cm^2)	S_{clin}	Gantry 0.5° Col 5°	Gantry 1.5° Col 5°	Gantry 5° Col 5°	Gantry 5° Col 1.5°	Gantry 5° Col 0.5°
6 x 6	5.8	0.0	0.1	0.4	0.4	0.4
4 x 4	3.8	0.0	0.1	0.3	0.3	0.3
3 x 3	2.8	0.0	0.1	0.3	0.3	0.3
2 x 2	1.8	0.1	0	0.2	0.3	0.3
1 x 1	0.9	0.1	0	0.2	0.2	0.2
0.6 x 0.6	0.6	0.0	0.1	0.3	0.3	0.3

Table 7.10 Difference in the cross plane CAX determined when performing lateral beam profile measurements with the gantry at 0° and collimator at 0° compared with those when mixed gantry and collimator errors were introduced using a PTW 31018 detector.

Cross plane CAX difference (mm)						
Set FS (cm^2)	S_{clin}	Gantry 0.5° Col 5°	Gantry 1.5° Col 5°	Gantry 5° Col 5°	Gantry 5° Col 1.5°	Gantry 5° Col 0.5°
6 x 6	6.0	0.0	0.1	0.1	0.1	0.1
4 x 4	3.8	0.0	0.1	0.3	0.3	0.3
3 x 3	2.8	0.0	0.1	0.3	0.3	0.3
2 x 2	1.8	0.1	0.1	0.3	0.3	0.3
1 x 1	0.9	0.0	0.1	0.3	0.3	0.3
0.6 x 0.6	0.6	0.0	0.1	0.2	0.2	0.2

7.3.8 Variation of the determination of field size and field output factor with the orientation of a detector

Figure 7.20 shows averaged FOF data obtained when ionisation chambers were oriented parallel and perpendicular to the beam plotted against S_{clin}. Data for the PTW 31016 detector were collected over a period of 28 days, data for PTW 31018 detector collected over a period of 7 days and data for the PTW 31021 detector were collected over a period of 196 days. The variations were determined from data performed on the same day for a specific chamber. The field size measurements were performed with the chamber oriented parallel to the beam for all the measurements. There was no movement of the water tank and the variations were only caused by the changes in the detector orientation and positioning. As can be visually seen, in figure 7.20 the data for the PTW 31016 detector starts showing variation at S_{clin} of 0.8 cm, for the PTW 31018 detector shows variations from S_{clin} of 2 cm whereas the data obtained using a PTW 31021 detector agreed with each other.

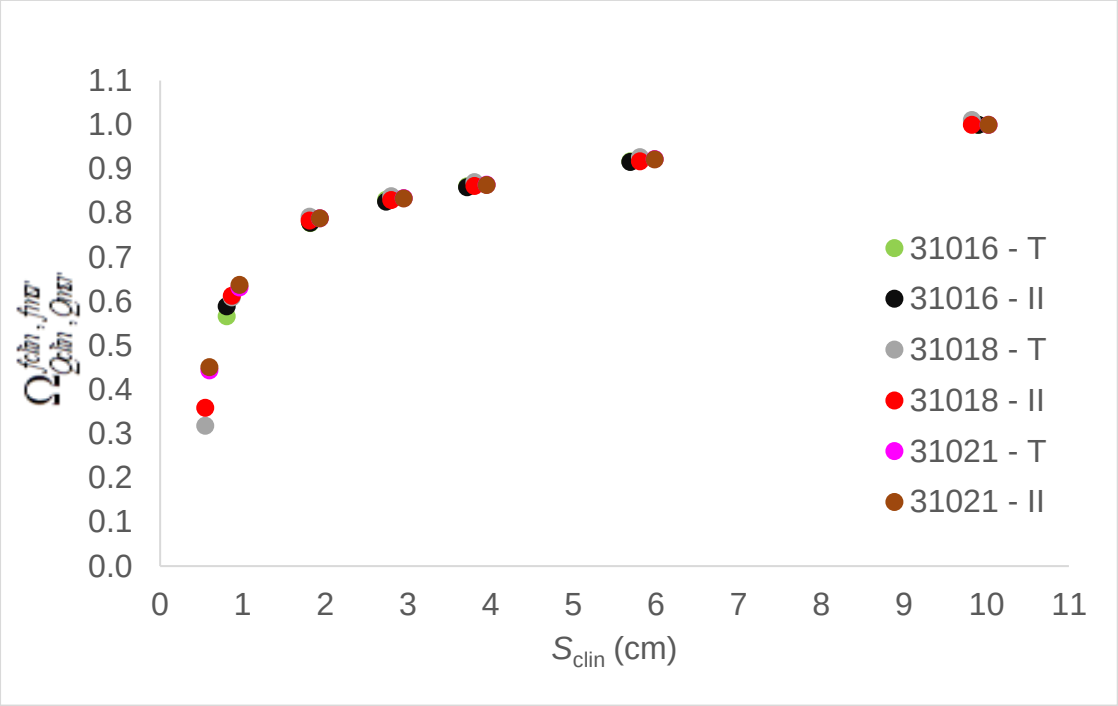


Figure 7.20 Averaged FOF data obtained when ionisation chambers were oriented parallel and perpendicular to the beam. Data for the PTW 31016 detector were collected over a period of 28 days on three different days, data for the PTW 31018 detector were collected over a period of 7 days on two different days and data for the PTW 31021 detector were collected over a period of 196 days on three different days. T represents data when the ionisation chamber was oriented perpendicular to the beam and II represents data when the ionisation chamber was oriented parallel to the beam.

Figure 7.21 shows the FOF data plotted against S_{clin} obtained using a PTW 31016 detector. The field size measurements were performed using a PTW 60012 oriented parallel to the beam. The data set were measured in a period of 28 days and there was an MLC calibration between data set 2 and 3. The difference in the FOFs calculated as a standard deviation of the mean for each day was the highest at S_{clin} of 1 cm where it was about 2 %. This difference is within the measurement uncertainty for determining the FOF when using a PTW 31016 which was estimated to be 2.3 %.

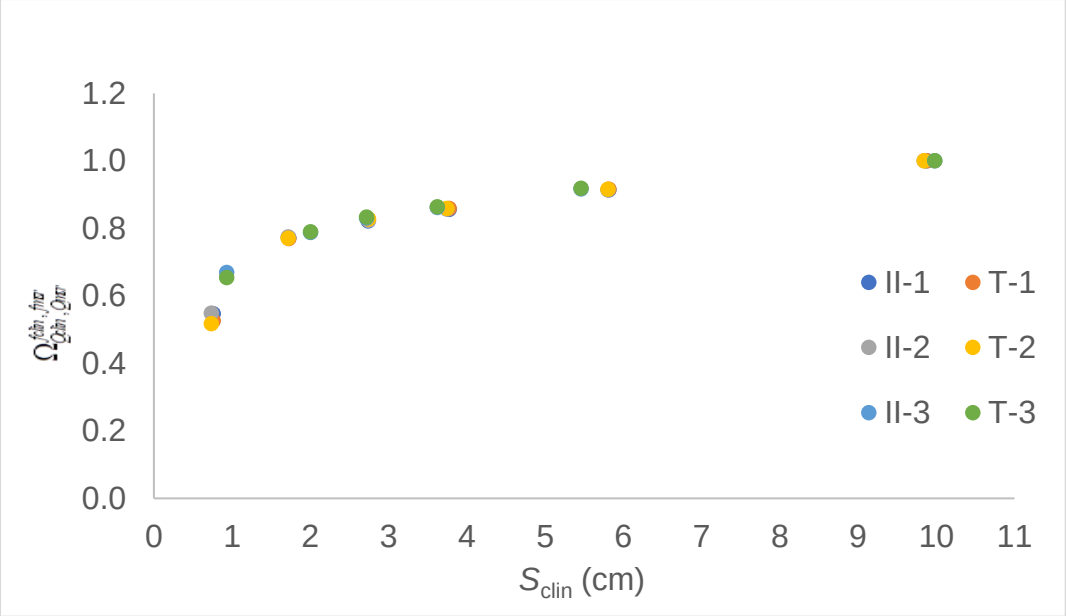


Figure 7.21 FOF versus S_{clin} obtained using a PTW 31016 detector oriented parallel and perpendicular to the beam in a 6 MV beam. T represents data when the ionisation chamber was oriented perpendicular to the beam and II represents data when the ionisation chamber was oriented parallel to the beam. The data set were measured in a period of 28 days and there was an MLC calibration between data 2 and 3.

Figure 7.22 shows the FOF data plotted against S_{clin} obtained using a PTW 31018 detector. The field size measurements were performed with the chamber oriented parallel to the beam. The difference in the FOFs calculated as a standard deviation of the mean for each day was the highest at S_{clin} of about 0.5 cm where it was about 12 % and about 3.5 % for S_{clin} of 0.8 cm. The data collected using the PTW 31018 detector were collected within a calibration period of the MLC, over seven days on two different days. The differences in the FOFs are higher than the estimated uncertainties for this detector. The manufacturer has recommended that this detector be used only in parallel to the beam. These data support the manufacturer's recommendations that the ionisation chamber is not used in a perpendicular orientation to the beam.

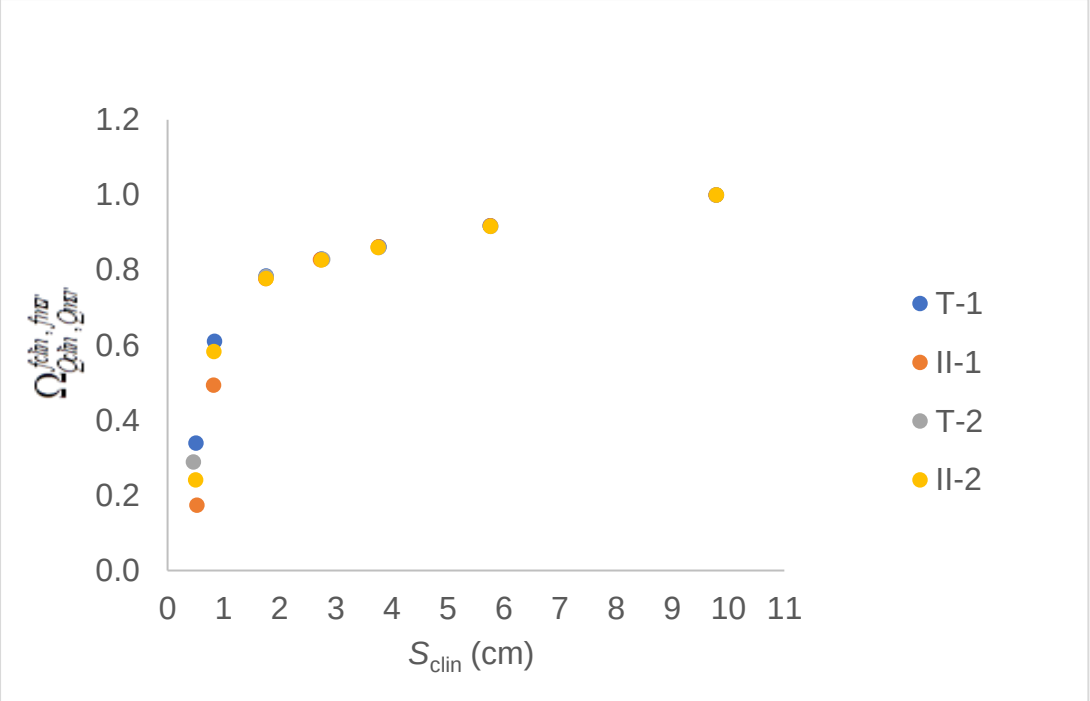


Figure 7.22 FOF versus S_{clin} obtained using a PTW 31018 detector oriented parallel and perpendicular to the beam in a 6 MV beam. T represents data when the ionisation chamber was oriented perpendicular to the beam and II represents data when the ionisation chamber was oriented parallel to the beam. The data set 1 and 2 were measured seven days apart.

The data obtained using an ionisation chamber, PTW 31021, are shown in figure 7.23 for measurements that were performed over a period of 196 days on three different days. Comparing the data sets for each day, one data set for the 25 November showed a variation in the FOFs of about 0.01 for the equivalent square field sizes of about 0.9 cm and 0.6 cm, which was higher than the estimated measurement uncertainty. The other data sets showed variations that were ≤ 0.003 for all field sizes and these were within the estimated measurement uncertainties.

A student t-test performed on the FOF data obtained showed that the FOF data set obtained on 25 November 2017 compared with the rest of the FOF data were significantly different as the P values were less than 0.05. The FOF data sets were obtained three days after MLC calibration except for the FOF data collected on the 25 November 2017 which were collected 94 days after MLC calibration. Data for S_{clin} were

not significantly different except for the equivalent square field of 1 cm, where the data obtained on 25 November 2017 were significantly different. The S_{clin} data were higher on initial data then decreased after 196 days between MLC calibration. It then increased again after MLC calibration. The student t-test performed on the FOF data obtained also showed that the data set obtained on 17 May 2017 compared with the rest of the data were significantly different as the P values were less than 0.05. The days between the measurement dates for data set obtained on 17 May 2017 and the other two sets were 189 days and 196 days. The number of days between the other data sets were seven.

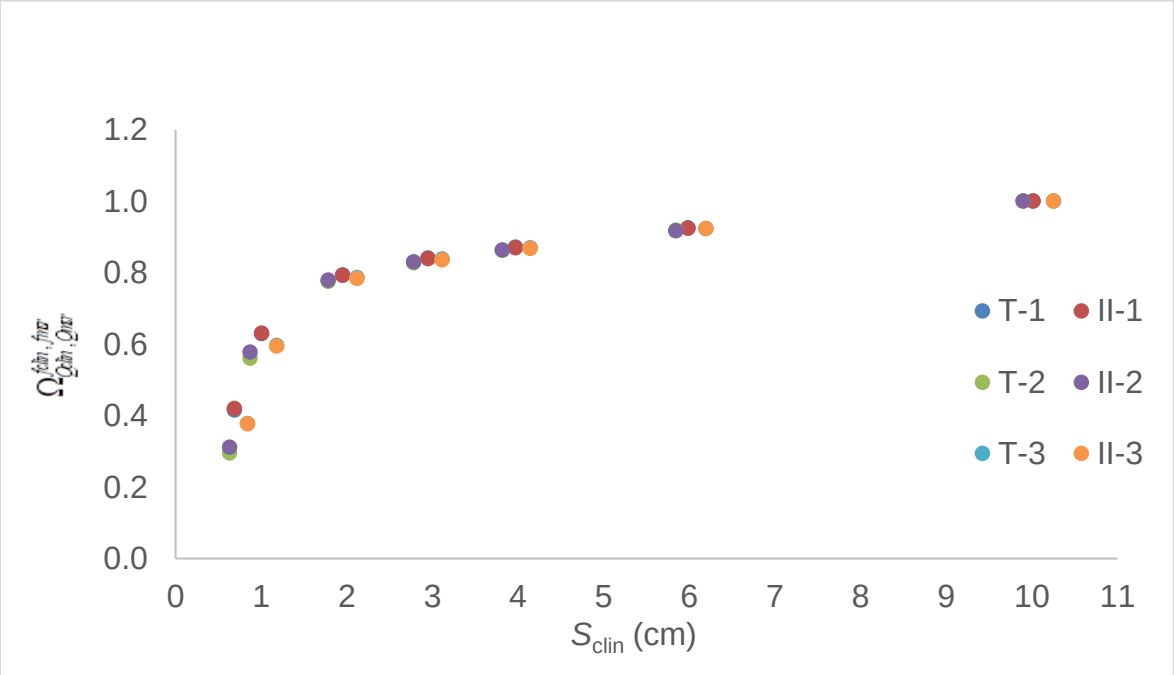


Figure 7.23 FOF versus S_{clin} obtained using a PTW 31021 detector oriented perpendicular and parallel to the beam. The data shown were collected over a period of 196 days. T represents data when the ionisation chamber was oriented perpendicular to the beam and II represents data when the ionisation chamber was oriented parallel to the beam.

The PTW 31021 detector was also used to check the variation caused by the orientation of a detector in measuring the field size and FOFs when the orientation of the detector is the same when performing both measurements. Figure 7.24 shows the results obtained. On average the field size difference was about 0.4 cm for the set field

size of 2 x 2 cm^2 increasing to about 2 cm for the set field size of 0.6 x 0.6 cm^2. This corresponds to a difference of 0.2 % for the FOFs measured at set field size of 2 x 2 cm^2 increasing to 1.7 % for the FOFs measured at set field size of 0.6 x 0.6 cm^2. From the data presented in figure 7.24 the differences are within the estimated uncertainty of measurements for the determination of the FOFs when using the PTW 31021 detector. Data shown in figures 7.20 to 7.24 lead to a conclusion that the PTW 31016 and PTW 31021 detectors are better suited to be used in both orientations better than the PTW 31018 detector down to the S_{clin} of 1 cm and 0.6 cm for PTW 31016 and PTW 31021 respectively. But the preferred orientation was the one where the detector was positioned parallel to the beam due to the ease of that set up. Volume averaging is dependent on the detector size. For a detector that has similar cavity dimensions radially and longitudinally like the PTW 31016 and PTW 31021, it is expected that the response of these detectors will be the same regardless of the orientation (IAEA, 2017 and Casar, 2020).

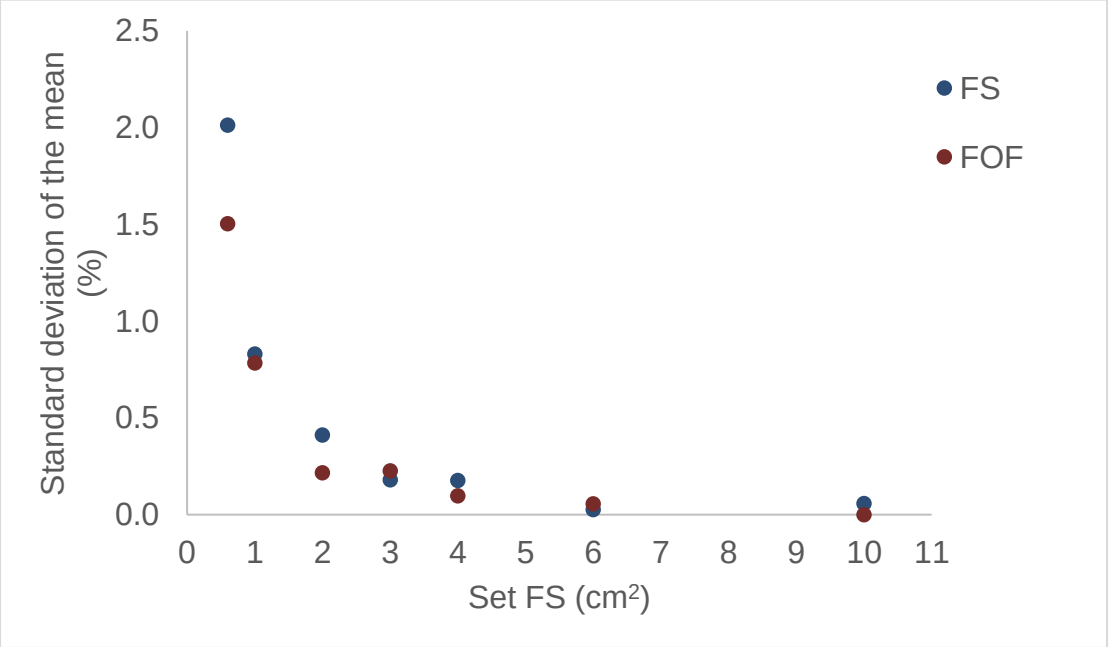


Figure 7.24 Standard deviation of the mean versus set field size for measurements using a PTW 31021 ionisation chamber when the orientation of the detector is the same when measuring field size and when measuring FOFs. The measurements were performed over a period of 196 days but those compared for perpendicular and parallel were performed on the same say. Measurements were performed in a 6 MV photon beam.

7.4 Measurements with and without a reference detector

Percentage depth dose measurements performed with and without a reference detector, PTW 34091, were compared. Figures 7.25 shows data measured with and without a PTW 34091 for a 0.6 x 0.6 cm^2 field. Figure 7.26 shows the results for a set field size of 1 x 1 cm^2. The detector used for performing the measurements was a PTW 60012 detector.

A method suggested by Low et.al. (1998) was used to determine the comparability of the percentage depth dose curves. This method determines the gamma index when comparing the percentage depth dose curves calculating the dose-difference and distance-to-agreement (DTA) for the curves being compared. For comparing the percentage depth dose curves, a gamma was calculated using a dose tolerance of 0.9 % and a DTA of 0.1 mm for set field sizes of 0.6 x 0.6 cm^2 and 1 x 1 cm^2. The pass rates were 90.2 % and 98.4 %. For an acceptable pass rate of 95.1 % for the 0.6 x 0.6 cm^2 field size, the dose tolerance was 1.1 % and a DTA 0.1 mm.

The results agree with those of L'homel et. al. (L'homel, 2017), who found that when the PTW T-Ref detector is placed at a distance ≥ 20 cm, there was no perturbation of the field detected and also the electrons generated on the T-Ref do not reach the detector used for performing the measurements at depth.

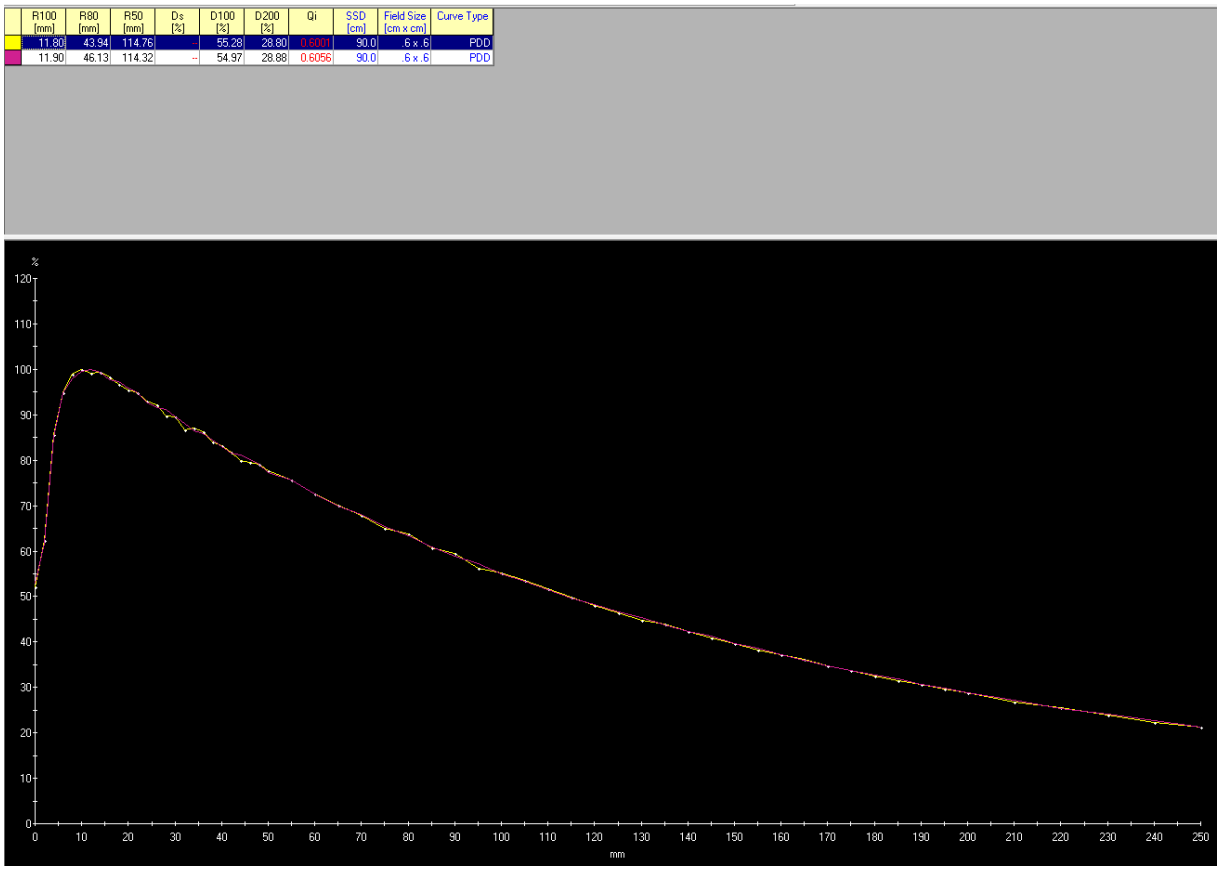


Figure 7.25 *PDD* curve for a set field size of 0.6 x 0.6 cm^2 measured with and without a reference detector, PTW 34091. Yellow represents the data that were obtained with a PTW 34091 detector in the beam and pink represents the data for measurements without a PTW 34091. Each curve was normalised to the depth of maximum dose.

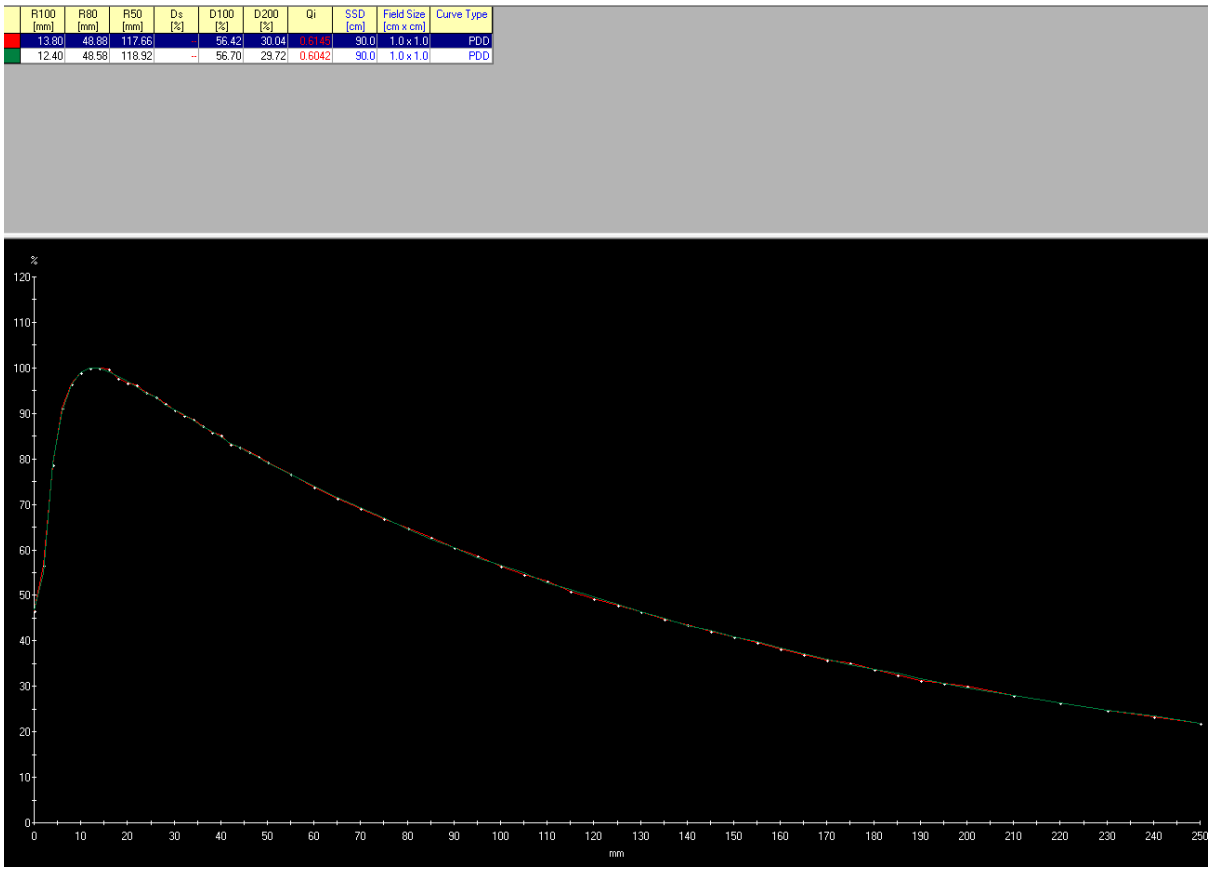


Figure 7.26 *PDD* curve for a set field size of 1 x 1 cm^2 measured with and without a reference detector, PTW 34091. Red represents the data that were obtained with a PTW 34091 detector in the beam and green represents the data for measurements without a PTW 34091 detector. Each curve was normalised to the depth of maximum dose.

Figure 7.27 shows the percentage difference in the FOF values measured with and without a T-Ref when using a PTW 31021 and a PTW 31010 detector. The difference was about 0.1 % for all equivalent square field sizes except for the two smallest fields. It increased to 0.8 % for the equivalent square field of 0.9 cm when using a PTW 31010 detector: 2 % and 3 % for the equivalent square fields of 0.9 cm and 0.7 cm respectively when using a PTW 31021 detector. The difference using both detectors is within the measurement uncertainty for all equivalent field sizes except for the measurements using a PTW 31021 detector at the equivalent square field of 0.7 cm. The uncertainty in measurements of the FOFs is given in table 7.15. The reason for the % difference that is within the uncertainty of measurements is attributed to the

stability of the dose rate/beam output. The difference that is higher than the uncertainty in the equivalent square field of 0.6 cm is due to the inability of the PTW 31021 detector to measure accurately at those small fields. For $S_{clin} \leq 1$ cm, the use of the reference chamber will provide confidence in the data measured.

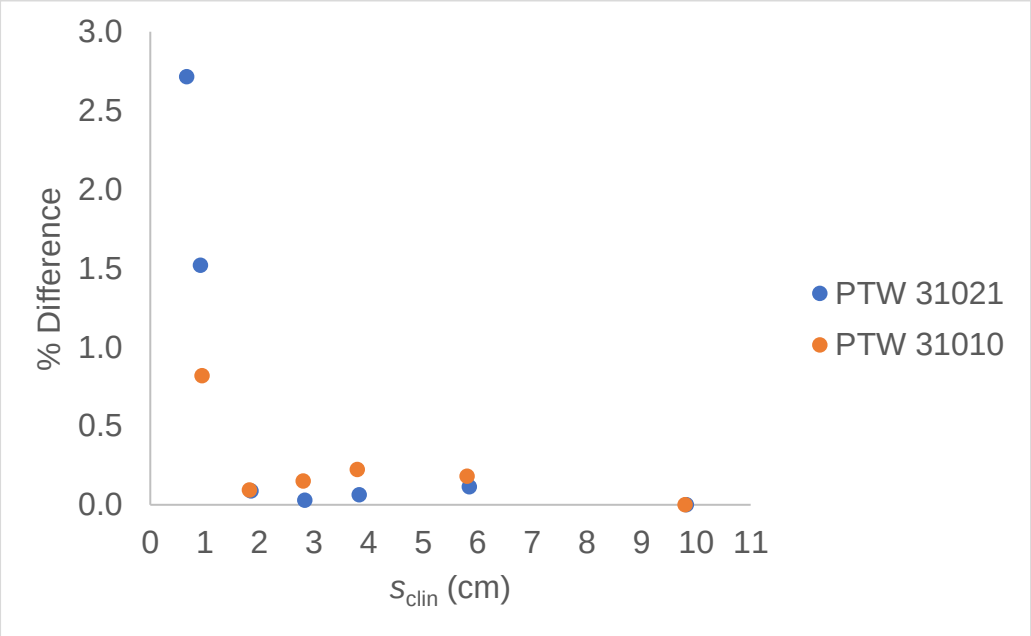


Figure 7.27 Percentage difference in the FOF values measured with and without a PTW 34091 detector when using a PTW 31021 and a PTW 31010 detector to measure FOFs.

7.5 Beam quality Indices

Data were measured using various detectors at depth 10 cm and 20 cm. The measurements using each detector were performed on same day without variations in the set up except for the setting of the detectors at different depths. The variation for the measured $TPR_{20,10}(10)$ ranged from 0.002 (0.3%) at a set field size of 10 x 10 cm^2 to about 0.004 (0.6 %) for a set field size of 3 x 3 cm^2, which is the msr field for cones, as shown in figure 7.28. The estimated uncertainty for the determination of the $TPR_{20,10}(10)$ is 0.6 % for a coverage factor of k = 2, equal to confidence level of 95 %.

$TPR_{20,10}(10)$ derived from the data measured using set field sizes 6 x 6 cm^2 and 4 x 4 cm^2 using equation 4.7 were compared with the data measured for each detector. A student t-test was used to check if there were any outliers in the calculated data. The calculated average $TPR_{20,10}(10)$ was 0.678 with a standard deviation of the mean of 0.5 %. When considering the data for each detector the highest variation observed was about 0.3 %. All these results were within the uncertainty of measurements for the determination of $TPR_{20,10}(10)$. When comparing the data obtained using the equation 3.8 with this study, the variation is more than 3 %. This is much higher than the uncertainty of measurements. The 3 % variation in the $TPR_{20,10}(10)$ for a PTW 30013 detector in a beam of $TPR_{20,10}(10) = 0.67$ yields a k_Q factor that is 0.3 % different when using the data published in the IAEA TRS 398 (IAEA, 2000). And thus equation 3.8 is not recommended for use in estimating the $TPR_{20,10}(10)$ for small fields as it will cause an increase in the uncertainty for absorbed dose to water.

Equation 4.7 may be used for the machines that cannot establish the reference field 10 x 10 cm^2 to calculate $TPR_{20,10}(10)$ with an estimated uncertainty of about 1 % for a coverage factor of $k = 2$, equal to confidence level of 95 %. These data show that equation 4.7 may be used for an equivalent square field size of 3 cm.

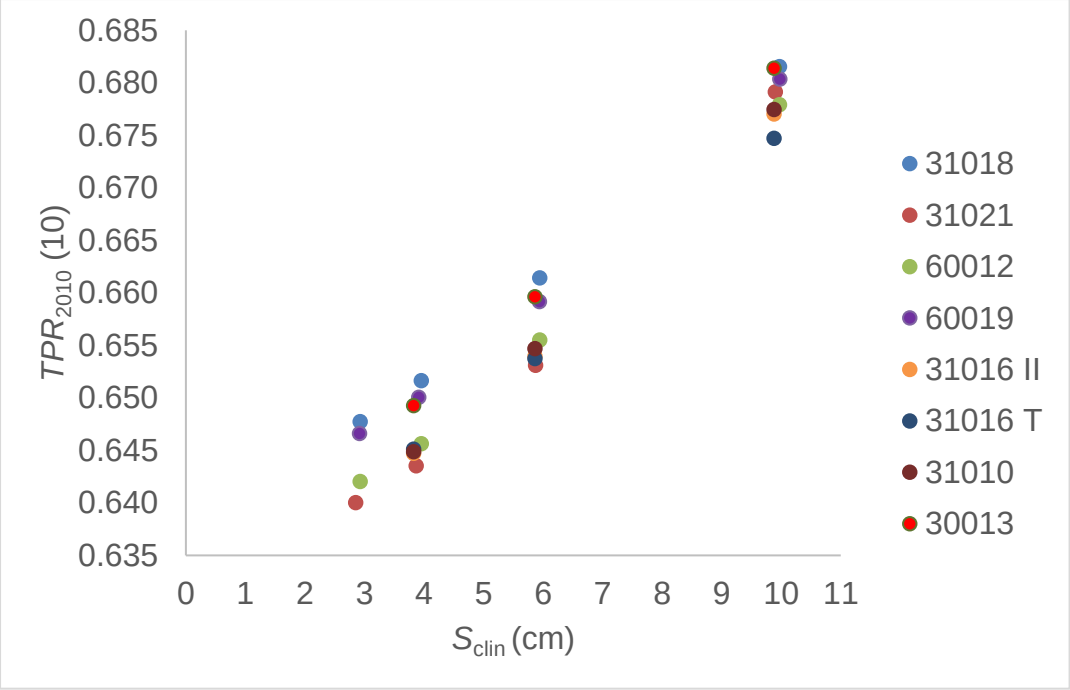


Figure 7.28 $TPR_{20,10}(10)$ measured in a 6 MV beam using various PTW detectors over a period of two years with MLC calibration periodically. 31016 II refers to the detector positioned parallel to the beam and 31016 T, to the detector positioned parallel to the beam.

7.6 Traceability of measurements

The detectors were cross calibrated at 6 MV for set field sizes of 10 x 10 cm^2, 6 x 6 cm^2 and 4 x 4 cm^2. The variations in the calibration coefficient obtained at field sizes 6 x 6 cm^2 and 4 x 4 cm^2 compared with data from 10 x 10 cm^2 were ≤ 0.02 % for field size of 6 x 6 cm^2 and about 2 % for the field size of 4 x 4 cm^2. The estimated uncertainty linked to this cross calibration was 3 % with a coverage factor of k = 2, equal to a confidence level of 95 %. Table 7.11 shows the data. Table 7.12 shows the data for similar measurements performed in a Co-60 machine. The variation for both the 6 MV and Co-60 measurements were within the uncertainty of measurements, i.e. 3 %.

Table 7.11 Calibration coefficients obtained by cross calibrating the detectors at a reference field 10 x 10 cm^2 and virtual msr fields of 6 x 6 cm^2 and 4 x 4 cm^2 in a LINAC using a 6 MV beam.

Chamber type	10 x 10 cm^2	6 x 6 cm^2	4 x 4 cm^2
PTW 31010	0.30 Gy/nC	0.30 Gy/nC	0.29 Gy/nC
PTW 31016 parallel	2.37 Gy/nC	2.37 Gy/nC	2.33 Gy/nC
PTW 31016 perpendicular	2.40 Gy/nC	2.39 Gy/nC	2.35 Gy/nC

Table 7.12 Calibration coefficients obtained by cross calibrating the detectors at a reference field 10 x 10 cm^2 and virtual msr fields of 6 x 6 cm^2 and 4 x 4 cm^2 in a Co-60 beam.

Chamber type	10 x 10 cm^2	6 x 6 cm^2	4 x 4 cm^2
PTW 31010	0.30 Gy/nC	0.30 Gy/nC	0.30 Gy/nC
PTW 31016 parallel	2.36 Gy/nC	2.35 Gy/nC	2.34 Gy/nC
PTW 31016 perpendicular	2.41 Gy/nC	2.43 Gy/nC	2.46 Gy/nC

7.7 Estimation of uncertainties

Table 7.13 shows the uncertainty contributors in the determination of the FOCF for the PTW 31021 in a 1 x 1 cm^2 field size.

Table 7.13 Uncertainty budget for the determination of the FOCF when using a PTW 31021 in a 1 x 1 cm^2 field size

Source of uncertainty	Estimated (%)	Type
uncertainty associated with the FOCF of the reference detector, u_{FOCF}(ref)	0.5	B
Uncertainty in the determination S_{clin}, $u_{S_{clin}}$	0.4	A
Uncertainties linked to the measurements performed using a reference detector in clin beam		
Positioning of chamber at beam centre	0.001	B
Uncertainty linked to the electrometer	0.1	A
Uncertainties linked to the measurements performed using a reference detector in msr beam		
Positioning of chamber at beam centre	0.000	B
Uncertainty linked to the electrometer	0.1	A
Uncertainties linked to the measurements performed using a PTW 31021 in clin beam		
Positioning of chamber at beam centre	0.001	B
Uncertainty linked to the electrometer	0.1	A
Ambient conditions measurements and correction	0.5	B
Uncertainties linked to the measurements performed using a PTW 31021 in msr beam		
Positioning of chamber at beam centre	0.0001	B
Uncertainty linked to the electrometer	0.2	A
Ambient conditions measurements and correction	0.5	B
Combined standard uncertainty (*k* = 1)	1.0	
Combined standard uncertainty (*k* = 2)	2.0	

Table 7.14 gives the uncertainty budget for the determination of the FOF when using a PTW 60012. Similar budget was determined for each detector to determine the results given in table 7.15.

Table 7.14 Uncertainty budget for the determination of the FOF when using a PTW 60012 in a 0.6 x 0.6 cm^2 field size

Source of uncertainty	Estimated (%)	Type
Field output correction factors, u_{FOCF}	0.70	B
Uncertainty in the determination S_{clin}, $u_{S_{clin}}$	0.4	A
Uncertainty linked to $u_{M_{clin}}$		
Positioning of chamber at beam centre	0.2	B
Uncertainty linked to the electrometer readings	0.1	A
Uncertainty linked to $u_{M_{msr}}$		
Positioning of chamber at beam centre	4E-07	B
Uncertainty linked to the electrometer readings	0.1	A
Combined standard uncertainty (*k* = 1)	0.84	
Combined standard uncertainty (*k* = 2)	1.7	

Table 7.15 shows the estimated combined relative uncertainty for the FOFs using the PTW detectors models 60012, 60019, 31018, 31016 and 31010 in conjunction with the FOCFs published in the IAEA TRS 483 for k = 2, equal to a confidence level of 95 %. As seen in table 7.15, the ionisation chambers give much higher uncertainties than the solid-state detectors.

Table 7.15 Combined relative uncertainty for the FOFs determined using various PTW detectors and the FOCFs published in the IAEA TRS 483 for k = 2, equal to a confidence level of 95 %.

S_{clin} (cm)	PTW 60012	PTW 60019	PTW 31018	PTW 31016	PTW 31021	PTW 31010
6 x 6	0.8	0.8	1.2	0.8	1.6	0.8
4 x 4	1.0	1.0	1.2	1.0	1.7	1.0
3 x 3	1.0	1.0	1.5	1.0	2.4	1.1
2 x 2	1.1	1.1	1.7	1.1	3.9	2.1
1 x 1	1.3	1.3	2.1	2.3	4.1	5.0
0.6 x 0.6	1.7	1.7	2.9	5.0	-	-

8. Conclusions

- It is very important to verify CAX for each independent measurement set up and not rely only on the set up using light field projections, the manufacturer's specifications of a detector and an automated water tank positioning system.
- The CAX of the radiation field needs to be established for each individual detector as the variation in CAX of 0.8 mm for in plane and 1.6 mm for cross plane could yield a 32 % variation in the FOF for an S_{clin} of about 0.6 cm.
- The solid-state detectors used in the study performed better than the air ionisation detectors in the determination of S_{clin} and FOF.
- The data in this study show that reliance on one detector for performing FOF measurements could yield undesirable outcomes. It is crucial to have more than one detector as this will help to get confirmation of the results.
- This study showed that equation 6.1, the method recommended by Sterling (Mayles, 2017), or equation 6.2, which is recommended in the IAEA TRS 483 (IAEA, 2017), may be used for calculating the equivalent square fields for small static fields with an uncertainty of 0.06 cm. Also, the FOF determined using both these methods yielded results that were within their corresponding measurement uncertainty. The method chosen should be documented to ensure that it is consistently applied.
- But further studies need to be performed for elongated fields where the length or width will be significantly larger than the other side as the data showed a difference that increased as the field gets smaller and the measured length and width differ more from each other at nominal field sizes ≤ 3 x 3 cm^2.
- Lack of periodic MLC maintenance will result in a gradual change in S_{clin}.
- The measurement repeatability of FOFs is affected by the performance of the MLC and jaw to be able to repeatedly achieve the exact same field size.
- The frequency of the MLC calibration greatly affects the FOF data. As such, a suitable frequency for each machine should be determined. From data in this study, it was concluded the 3-monthly calibration of the machines yielded results that were within 0.06 cm, which was the measurement uncertainty for the determination of S_{clin}.

- The use of a FOCF is critical for small field detectors to ensure accuracy of the dosimetry. For those detectors that do not have published FOCFs, there is a need to determine them before a detector is used for clinical measurements and have them validated through comparisons, calculations or audits.
- When using more than one detector, at least two of the detectors used for determining FOF should have published FOCFs for the radiation beams and field sizes to be used. The detectors with published FOCF may be used to determine the FOCF's for the other detectors using equation 6.5 in section 6.2.3.3, as recommended in the IAEA TRS 483 (IAEA, 2017).
- FOCFs were determined for the PTW 31021 detector, see table 7.8 of section 7.3.3, and compared with the data obtained using FOCFs published in the IAEA TRS 483. The results were within the uncertainty of measurements for this detector, as given in table 7.15 of section 7.7.
- Published FOCF are restricted to S_{clin} where the 0.7 < A/B < 1.4. Based on the sensitivity of FOF data for S_{clin} < 2 cm, a formula for calculating S_{clin} needs to be developed for elongated fields.
- The PTW 31010, PTW 31006 and PTW 31016 detectors should not be used for S_{clin} < 2 cm in a Co-60 beam without a FOCF.
- Data published in BJR 25 for 6MV and cobalt teletherapy should not be used for determining FOFs in small fields as it showed differences of about 40 % for the smallest field size.
- Some centres could not defend their FOF data owing to a lack of documentation.
- This study showed that detector orientation may be significant for small field measurements. It was concluded that the PTW 31018 should not be used perpendicular to the beam as it yielded differences of about 12 % and 3.5 % for S_{clin} of about 0.5 cm and 0.8 cm, respectively. It was also concluded that the PTW 31021 could be used in either orientation as the FOF data were within the measurement uncertainty given in table 7.15 of section 7.7 for all the field sizes. The preferred orientation may be parallel due to the ease of set up, which limits the uncertainties associated with the set up itself.

- Each centre should evaluate the stability of their beam output in order to decide on the use of a reference chamber like the T-Ref. For $S_{clin} \leq 1$ cm, the use of the reference chamber will provide confidence in the data measured.
- The study was performed using a Siemens Primus linac, which was found to have a stable beam output and the use of a T-Ref did not improve the uncertainty of measurement.
- This study showed that the method recommended in the IAEA TRS 398, for the determination of the beam quality index, should not be used for small static fields as it introduced variations of about 3 % in a beam of $TPR_{20,10}(10) = 0.67$, which were significantly higher than the measurement uncertainty.
- Equation 4.7 of section 4.4.4 may be used for the machines that cannot establish the reference field of 10 x 10 cm^2 in order to calculate $TPR_{20,10}(10)$ with an estimated uncertainty of about 1 % for a coverage factor of $k = 2$, equal to confidence level of 95 %. Data in this study show that equation 4.7 may be used down to an equivalent square field size of 3 cm with an estimated uncertainty of 1 %.
- The determination of FOFs and daisy chaining are the two dosimetric procedures resulting in the biggest uncertainties for reference dose determination.
- The relative uncertainties of measurements were estimated for the determination of the FOF data using PTW 31021, PTW 31010, PTW 31016, PTW 31018, PTW 60012 and PTW 60019 detectors. As shown in table 7.15 of section 7.7, the estimated relative uncertainties determined for the FOFs show that for the smallest equivalent square fields, 1 cm and 0.6 cm, the PTW 60012 and PTW 60019 solid-state detectors have less uncertainties compared to the other detectors.
- There is a need for PSDLs and SSDLs to provide traceability for field sizes of 4 x 4 cm^2 to decrease the uncertainty and risk associated with daisy chaining of small field detectors.
- Dosimetry audits for small fields should focus on the measured FOFs and reference dose determination in field sizes ≤ 2 cm as data from the study showed that small variations in the set up could lead to higher uncertainties in the FOF.

- The performance of MLCs' at field sizes ≤ 1 must be part of the audit as their performance could affect the FOF measurements. The data from the centre's monitoring of MLCs in between the calibration periods be evaluated if it supports the minimum field size that is used for complex treatment deliveries.

9. Future work

- FOCF data for Co-60 teletherapy with MLC is lacking.
- There is a need for PSDLs and SSDLs to develop methods for calibrating detectors used in small fields using the field size of 4 x 4 cm^2 to decrease the uncertainty due to daisy chaining of small field detectors.
- The formula used in equation 4.7 of section 4.4.4, that was suggested in the IAEA TRS 483 for calculating $TPR_{20,10}(10)$ should be more rigorously tested for field sizes ≤ 3 cm.

References

Alfonso, R. et al. (2008) A new formalism for reference dosimetry of small and nonstandard fields, Med. Phys. 35, 5179–5186.

Allisy-Roberts, P. J. and Burns, D. T. (2005) Summary of the BIPM.RI(I)-K4 comparison for absorbed dose to water in ^{60}Co gamma radiation, Metrologia, Volume 42, Technical Supplement.

Almond, P.R. et al. (1999) AAPM's TG-51 protocol for clinical reference dosimetry of high-energy photon and electron beams, Med. Phys. 26, 1847–1870.

Andreo, P., Burns, D.T. and Salvat, F. (2012) On the uncertainties of photon mass energy-absorption coefficients and their ratios for radiation dosimetry, Phys. Med. Biol. 57 2117–2136.

Andreo, P. et al. (2016) On the Monte Carlo simulation of small-field microdiamond detectors for megavoltage photon dosimetry, Phys Med Biol. 61: L1–L10.

Andreo, P. and Palmans, H. (2016) Comments on "experimental determination of the PTW 60019 microDiamond dosimeter active area and volume", Med Phys. 43:6667.

Andreo, P. et al. (2017) Fundamentals of Ionizing Radiation Dosimetry, First edition, Wiley-VCH Verlag GmbH & Co. KGaA.

Aspradkis M. and Byrne, J. (2011) Small field dosimetry: Challenges and progress, Talking point, Medicalphysicsweb.

Attix, F.H., Roesch, W.C. and Tochilin, E. (1968) Radiation Dosimetry, Academic Press, New York.

Attix, F.H. (1986) Introduction to Radiological Physics and Radiation Dosimetry, Wiley, New York.

APS News (2001) American Physical Society, This Month in Physics History: November 8, 1895: Röentgen's Discovery of X-Rays, Volume 10, No. 10, New York.

ASN, (2007) Autorité de sûreté nucléaire, Report concerning the radiotherapy incident at the university hospital centre (CHU) in Toulouse – Rangueil Hospital, Bordeaux, France.

Azangwe, G. et al. (2014) Detector to detector corrections: A comprehensive experimental study of detector specific correction factors for beam output measurements for small radiotherapy beams, Med. Phys. 41 072103-1–16.

Barton, M.B., Jacob, S.A. and Gebsky, V. (2003) Utility-adjusted analysis of the cost of palliative radiotherapy for bone metastases Australas Radiol, 47 (3), pp. 274–278.

Benmakhlouf, H. and Andreo, P. (2017) Spectral distribution of particle fluence in small field detectors and its implication on small field dosimetry, Med. Phys. 44 (2), 713-12.

BIPM (2006) Bureau International des Poids et Mesures, Le Syste´me International d'Unite´s (SI), The International System of Units (SI), 8th ed. (Bureau International des Poids et Mesures, Se`vres).

BIPM JCGM (2008) Bureau International des Poids et Mesures Joint Committee for Guides in Metrology, Evaluation of Measurement Data: Guide to the Expression of Uncertainty in Measurement (GUM), JCGM 100:2008, BIPM, Sévres.

BIPM JCGM (2009) Bureau International des Poids et Mesures Joint Committee for Guides in Metrology, Evaluation of measurement data — An introduction to the "Guide to the expression of uncertainty in measurement" and related documents, JCGM 104:2009, BIPM, Sévres.

BIPM JCGM (2018) Bureau International des Poids et Mesures, Rules of procedure for the Consultative Committees (CCs) created by the CIPM, CC working groups and CC workshops, CIPM-D-01, Version 3, BIPM, Sévres.

BIPM (2012) Bureau International des Poids et Mesures Joint Committee for Guides in Metrology, International vocabulary of metrology – Basic and general concepts and associated terms (VIM), 3rd edition, JCGM 200:2012, BIPM, Sévres.

BIPM (2019) Bureau International des Poids et Mesures, Le Syste´me International d'Unite´s (SI), The International System of Units (SI), 9th ed. (Bureau International des Poids et Mesures, Sévres).

BIPM KCDB (2019) Bureau International des Poids et Mesures, Calibration and Measurement Capabilities - CMC database, www.bipm.org. (Accessed September 2019).

Bouchard, H. et al. (2015) Detector dose response in megavoltage small photon beams. I. Theoretical concepts, Medical Physics Vol. 42, No. 10, 6033-6047.

Bouchard, H. et al. (2015) Detector dose response in megavoltage small photon beams. II. Pencil beam perturbation effects, Medical Physics Vol. 42, No. 10, 6048-6061.

BJR-25 (1996) British Institute of Radiology, Central axis Depth Dose Data for Use in Radiotherapy, British Journal of Radiology Supplement no. 25, The British Institute of Radiology, London.

Burns, D.T. et.al. (2014) Use of the BIPM calorimetric and ionometric standards in megavoltage photon beams to determine W_{air} and I_c, Physics in Medicine and Biology 59, 1353–1365. https://doi.org/10.1088/0031-9155/59/6/1353.

Burns D. and Kessler C. (2018) Re-evaluation of the BIPM international dosimetry standards on adoption of the recommendations of ICRU Report 90, Metrologia, 2018, 55(4), R21-R26.

Casar, B. et al. (2019) A novel method for the determination of field output factors and output correction factors for small static fields for six diodes and a microdiamond detector in megavoltage photon beams, Med. Phys. 46 (2), 944-963.

Casar, B. et al. (2020) Output correction factors for small static fields in megavoltage photon beams for seven ionization chambers in two orientations —perpendicular and parallel, Med. Phys. 47 (1), 242-258.

(1996) Chapter 2: The Development of Radiotherapy: Physics, Technology, Methods, Acta Oncologica, 35:sup6, 24-30, DOI: 10.3109/02841869609083982.

Charles, P. H. (2014) A practical and theoretical definition of very small field size for radiotherapy output factor measurements, Med. Phys. 41 (4).

Chen, M. et al. (2009) Efficient gamma index calculation using fast Euclidean distance transform, Physics in medicine and biology. 54. 2037-47.

Chow, J.C., Seguin, M. and Alexander, A. (2005) Dosimetric effect of collimating jaws for small multileaf collimated fields. Medical Physics, Vol. 32, Issue 3, 759–765.

Côté, B. et al. (2019) Aerrow-Mini: A Probe-Format Graphite Calorimeter for Absolute Dosimetry of Small High-Energy Photon Fields, International Symposium on Standards, Applications and Quality Assurance in Medical Radiation Dosimetry Standards, applications and quality assurance in medical radiation dosimetry (IDOS): Book of Extended Synopses, Contribution ID: 280, Vienna.

Cranmer-Sargison, G. et al. (2011) Implementing a newly proposed Monte Carlo based small field dosimetry formalism for a comprehensive set of diode detectors, Med. Phys. 38, 6592.

Cranmer-Sargison, G. et al. (2013) A methodological approach to reporting corrected small field relative outputs, Radiotherapy and Oncology 109, 350–355.

Crop, F. (2009) The influence of small field sizes, penumbra, spot size and measurement depth on perturbation factors for microionization chambers, Phys. Med. Biol. 54: 2951–2969, doi:10.1088/0031-9155/54/9/024.

Dalaryd, M., Knöös, T. and Ceberg, C. (2014) Combining tissue-phantom ratios to provide a beam-quality specifier for flattening filter free photon beams, Medical Physics 41, 111716; doi: 10.1118/1.4898325.

Das, I. J., Ding, G. X. and Ahnesjö, A. (2008) “Small fields: Nonequilibrium radiation dosimetry,” Med. Phys. 35, 206–215.

Das, I.J. and Francescon, P. (2018) Comments on the TRS-483 protocol on small field dosimetry. Med Phys. 45:5666–5668.

Derreumaux, S. et. al. (2008) Lessons from recent accidents in radiation therapy in France, Radiat Prot Dosimetry; 131(1):130-5.

Derreumaux, S., et. al. (2011) “Concerns in France about the dose delivered to the patients in stereotactic radiation therapy”, Standards, Applications and Quality Assurance in Medical Radiation Dosimetry (IDOS) (Proc. Int. Symp. Vienna, 2010), Vol. 1, IAEA, Vienna 273–286.

Devic, S., et.al. (2005) Precise radiochromic film dosimetry using a flat-bed document scanner, Med. Phys. 32, 2245.

Dieterich, S. and Sherouse, G.W. (2011) Experimental comparison of seven commercial dosimetry diodes for measurement of stereotactic radiosurgery cone factors, Medical Physics 38, 4166; doi: 10.1118/1.3592647.

Duane, S. et al. (2012) An absorbed dose calorimeter for IMRT dosimetry, Metrologia 49, S168–S173. https://doi.org/10.1088/0026-1394/49/5/s168.

DuSautoy, A.R. (2000) NPL calorimetry: the evolution so far. In: Williams AJ, Rosser KE, eds. Proc. NPL Workshop on Recent Advances in Calorimetric Absorbed Dose Standards. Teddington, Middlesex, UK: National Physical Laboratory; 2000:22–27.

Ellison, S.L.R. and Williams, A. ed. (2012) EURACHEM/CITAC Guide Quantifying Uncertainty in Analytical Measurement, CITAC Guide number 4, Third Edition, UK.

Eklund, K. and Ahnesjö, A. (2008) Fast modelling of spectra and stopping-power ratios using differentiated fluence pencil kernels, Phys. Med. Biol. 53 4231–4247.

Followill, D.S. et al. (1998) An empirical relationship for determining photon beam quality in TG-21 from a ratio of percent depth doses, Med. Phys. 25 1202–1205.

Followill, D.S. et al. (2012) The Radiological Physics Center's standard dataset for small field size output factors, Journal of applied clinical medical physics, Vol. 13, No. 5.

Fought, A.M. et al. (2016) Re-examining TG-142 recommendations in light of modern techniques for linear accelerator-based radiosurgery, Med. Phys. 43 (10):5437.

Gianfaldoni, S. et al. (2017) An Overview on Radiotherapy: From Its History to Its Current Applications in Dermatology, Open Access Maced J Med Sci. 5(4):521-525.

Hussein, M., Clark, C.H. and Nisbet, A. (2017) Challenges in calculation of the gamma index in radiotherapy – Towards good practice, Physica Medica, Volume 36, 1-11.

Hyun, M.A. et al. (2017) Ion recombination and polarity corrections for small-volume ionization chambers in high-dose-rate, flattening-filter-free pulsed photon beams, Med. Phys. 44 (2), 618-627.

IAEA (2000) International Atomic Energy Agency, Absorbed Dose Determination in External Beam Radiotherapy: An International Code of Practice for Dosimetry Based on Standards of Absorbed Dose to Water, Technical Reports Series No. 398, IAEA, Vienna.

IAEA (2016) International Atomic Energy Agency, Accuracy requirements and uncertainties in radiation therapy, Human health series no. 31, IAEA, Vienna.

IAEA (2017) International Atomic Energy Agency, Dosimetry of Small Static Fields used in External Beam Radiotherapy: An IAEA AAPM international Code of Practice for reference and relative dose determination, Technical Report Series No. 483, IAEA, Vienna.

ICRU (1976) International Commission on Radiation Units and Measurements, Determination of absorbed dose in a patient irradiated by beams of x- or gamma-rays in radiotherapy procedures, ICRU Report 24, Bethesda, 1976.

ICRU (1980) International Commission on Radiation Units and Measurements, Radiation Quantities and Units, ICRU Report 33, Bethesda, MD.

ICRU (1998) International Commission on Radiation Units and Measurements, Fundamental Quantities and Units for Ionising Radiation, ICRU Report 60, Bethesda, MD.

ICRU (2010) International Commission on Radiation Units and Measurements, Prescribing, Recording, and Reporting Intensity-Modulated Photon-Beam Therapy, ICRU Report 83, Bethesda, MD.

ICRU (2011) International Commission on Radiation Units and Measurements, Fundamental quantities and units for ionizing radiation, ICRU Report 85a, Bethesda, MD.

ICRU (2017) International Commission on Radiation Units and Measurements, Prescribing, recording, and reporting of stereotactic treatments with small photon beams, ICRU report 91, Bethesda, MD.

IEC (2004) International Electrotechnical Commission, Medical Electrical Equipment: Glossary of Defined Terms, IEC TR 60788, IEC, Geneva.

IPEM (2010) Institute of Physics and Engineering in Medicine, Small Field MV Photon Dosimetry, IPEM Rep. 103, IPEM, York.

ISO (2006) International Standards Organisation, Statistics vocabulary and symbols, Part 1: General statistical terms and terms used in probability, ISO/IEC 3534-1, Switzerland.

ISO (2017) International Standards Organisation, General requirements for the competence of testing and calibration laboratories, ISO/IEC 17025, Switzerland.

Johns, H.E. and Cunningham, J.R. (1985) The Physics of Radiology, Thomas, Springfield, IL.

Kessler C. et al. (2019) Comparison of the standards for absorbed dose to water of the METAS, Switzerland and the BIPM in accelerator photon beams (BIPM.RI(I)-K6), Metrologia, 56, Tech. Suppl., 06001.

Kragten, J. (1994) Calculating standard deviations and confidence intervals with a universally applicable spreadsheet technique, Analyst, 119, 2161-2166.

Khan, F. (2003) The Physics of Radiation Therapy, 4th edn, Lippincott, Williams and Wilkins, Baltimore, MD.

Khan, F. (1992) The Physics of Radiation Therapy, 2nd edn, Lippincott, Williams and Wilkins, Baltimore, MD, ISBN 0-683-04502-4.

Klein, E.E. et al. (2009), AAPM Task Group 142 report: Quality assurance of medical accelerators, Med. Phys. 36, 4197–4212.

Knoll, G.F. (1979) Radiation Detection and Measurement, Wiley, New York.

Krauss, A. (2006) The PTB water calorimeter for the absolute determination of absorbed dose to water in ^{60}Co radiation, Metrologia 43:259

Krauss, A. and Kapsch, R.P. (2007) Calorimetric determination of k_Q factors for NE 2561 and NE 2571 ionization chambers in 5 cm x 5 cm and 10 cm x 10 cm radiotherapy beams of 8 MV and 16 MV photons, Phys Med Biol. 52(20):6243-59.

Krauss, A. Kapsch, R.P. and Rouijaa, M. (2011) Calorimetric determination of k_Q factors for NE2561 ionization chambers in 3 cm × 3 cm beams of 6 MV and 10 MV photons, International Symposium on Standards, Applications and Quality Assurance in Medical Radiation Dosimetry Standards, applications and quality assurance in medical radiation dosimetry (IDOS) :proceedings of an international symposium, Vienna 209-217.

Krongkietlearts, K. et al. (2016) Determination of output factor for 6 MV small photon beam: comparison between Monte Carlo simulation technique and microDiamond detector, Journal of Physics: Conference Series 694 012019.

Li, H. et al. (2011) Toward a better understanding of the gamma index: Investigation of parameters with a surface-based distance method. Med Phys.;38(12):6730–6741.

Levin, V. and Tatsuzaki, H. (2002) Radiotherapy services in countries in transition: gross national income per capita as a significant factor Radiother Oncol, 63 (2), pp. 147–150.

L'homel, B., Stadler, M. and Vieillevigne, L. (2017) The PTW T-REF chamber – A new plane parallel transmission chamber as reference detector for small fields, Physica Medica, Volume 44, Supplement 1, Pages 29-30.

Li, S. et al. (2006) Analysis of photon beam data from multiple institutions: An argument for reference data. Medical Physics, Vol. 33, 1991.

LI, X.A. et al. (1995) Lateral electron equilibrium and electron contamination in measurements of head-scatter factors using miniphantoms and brass caps, Med. Phys. 22 1167–1170.

Lillicrap, S.C. et al. (1990) Code of Practice for high-energy photon therapy dosimetry based on the NPL absorbed dose calibration service, Phys. Med. Biol. 35 1355–1360.

Louw, W. and Judge, S. (2018) CCRI President's Report to the 26th meeting of the CGPM, BIPM, Sévres.

Low, D.A. et al. (1998) A technique for the quantitative evaluation of dose distributions, Med Phys. 25(5):656-61.

Mayles, P., Nahum, A. and Rosenwald, J.C. (2007), Handbook of Radiotherapy Physics: Theory and Practice, First edition, Taylor & Francis Group, LLC

Marsolat, F. et al. (2015), Why diamond dimensions and electrode geometry are crucial for small photon beam dosimetry, Journal of Applied Physics 118, 234507; doi: 10.1063/1.4937994.

Massillon-JL, G. et al. (2012) Energy Dependence of the New Gafchromic EBT3 Film: Dose Response Curves for 50 kV, 6 and 15 MV X-Ray Beams*, International Journal of Medical Physics, Clinical Engineering and Radiation Oncology Vol. 1 No. 2 (2012).

McDowell, M. (1997) The national metrology laboratory of South Africa – The first 50 years (1947 – 1997), The Natal witness publishing and printing company (Pty) Ltd, South Africa, ISBN 0-7988-5360-3.

McEwen, M. et al. Addendum to the AAPM's TG-51 protocol for clinical reference dosimetry of high-energy photon beams, Med. Phys. 41 (2014) 041501-1–20.

McEwen, M. R. and DuSautoy, A. R. (2009) Primary standards of absorbed dose for electron beams, Metrologia 46, S59–S79.

Mckerracher, C. and Thwaites, D.I. (1999) Assessment of new small-field detectors against standard-field detectors for practical stereotactic beam data acquisition, Phys. Med. Bio. 44:2143-2160.

McVicker, D., Yin, F. F. and Adamson, J. D. (2016) On the sensitivity of TG-119 and IROC credentialing to TPS commissioning errors. Journal of applied clinical medical physics, 17(1), 34–48. https://doi.org/10.1120/jacmp.v17i1.5452.

Medin, J. et al. (2004) Commissioning of an NRC-type sealed water calorimeter at METAS using ^{60}Co γ-rays, Phys Med Biol. 49:4073–4086.

Meyer, J.L. et al. (2007) New technologies in the radiotherapy clinic, Front Radiat. Ther. Oncol., 40:1-17, doi: 10.1159/000106025.

Muir, B.R. et al. (2017) Electron beam water calorimetry measurements to obtain beam quality conversion factors, Med. Phys. 44 (10), 5433-5444.

Nahum, A.E. (1978) Water/Air Mass Stopping Power Ratios for Megavoltage Photon and Electron Beams, Phys. Med. Biol. Vol 23 No. 1, 24-38.

Nahum, A.E. (2009) “Cavity Theory, Stopping-Power Ratios, Correction Factors”, Chapter 3 in Clinical Dosimetry Measurements in Radiotherapy, Editors DWO Rogers and Joanna E Cygler, AAPM 2009 Summer School Proceedings, Medical Physics Publishing, Madison, WI. (ISBN 978-1-888340-84-6).

Niroomand-Rad, A. et al. (1998) Radiochromic Film Dosimetry: Recommendations of AAPM Radiation Therapy Committee Task Group No. 55, Medical Physics 25, 2093.

Nobecu, L.J. (2017) Cobalt teletherapy small field dosimetry, MSc Research report, University of Witwatersrand.

O’Brien, D. J. et al. (2016) Small field detector correction factors $k_{Q_{clin},Q_{msr}}^{f_{clin},f_{msr}}$ for silicon-diode and diamond detectors with circular 6 MV fields derived using both empirical and numerical methods, Medical Physics 43, 411; doi: 10.1118/1.4938584.

Palmans H. (2012) Determination of the beam quality index of high-energy photon beams under nonstandard reference conditions, Medical Physics 39, 5513-5519.

Palmans, H. et al. (2018) Dosimetry of small static fields used in external photon beam radiotherapy: Summary of TRS-483, the IAEA-AAPM international Code of Practice for reference and relative dose determination. Med Phys. 2018;45:e1123–e1145.

Palmans, H. et al. (2018) Reply to “Comments on the TRS-483 Protocol on Small field Dosimetry”, Med. Phys. 45 (12), 5669-5671.

Papaconstadopoulos et al. (2017) Experimental investigation on the accuracy of plastic scintillators and of the spectrum discrimination method in small photon fields, Med. Phys. 44 (2), 654-11.

Papaconstadopoulos, P. (2016) On the Detector Response and the Reconstruction of the Source Intensity Distribution in Small Photon Fields, PhD Thesis, McGill University.

Park, J.M. et al. (2018) Reliability of the gamma index analysis as a verification method of volumetric modulated arc therapy plans, Radiat Oncol 13, 175.

Picard, S. and Roger, P. (2011a) The BIPM absorbed-dose graphite calorimeter, Poster for the CGPM, BIPM, Sévres.

Picard, S., Burns, D. T. and Roger, P. (2009) Construction of an Absorbed-Dose Graphite Calorimeter, Rapport BIPM-09/01, BIPM, Sévres.

Picard, S., Burns, D. T. and Roger, P. (2011b) The BIPM graphite calorimeter standard for absorbed dose to water, International Symposium on Standards, Applications and Quality Assurance in Medical Radiation Dosimetry Standards, applications and quality assurance in medical radiation dosimetry (IDOS) :proceedings of an international symposium, Vienna 2011, 139-151

Podgorsak, E. B. et al. (2005) Radiation oncology physics: a handbook for teachers and students, Vol. 657, Vienna: International Atomic Energy Agency, ISBN 92–0–107304–6.

PTW 2008/2009 Ionizing radiation detectors brochure.

PTW 2011/2012 Radiation medicine QA solutions brochure.

PTW Radiation therapy detectors for small field brochure.

Ratcliffe, C.P. and Ratcliffe, B. (2015) Doubt-Free Uncertainty in measurement: An introduction for engineers and students, Springer International Publishing, Switzerland.

Renaud, J. et al. (2013) Development of a graphite probe calorimeter for absolute clinical dosimetry, Medical Physics, 40(2), https://doi.org/10.1118/1.4773870.

Renaud, J. et al. (2018) Aerrow:A probe-format graphite calorimeter for absolute dosimetry of high-energy photon beams in the clinical environment, Med. Phys., 45:414-428.

Röentgen, W.C. (1896) On a new kind of rays, Science 3(59):227-31.

Sanchez-Doblado, F. et al. (2003) Ionization chamber dosimetry of small photon fields: A Monte Carlo study on stopping-power ratios for radiosurgery and IMRT beams, Phys. Med. Biol. 48 2081–2099.

Sanchez-Doblado, F. et al. (2007) A new method for output factor determination in MLC shaped narrow beams, Physica Medica, Volume 23, Issue 2, Pages 58-66, ISSN 1120-1797.

Sauer, O. A. and Wilbert, J. (2007) Measurement of output factors for small photon beams, Med. Phys. 34 1983-88.

Sauer, O. A. (2009) Determination of the quality index (Q) for photon beams at arbitrary field sizes, Medical Physics 36(9):4168-72.

Saw, C. B. et al. (2001) Leaf sequencing techniques for MLC-based IMRT, Medical Dosimetry, Vol. 26, No. 2, pp. 199–204.

Seco, J., Clasie, B. and Partridge, M. (2014) Review on the characteristics of radiation detectors for dosimetry and imaging Phys. Med. Biol. 59, R303–R347.

Seuntjens, J.P. and Dusautoy, A.R. (2002) Review of calorimeter-based absorbed dose to water standards, International symposium on standards and codes of practice in medical radiation dosimetry: Book of extended synopses, IAEA-CN--96-3, Vienna, Austria.

Seuntjens, J. and Duane, S. (2009) Photon absorbed dose standards, Metrologia 46, S39–S58.

Seuntjens, J. (2016) Theoretical and practical course on dosimetry of small fields in radiotherapy: Absorbed dose standards for small fields, Regional training course presentations, Johannesburg, South Africa.

Streiner, D.L. and Norman, G.R. (2006) Commentary ‘‘Precision’’ and ‘‘Accuracy’’: Two Terms That Are Neither, Journal of Clinical Epidemiology 59, 327–330.

Svensson, H. and Landberg, T. (1994) Neutron therapy--the historical background, Acta Oncol.;33(3):227-31.

AAPM Task Group 21, Radiation Therapy Committee (1983) American Association of Physicists in medicine, A protocol for the determination of absorbed dose from high-energy photon and electron beams, Med. Phys. 10 741–771.

Thoraeus, R. A. (1932) A study of ionization method for measuring the intensity and absorption of roentgen rays and of the efficiency of different filters used in therapy. Acta Radiol. 15: 1–86.

Thoraeus, R. (1961) Cesium 137 and its Gamma Radiation in Teleradiotherapy,

Acta Radiologica, 55:5, 385-395, DOI: 10.3109/00016926109175133.

Thwaites, D. (2013) Accuracy required and achievable in radiotherapy dosimetry: have modern technology and techniques changed our views?, 7th International Conference on 3D Radiation Dosimetry (IC3DDose), Journal of Physics: Conference Series 444 012006.

Van der Merwe, D. et al. (2017) Accuracy requirements and uncertainties in radiotherapy: a report of the International Atomic Energy Agency, Acta Oncologica, 56:1, 1-6, DOI: 10.1080/0284186X.2016.1246801.

Van Dyk, J. et al. (1999) The modern technology of radiation oncology, A Compendium for Medical Physicists and Radiation Oncologists, Medical Physics Publishing.

Van Dyk, J., Battista, J.J. and Glenn, S.B , Accuracy and Uncertainty Considerations in Modern Radiation Oncology, Chapter 11 of the Modern Technology of Radiation Oncology, Volume 3.

Vassiliev, O.N. et al. (2006) Dosimetric properties of photon beams from a flattening filter free clinical accelerator. Phys Med Biol. 51(7):1907–17.

Wuerfel, J.U. (2013) Dose measurements in small fields, Medical Physics International Journal, vol.1, No.1, 81-90.

Xiao, Y. et al. (2015) Flattening filter-free accelerators: a report from the AAPM Therapy Emerging Technology Assessment Work Group, Journal of Applied Clinical Medical Physics, Vol 16, No 3.

Zeverino, M. et al. (2017) Commissioning of the Leksell GammaKnife ® Icon™, Med. Phys. 44 (2) 355.

Appendix A: Ethics waiver

Human Research Ethics Committee (Medical) 50 years 1966 – 2016

Research Office Secretariat: Faculty of Health Sciences, Phillip Tobias Building, 3rd Floor, Office 301,
29 Princess of Wales Terrace, Parktown, 2193 Tel +27 (0)11-717-1252 /1234/2656/2700
Private Bag 3, Wits 2050, email: zanele.ndlovu@wits.ac.za
Office email: hrec-medical.researchoffice@wits.ac.za
Website: www.wits.ac.za/research/about-our-research/ethics-and-research-integrity/

Ref: W-CJ-170724-1 24/07/2017

TO WHOM IT MAY CONCERN:

Waiver: This certifies that the following research does not require clearance from the Human Research Ethics Committee (Medical).

Investigator: Z L M Msimang (student no. 8802566H).

Project title: Accuracy and associated measurement uncertainties in clinical dosimetry data for static small fields.

Reason: This study will be done using dosimetry equipment in the Department of Medical Physics at CMJAH. There are no human participants and measurements will be done after hours.

UNIVERSITY OF THE WITWATERSRAND
PROF PE CLEATON-JONES
HREC (MEDICAL)
2017 -07- 24
JOHANNESBURG

Professor Peter Cleaton-Jones

Chair: Human Research Ethics Committee (Medical)

Copy – HREC (Medical) Secretariat: Zanele Ndlovu, Rhulani Mkansi, Lebo Moeng.